UNIVERSITÀ
DEGLI STUDI
DI PADOVA

Sede Amministrativa: Università degli Studi di Padova

Dipartimento di Fisica e Astronomia "G.Galilei"

SCUOLA DI DOTTORATO DI RICERCA IN: Astronomia
CICLO XVIII

Determining stellar parameters for giants in the APOGEE-Kepler surveys

Direttore della Scuola: Prof. Giampaolo Piotto
Supervisore: Dott. Léo Alberto Girardi
Co-supervisora: Prof.ssa Paola Marigo

Dottoranda: Thaíse da Silva Rodrigues

UNIVERSITÀ DEGLI STUDI DI PADOVA
DIPARTIMENTO DI FISICA E ASTRONOMIA
"G.GALILEI"

PhD Course in Astronomy – XXVIII cycle

PhD Thesis

# Determining stellar parameters for giants in the APOGEE-Kepler surveys

Thaíse da Silva Rodrigues

Supervisors	**Director PhD School**
PhD Léo Alberto Girardi	
Prof. Paola Marigo	Prof. Giampaolo Piotto

March/April 2017

To my family
Lecir, Rubens, Diego, *and* **Matheus**
Best friends
Aiara, Yanele, Zdenka
My love
Giacomo
And all those who are trying to be **resilient** *as I am*;

Remember: despite how open, peaceful, and loving you attempt to be, people can only meet you, as deeply as they've met themselves.

[Matt Kahn]

I have no special talents. I am only unreasonably persistent.
(it was supposed to be "I am only passionately curious.")

[Adaptation of Albert Einstein sentence to the real academic life]

Siamo tutti universi danneggiati. Da qualcosa o qualcuno siamo stati danneggiati. Dal poco amore o dalle troppe paure, o da chi ci ha promesso certezze scoppiate in volo come pezzi di vetro negli occhi. Le persone più incantevoli al mondo hanno sempre un vissuto complesso. Sono spesso le più difficili da amare ma anche quelle che sanno dare di più. Le persone incantevoli hanno vinto il disincanto e per vincere il disincanto ci vuole tanto coraggio, lo stesso che serve per i sentimenti.

[Massimo Bisotti]

Acknowledgements

These are my pages, maybe my only real pages in this thesis where I can be Thaíse, not Rodrigues, T.S., and I would like to enjoy them as much as I can and I will do it writing in different languages. Motivada pelo "eu não vim até aqui para desistir agora" (Até o fim, Engenheiros do Hawaii), eu tenho que ir até o fim, mesmo que me falte força. Primeiramente devo agradecer a minha família, a todo suporte emocional e financeiro para que eu chegasse até aqui. Agradeço de coração a minha maior inspiração e fonte de forças que é a minha mãe: Lecir. Ela sempre esteve ao meu lado e sempre me deu todo o melhor que pôde. Ela lutou comigo e conquistamos juntas todas as batalhas que enfrentamos. *Momis, te amo muito!* Agradeço também ao meu popis Rubens e aos meus irmãos–amigos Diego e Matheus, que me impulsionaram a correr atrás dos meus sonhos. E se hoje escrevo essas palavras é graças a imensurável ajuda da Aiara, minha florzinha. Ela me encorajou e me motivou em todas as aplicações para doutorado, em todas as minhas dúvidas desde escrever em inglês até as crises existenciais. *Sem você, florzinha, eu não teria conseguido!* Gratidão eterna pela nossa amizade.

Gracias, Juan Pablo, você sempre me apoiou em todas as minhas escolhas. Sempre me recordarei de todo acolhimento que você me ofereceu. Não posso deixar de agradecer quem me ajudou lá no início até eu chegar na Itália, amigos de infância: Natália, Liliana, Roberta e Victor; o meu querido professor de física durante o ensino médio: Eduardo; amigos da UFRJ: Ihani, João Antônio, Loloano, Luana, Lygia e Victor; professores da UFRJ: Gustavo (ex-orientador), Helio Jacques e Denise; amigos da USP: Aiara, Luciene e Daniel; meu orientador de mestrado: Walter; a minha família em São Paulo que me abrigou por quase 3 anos: Elenay, Hélio, Luiz Felipe, Yanele, Daniel, Marcia, João Pedro, Barbara e Fernanda; um *grude* importante: Sergio O.; todos meus tios e tias, primos e primas; a memória dos meus avôs e avós. Vocês foram essenciais para que eu chegasse até aqui!

A música continua "minhas raízes estão no ar, minha casa é qualquer lugar", eu acreditava plenamente nisso, mas depois de mudar de Corumbá, com apenas 17 anos, para o Rio de Janeiro, do Rio de Janeiro para São Paulo, de São Paulo para Padova, comecei a desejar uma casa mais segura, um lugar para aterrar minhas

junto com meus tios MoMa. Nunca esquecerei a coragem da minha momis de cruzar o oceano em um imenso avião e da emoção que sentiu ao conhecer a tão sonhada Veneza.

I would like to thank immensely my best friend Zdenka writing in Czech but unfortunately I cannot. You are really a pearl and I also thank Camila who introduce us, you have been a sister to me here. You hugged me in the moment that I most needed. *I love and miss you a lot.* Rigranzio i miei pochi amici italiani: Matteo – primo amico che ho fatto qua; Leo e Luca – per le partite di calcio condivise sul un tavolo con un big panino e una buona birra; Boldrin – per essere veramente "la definizione di amicizia" che mi piace di piú e per la speranza che io potessi rivivere un sogno perso, grazie per la pianola; Nardin e Borin – grazie mille, Bro e Gatinho! Voi siete stati molto importanti per me durante tutti questi anni! Voi due mi avete accettata come sono e questa è stata una delle esperienze più belle che ho avuto qui. Ringrazio anche i colleghi di dottorato e di stanza per la pazienza di spiegarmi tante cose, per aiutarmi ed anche per capire la mia antisocialità. Mi dispiace, sono fatta cosí!

Ringrazio Alessandra Zorzi, Anna Bologna, Prof. Giampaolo Piotto, Cristina Ronzani e Massimo Turatto per tutto l'aiuto con la burocrazia (che piace a tutti gli italiani!). E principalmente al Dipartimento di Fisica e Astronomia e l'Osservatorio Astronomico di Padova per avermi accettata come dottoranda.

Ringrazio in particolare certe persone che me hanno fatto vedere la vita di un modo diverso: Bernardo S. – mi hai fatto conoscere tante cose e mi sono divertita con la tua personalità diversa da tutti! Francesco L. – tu sei stato molto più importante per me di quello che ti ho lasciato sapere, ed ancora sei. Alessandro S. – il mio vicino che mi ha aiutato a capire tantissime cose, anche come sistemare un lavandino! Stefano P. – tu mi hai messo nel maggior problema che potevo avere qua, ma questo solo ha provato quanto sono forte! Grazie per aiutarmi a superarlo! Luca B. – tu mi hai fatto sentire per la prima volta, dopo tanto tempo, la voglia di vivere, non dimenticherò mai quel momento. Il tuo modo impulsivo-emotivo diverso da me, mi ha fatto vivere delle emozione che mi mancavano. Carlo M. – tu mi hai fatto vivere quello che volevo vivere e mi hai fatto conoscere un mondo molto diverso di quello che conoscevo. Grazie per l'opportunità! Nico F. – tu sei un amico carino e pazzo e desidero il meglio per te, anche se sei testardo! Fred A. – I would like to write German, but you know, I am lazy, maybe you do not know that you gave me hope, hope to keep going, to keep trying, to keep being myself and being free. I will never forget this! *You are really a part of who I am.*

Vorrei anche ringraziare i migliore collaboratori che potevo avere: Andrea Miglio, Diego Bossini, Hugo Coelho e Josefina Montalbàn. Voi mi avete insegnato tanto!

Viver longe de casa por tanto tempo te faz perceber quem são as pessoas que realmente importam. Não posso deixar de enfatizar o quanto o *Le catrage* me ajudou durante todos esses 4 anos. Minha sorrelina, Babi e Fer, vocês foram essenciais para

eu estar aqui. Vocês sempre estiveram comigo, independente do fuso ou da distância. Sorellina, você fez tanto por mim, que não tem palavras nem maquiagem que eu possa comprar para você para te agradecer! *Amo vocês e sei que não conseguiria terminar isso sem vocês!* Minha eterna gratidão a vocês!

La migliore cosa che ho fatto in questo paese è addotare la mia gattina Mela, la mia Melina Verde (grazie all'aiuto di Camila e Dalma). Lei mi ha fatto vivere delle emozione mai vissute, mi ha datto tutto quello di cui avevo bisogno quando ero a casa da sola. Lei mi ha fatto una persona migliore e nostra conessione è una della più forte che ho mai provato. Grazie per prendere cura di me in questi 3 anni insieme! Farò di tutto per te, perchè sei l'unica che sta li sempre con me. Il tuo amore lo sento tutti i giorni e questo mi fa voler essere la migliore mamma per te, cioè viziarti di più.

Ringrazio Giacomo Spagnolo, il mio amore, migliore amico, chef e compagno di casa. Questo ultimo anno è stato il migliore della mia vita, perché tu (e anche Melina) sei stato con me a Magalenha, la nostra casa. Mi hai fatto amarti con tutto quello che potevo e mi hai fatto diventare una persona migliore. Tu sei la parte di me che mi fa ancora vivere la vita con intensità ogni giorno. Grazie per avermi aiutato, amato, sopportato, ed anche per provare a capirmi sempre. Ti amo e vorrei amarti di più. Ringrazio anche perché mi hai portato una famiglia bella! Ringrazio la tua mamma Albertina, il tuo papà Floriano, le tue sorelle Sofia e Elena e tuo fratelo Aristide, e anche Marco, Rosa, e la piccola Zahira che mi ha fatto sentire una zia. La famiglia è il nostro bene più prezioso, come diceva la mia nonna e tu me l'hai datto durante questi ultimi mesi.

Non posso fare finta di niente e non rigranziare la Sertralina e il Rivotril che mi hanno dato forza per proseguire questo percoso, e anche ai professionisti che mi seguono: Michele R., Elena P. e Daniele T.. E più di tutto, devo riconoscere il mio coraggio di chiedere aiuto.

Sono stata lontana dal mio paese per 4 anni e ho imparato ad amare questa città come se fosse la mia città natale. Mi sono persa tante volte nelle piccole vie del centro, con i nomi dei formaggi, con i gelati e i vini. Ho imparato i differenti modi di fare il caffè, a fare la pasta al dente e a dire "ciao" anche se la persona è appena arrivata! Ho perso un quinto del mio tempo con tutti gli obblighi burocratici necessari per vivere qua, ma non mi pento, perchè ho bevuto tutti i vini che potevo per dimenticare la noia. E continuo a bere...

Summary

In the first part of this work, we present distance and extinction determinations for individual stars in the first and second release of the APOKASC catalogue, built from the joint efforts of the Apache Point Observatory Galactic Evolution Experiment (APOGEE) and the *Kepler* Asteroseismic Science Consortium (KASC). Our method takes into account the spectroscopic constraints derived from the APOGEE Stellar Parameters and Chemical Abundances Pipeline, together with global asteroseismic parameters from KASC. Asteroseismic parameters allow us to measure the basic stellar properties of field giants observed far across the Galaxy. Most of such determinations are, up to now, based on simple scaling relations involving the large frequency separation, $\Delta\nu$, and the frequency of maximum power, ν_{max}. The spectroscopic and asteroseismic parameters are then employed to estimate intrinsic stellar properties, including absolute magnitudes, using the Bayesian tool PARAM. We then find the distance and extinction that best fit the observed photometry. We also implemented our code to estimate distances and extinctions taking into account only spectroscopic parameters for the APOGEE stars. We checked our distances by either comparing with other available distance catalogues and with stars belonging to star clusters. Our extinctions were also compared with extinction maps in the literature. The average distance and extinction uncertainties are ~ 2 per cent and ~ 0.08 mag for the stars in the APOKASC catalogue, and ~ 7 per cent and ~ 0.21 mag for the stars without asteroseismic parameters (APOGEE catalogue). In the last part of this work, we implement $\Delta\nu$ and the period spacing, ΔP, computed along detailed grids of stellar evolutionary tracks, into stellar isochrones and hence in our Bayesian method of parameter estimation. Tests with synthetic data reveal that masses and ages can be determined with typical precision of 5 and 19 per cent, respectively, provided precise seismic parameters are available. Adding independent information on the stellar luminosity, these values can decrease down to 3 and 10 per cent respectively. The application of these methods to NGC 6819 giants produces a mean age in agreement with those derived from isochrone fitting, and no evidence of systematics differences between RGB and RC stars. The age dispersion of NGC 6819 stars, however, is larger than expected, with at least part of the spread ascribable to stars that underwent mass-transfer events.

Sommario

Nella prima parte di questa tesi, presentiamo le determinazioni delle distanze ed estinzioni per le stelle singole contenute nella prima e nella seconda release del catalogo APOKASC, costruito dagli sforzi congiunti dell'Apache Point Observatory Galactic Evolution Experiment (APOGEE) e dal *Kepler* Asteroseismology Science Consortium (KASC). Il nostro metodo prende in considerazione i vincoli spettroscopici derivati dell'APOGEE Stellar Parameters and Chemical Abundances Pipeline, insieme ai parametri globali dell'astrosismologia via KASC. I parametri astrosismici ci permettono di misurare le proprietà stellari fondamentali delle stelle giganti di campo osservate a grandi distanze attraverso la Galassia. La maggior parte di tali determinazioni sono, ad oggi, basate su semplici relazioni di scala che coinvolgono la grande separazione in frequenza, $\Delta\nu$, e la frequenza corrispondente al massimo della potenza spettrale delle oscillazioni, $\nu_{\max}$. I parametri spettroscopici ed astrosismologici vengono poi impiegati per stimare le proprietà intrinseche stellari, tra cui magnitudine assoluta, usando il codice Bayesiano PARAM. Dopo sono calcolate la distanza e l'estinzione che meglio si adattano alla fotometria osservata. Abbiamo anche implementato il nostro codice per stimare le distanze e le estinzioni prendendo in considerazione solamente i parametri spettroscopici per le stelle del catalogo APOGEE. Abbiamo controllato le nostre distanze confrontandole con gli altri cataloghi di distanza disponibili e con stelle appartenenti ad ammassi stellari. Le nostre estinzioni sono state confrontate anche con le mappe di estinzione presenti nella letteratura. Le incertezze medie delle distanze e delle estinzioni sono ~ 2 per cento e ~ 0.08 mag per le stelle nel catalogo APOKASC, e ~ 7 per cento e ~ 0.21 mag per le stelle senza parametri asterosimici (catalogo APOGEE). Nell'ultima parte di questa tesi implementiamo $\Delta\nu$ e la separazione in periodo, ΔP, che sono state calcolate lungo griglie dettagliate di tracce evolutive stellari, poi in isocrone stellari ed infine in nostro metodo Bayesiano di stima di parametri. Prove con dati sintetici rivelano che le masse e le età possono essere determinate con precisione tipica di 5 e di 19 per cento, rispettivamente, a condizione che precisi parametri sismici siano disponibili. Aggiugendo informazioni indipendenti sulla luminosità stellare, questi valori possono diminuire fino a 3 e 10 per cento, rispettivamente. L'applicazione di questi metodi alle stelle giganti di NGC 6819 produce una età media in accordo con

i valori derivati da isocrone fitting, e non produce nessuna evidenza di differenze sistematiche tra le stelle RGB e RC. La dispersione di età delle stelle di NGC 6819, tuttavia, è maggiore del previsto, con almeno parte della dispersione attribuibile alle stelle sottoposte ad eventi di trasferimento di massa.

Contents

XIII

List of Tables

List of Figures

XVII

Chapter 1

The Milky Way

1.1 A brief description of our Galaxy

In 1888 the famous Brazilian poet Olavo Bilac (1865–1918) wrote a book entitled *Via-Láctea*, in english Milky Way (MW), whose main sonnet is as following

Sonnet XIII

"Well (thou´ll say) hearing stars! Certainly
Thou´ve lost your mind!" And I´ll say to thee, however
That, to hear them, many times I wake
And open the windows, palid in awe...

And we talk all night long, while
The milky way, as an open canopy,
Shines. And, at the coming of the sun, missing and crying,
I still look for them in the desert sky.

Thou´ll now say: "Crazed friend!
What do thou talk to them? What sense
Has what they say, when they are with thee?"

And I´ll say to thou: "Love to understand them!
Because only he who loves may have ears
Capable of hearing and understanding stars."

Even if Galileo Galilei (1564–1642), two centuries before, has seen for the very first time through a telescope that the literally *milky way* in the night sky was formed by several dim stars, at the time of Olavo Bilac death, the concept of galaxy (or even Universe) was not yet settled. Until that moment, some ideas were written about what surrounded us, but the first scientific research in order to understand the shape and the size of the Universe was carried out by William Herschel (1738–1822), who

did a systematic study of the distribution of stars across the sky. However his view of the Universe was incorrect given the assumption that all stars have almost the same intrinsic brightness and were uniformly distributed. Then Jacobus Kapteyn (1851–1922), with more stellar data available, also estimated the spatial distribution of the stars increasing the size and scale height of our Galaxy, but he did a very erroneous assumption that the interstellar medium was completely transparent (Kapteyn, 1922). In 1914 Harlow Shapley (1885–1972) started to study globular clusters and noticed that they do not spread uniformly as in the current model of the MW, but they concentrated in one direction (Sagittarius constellation), indicating that the Sun lies far from the Galactic center (~ 15 kpc), contradicting the Kapteyn Universe. Without going into too many details, the scenario of Shapley was supported by the study of proper motion and radial velocity of several individual stars by Bertil Lindblad (1895–1965), who draw the first picture of the the spiral kinematics of the Galaxy and its spiral arms; and by Jan Oort (1927) who estimated the rotational velocity of the Sun and realized that Shapley overestimated its position. The first reasonable image of our entire Galaxy was just possible thanks to the collaboration of many radio telescopes in the world during the 50's, which observed the 21 cm emission line of atomic hydrogen suggested by Hendrick van den Hulst that traced the velocity distribution of interstellar neutral clouds (Oort, Kerr & Westerhout, 1958).

Unfortunately the poet Bilac died, perhaps believing that he was lunatic, without knowing that in fact the stars have sound waves propagating inside them, and thanks to the current technology we are able to *hear* them and study what is going on in their interior. Still in 1926, Sir Arthur Stanley Eddington in his famous book *The Internal Constitution of the Stars* (Eddington, 1926) wrote:

> At first sight it would seem that the deep interior of the sun and stars is less accessible to scientific investigation than any other region of the universe. Our telescopes may probe farther and farther into the depths of space; but how can we ever obtain certain knowledge of that which is hidden behind substantial barriers? What appliance can pierce through the outer layers of a star and test the conditions within?

Eddington was wondering, or perhaps lamenting, about how can we explore the unseen. However Kurtz (2005) wrote the answer in an formidable way:

> Therefore he (Eddington) would have been amazed and delighted to know that there is now a way to see inside the stars – not just calculate their interiors – but literally see. We have invented Eddington's "appliance" to pierce the outer layers of a star: It is asteroseismology, the probing of stellar interiors through the study of their surface pulsations.

2

Also the poet Olavo Bilac would be delighted to know that he was *right*, we really need to *love the stars to be able to hear them*, in the sense that we should persist in our hypothesis/theories/assumptions but also *open the windows* in order to *talk to the stars* and obtain observational results that can test/confirm/change the paths of our speculation, because the theory of stellar pulsation started to be explored by (Eddington, 1918; Ledoux, 1945), the theoretical asymptotic expression for non radial oscillation of stars, which gives physical significance to some seismic parameters, came much later (Tassoul, 1980; Gough, 1986, 2003), while the first detection of solar-like oscillations in a red giant star was seen only in 2002 (Frandsen et al., 2002). Nowadays we see (*hear*) the star sounds by the periodic changes in theirs brightness thanks to the improvement of the telescopes and instruments.

Observations of interstellar neutral hydrogen clouds by radio suggest that our Galaxy has similar spiral structure compared with several external galaxies, which present in general two spiral arms starting from either the central bulge or from a bar that cross the bulge. Our position inside the MW complicates the study of its morphology, but assuming that there are similarities between our Galaxy and external spiral galaxies, simple models of stellar counts were built (Bahcall & Soneira, 1984) and were able to make already very good predictions about the observed distributions of stellar counts, magnitudes, and colors. From photometric and parallax data, the disk of our Galaxy was distinguished in thin and thick disks (Gilmore & Reid, 1983).

In the 90's, radio data indicated that our Galaxy is type Sb-Sbc following Hubble's classification: a bulge with intermediate size and moderate winding of the arms (Binney & Merrifield, 1998). While observations in infrared of the center of the Galaxy show clear evidences of the presence of a bar (Blitz & Spergel, 1991; Bland-Hawthorn & Gerhard, 2016).

The better knowledge of stellar evolution theory, some key wide-area photometric surveys (e.g. 2MASS and SDSS), and the release of Hipparcos parallaxes have further revolutionised the field, improving distance calibrations and providing better models for the spatial distribution of the stars in the MW (such as Robin et al., 2003; Girardi et al., 2005; Jurić et al., 2008).

To date it is well known that our Galaxy comprises a thin disk with radius between $25 - 30$ kpc and a scale height of 300 pc, while the thick disk has a scale height of 900 pc (Jurić et al., 2008); a bulge with radius of $2 - 3$ kpc, and a diffuse halo comprising many globular clusters that extends more than 30 kpc from the center Binney & Merrifield (1998). The Sun locates in the Galactic disk, between the inner Sagittarius arm and the outer Perseus arm (Mihalas & Binney, 1981), approximately 25 pc above the midplane (Jurić et al., 2008) and 8.5 kpc away from the center (IAU standard).

In order to understand the history and evolution of our Galaxy we still need to obtain more information about 3 essential parameters of stars: distances, ages, and

chemical abundances, for a large quantity of stars and with more precision in the data. These properties are necessary to test quantitatively the chemo-dynamical models of our Galaxy. Large catalogues of homogeneously-derived stellar atmospheric properties and chemical abundances started to become available with the advent of multi-fiber spectroscopy surveys, such as the Sloan Digital Sky Survey (Strauss et al., 1999) and the Radial Velocity Experiment (Steinmetz et al., 2006).

Stellar distance and age estimates, instead, were available only for stars in clusters, and for a few hundreds of nearby stars in the Hipparcos catalogue (Jørgensen & Lindegren, 2005). As we will see later in this thesis, stellar properties, specially ages of distant field stars, are now becoming accessible via asteroseismology. They are robust if accompanied with high-resolution spectroscopy and stellar models.

1.2 Present large surveys of the Milky Way

A number of massive high-resolution spectroscopy surveys (e.g., APOGEE, Gaia-ESO, ARGOS, GALAH Gilmore et al., 2012; Freeman et al., 2013; Freeman, 2012; Majewski et al., 2014) are presently being conducted as part of a major community effort to reveal the evolution and present structure of our Milky Way (MW) galaxy. These surveys promise to greatly expand the available data base of spectroscopic properties such as radial velocities, effective temperatures, surface gravities and chemical abundances. As demonstrated by several authors (Allende Prieto et al., 2006; Burnett & Binney, 2010; Binney et al., 2014; Hayden et al., 2014; Santiago et al., 2016), spectroscopic parameters coupled with photometry can provide distance estimates for all of the observed stars, especially when the surface gravity, $\log g$, is well-constrained. This is preferentially done via Bayesian methods that naturally take into account the many sources of measurement uncertainties and biases. However, it is also clear that a major effort is needed to calibrate such distance determinations and reduce their uncertainties below the $\sim$20 per cent level.

Future astrometry from Gaia will obviously provide distance calibrators over a wide range of apparent magnitudes and distances – except for the very red and optically-obscured stars, hidden by dust lanes across the Galactic mid-plane. In the meantime, distance determinations for field giants in spectroscopic surveys must rely essentially on just two kinds of calibrators: stars in clusters, and stars with well-determined asteroseismic parameters. In this paper we concentrate on the latter, discussing the accuracies in distance determinations that are attainable via Bayesian methods.

There is a very special sample of stars – the APOKASC sample. This unique data set results from a collaboration between *Kepler* Asteroseismic Science Consortium

(KASC[1], Kjeldsen et al., 2010) and Apache Point Observatory Galactic Evolution Experiment (APOGEE Majewski et al., 2014), which itself is part of the third phase of the Sloan Digital Sky Survey (SDSS-III; Eisenstein et al., 2011). Almost 2,000 red giants targeted by the *Kepler* satellite mission (Borucki et al., 2010) have been observed by APOGEE during the first year and included in the SDSS-III Data Release 10 (DR10, Ahn et al., 2014). They correspond to the sample presented in Pinsonneault et al. (2014) and discussed in the fisrt part of this work. The entire APOKASC-2 sample includes over 10,000 giants and is part of the SDSS-IV/APOGEE-2 campaign.

Solar-like oscillations are excited in cool stars, and the natural periods for low density red giants (of the order of days to weeks) are sufficiently long for them to be easily detected for instance with the *Kepler* cadence (Hekker et al., 2010). *Kepler* or CoRoT (Baglin & Fridlund, 2006) asteroseismic data can be used to infer mean density, $\log g$, masses ($\mathcal{M}$), radii (R) – when combined with an effective temperature estimate – and diagnostics of evolutionary state. The APOGEE spectra provide accurate determinations of effective temperatures (T_{eff}) and chemical abundances of several elements (García Pérez et al., 2016). There is also an extensive data base of photometry for these stars, which can provide additional constraints on stellar properties.

This data set provides a powerful set of tools for estimating stellar distances. Precise asteroseismic surface gravities, combined with mass constraints, can be used to infer stellar radii. T_{eff} and extinction can be measured using spectroscopy and photometry. This information is straightforwardly converted into intrinsic luminosities from the standard relation

$$L = 4\pi R^2 \sigma T_{\text{eff}}^{\,4}, \tag{1.1}$$

where σ is the Stefan-Boltzmann constant. When L is combined with a bolometric correction, an extinction, and the observed apparent magnitude in a given pass-band, a so-called 'direct measurement' of the distance is possible (see e.g., Miglio et al., 2013). Bayesian methods combine the likelihood of all possible solutions to provide a better weighted – and possibly more accurate – solution that includes prior information about the data set. Essentially, Bayesian methods incorporate information from stellar models that allows us (1) to require a consistent stellar parameter measurement, as opposed to permitting unphysical combinations of mass, radius, temperature, and metallicity; (2) to account for population effects, such as lifetime, the star formation rate, and the initial mass function, which bias the true stellar parameters in a manner inconsistent with a purely Gaussian distribution; and

---

[1] http://astro.phys.au.dk/KASC

5

(3) to reconcile independent methods for inferring properties such as the effective temperature.

Once distances to the asteroseismic targets are determined, they can be used for a series of applications related to Galactic archaeology (Miglio et al., 2013). Especially useful are the red giants, which can be measured at large distances due to their intrinsic brightness, hence probing regions of the MW far from the well-studied Solar Neighbourhood. In addition, the asteroseismic distances will help to obtain a better distance calibration for stars observed in broad-band photometry and high-resolution spectroscopy alone.

1.2.1 APOGEE

APOGEE uses a high-resolution infrared spectrograph (Wilson et al., 2012), mounted at the Apache Point Observatory 2.5 m telescope (Gunn et al., 2006), with a mean resolution of $\sim$22,500 in the H-band (spectral coverage: $1.51 - 1.70\ \mu$m). APOGEE has already observed more than 150,000 stars selected from 2MASS photometry, at typical signal-to-noise ratios of ~ 100 per resolution element. The targeted stars are mostly red giant branch (RGB), red clump (RC), and asymptotic giant branch stars (Zasowski et al., 2013), and are spread over all regions of the MW, including the bulge, disk, and halo. The scientific exploitation of this enormous data base is facilitated by the APOGEE Stellar Parameter and Chemical Abundances Pipeline (ASPCAP; Mészáros et al., 2013; García Pérez et al., 2016). For each APOGEE target, ASPCAP returns basic stellar parameters (effective temperature, surface gravity, metallicity), and individual chemical abundances for a number of elements. The raw ASPCAP stellar parameters were then compared with independent external measurements from star cluster members and asteroseismic targets for the key stellar parameters, namely overall metallicity ([M/H]), surface gravity, and effective temperature. The final DR10 results included a recommended set of corrections intended to make the ASPCAP results consistent with the values from these external checks (see Mészáros et al., 2013). In the first part of this work, we use the T_{eff} and [M/H] 'corrected ASPCAP values' provided in DR10, instead of the raw ones; they include corrections that improve the agreement with other independent scales based on the infrared-flux method (IRFM) and on cluster data. The [M/H] are calibrated with the literature values of [Fe/H] in 20 star clusters.

In the second part of this work, we use the DR12 results (Alam et al., 2015), which includes all the data observed till 2014 July. Approximately 46000 new stars were included in the catalogue and many improvements were done in the ASPCAP pipeline in order to derive more accurate fundamental stellar parameters and also individual chemical abundances up to 15 elements.

1.2.2 *Kepler*

The *Kepler* space telescope has observed ∼196,400 stars (Huber et al., 2014) in a field of 105 deg^2 towards the constellations of Cygnus and Lyra (Borucki et al., 2010). Apart from the discovery of exoplanets and multiple stellar systems, the high temporal and photometric quality of the data provides the possibility to study red giants by detection of solar-like oscillations (e.g., Huber et al., 2010; Chaplin et al., 2011). For solar-like oscillators with pulsations excited in the turbulent outer layers, two global asteroseismic parameters can be extracted: the average large frequency separation, $\Delta\nu$, and the frequency of maximum oscillation power, $\nu_{\max}$. The former is the dominant frequency separation of the near-regular pattern of high overtones, and depends to good approximation on the mean density $\overline{\rho}$ of the star (Vandakurov, 1968):

$$\Delta\nu \propto \overline{\rho}^{1/2} \propto \mathcal{M}^{1/2} R^{-3/2}. \tag{1.2}$$

The latter is the frequency of maximum power of the Gaussian-like modulation of the mode amplitudes, which is related to the acoustic cut-off frequency of the star, and therefore to its fundamental parameters (Brown et al., 1991; Belkacem et al., 2011):

$$\nu_{\max} \propto g T_{\text{eff}}^{-1/2} \propto (\mathcal{M}/R^2) T_{\text{eff}}^{-1/2}. \tag{1.3}$$

Adopting homology relations and considering reference values of $\Delta\nu$ and $\nu_{\max}$ derived from the Sun, these equations determine the mass and radius of a star independently of evolutionary stellar models, if a value for the effective temperature is available. This is the so-called 'direct method' of parameter determination. Asteroseismic radii agree to within 5 per cent of those inferred from interferometry (Huber et al., 2012) and from stars with *Hipparcos* parallaxes (Silva Aguirre et al., 2012). Masses are more difficult to directly constrain, but eclipsing binaries in NGC 6791 with well-measured masses (Brogaard et al., 2012) can be used to infer the expected masses for red giants. Asteroseismic mass estimates for cluster members (Miglio et al., 2012) are close to, but greater than, these mass estimates; for these stars, systematic uncertainties in the asteroseismic masses are at the 10 per cent level. A larger systematic trend for metal-poor stars is found (Epstein et al., 2014), but such stars are rare in our sample. For our purposes, the primary impact of mass uncertainties is their impact on radius measurements, as overestimated masses at fixed surface gravity will require overestimated radii to compensate.

1.2.3 APOKASC

This excellent and accurate alternative to derive stellar properties encouraged the APOGEE team to include *Kepler* stars on their target list, giving rise to the APOGEE-KASC collaboration (APOKASC). Approximately ∼10,000 stars in the magnitude

range $7 \leq H \leq 11$, including giants from the open clusters NGC 6791 and NGC 6819, were already observed; out of 2,000 stars are part of the first APOKASC public release (Pinsonneault et al., 2014) and are distributed in the sky as in Fig. 1.1. The squares show the *Kepler* field of view, and the circles indicate the APOGEE plates observed during the first year with the stars in the sample (red dots). The target selection and first release of the APOKASC catalogue are described in Pinsonneault et al. (2014). A total of 1989 stars having both seismic and spectroscopic data are analysed in this work.
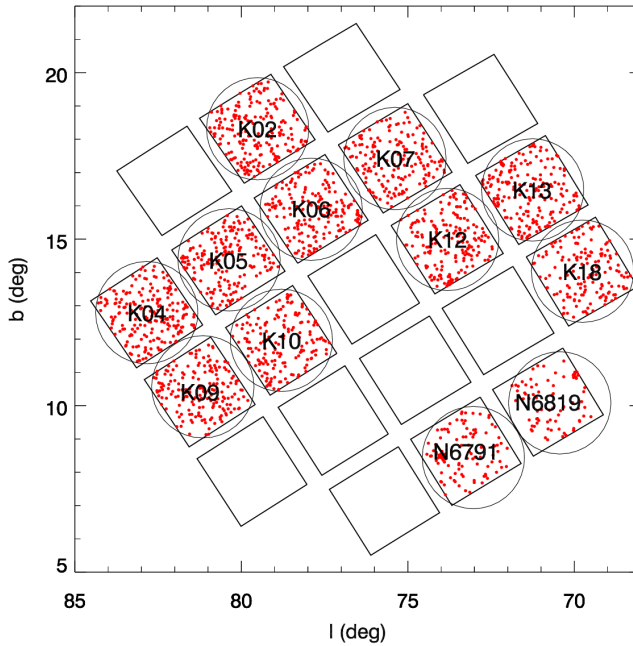
Figure 1.1: Position of APOKASC fields (circles) in Galactic coordinates relative to the *Kepler* field (squares). Red dots represent the stars observed during the first year and analysed in this paper. The final APOKASC sample will include a significantly larger sample across the entire *Kepler* field.

In addition to the spectroscopic and asteroseismic parameters, stars in the APOKASC catalogue have measured apparent magnitudes in

- SDSS $griz$ and $DDO51$, as measured by the KIC team (Brown et al., 2011), and corrected by Pinsonneault et al. (2012);

- JHK_{s} from 2MASS (Cutri et al., 2003; Skrutskie et al., 2006);

- the *Kepler* magnitude, Kp, as derived from a combination of the $griz$ magnitudes (Brown et al., 2011);

- WISE photometry (at 3.35, 4.6, 11.6 and 22.1μm, or W1 to W4) from the Preliminary Release Source Catalog (Wright et al., 2010).

For this work, we discard the Kp magnitude because it does not represent an independent photometric measurement, and DDO51 because it is a relatively narrow (and non-standard) passband, which causes problems in our synthetic photometry (see Girardi et al., 2002). The WISE photometry in the filters $W3$ and $W4$ are disregarded because of their larger measurement uncertainties and possible contamination by warm interstellar dust (Davenport et al., 2014, and references therein). Thus, we make use of a set of nine photometric measurements covering the entire wavelength range from the blue to the mid-infrared, using standard filter transmission curves and well-defined zero-points, which are all easily reproducible by stellar models, as illustrated below.

Chapter 2

Bayesian method applied to the APOKASC and APOGEE surveys

2.1   Introduction

In principle, one could simply derive independent observational estimates for the stellar observables, using the direct method. However, there are important effects which are neglected by treating all stellar parameters as uncorrelated and all errors as strictly Gaussian. For example, stars are much more likely to be observed in long-lived evolutionary phases than in short-lived ones; less massive stars are more common than higher mass ones; and stellar theory makes strong predictions about the allowed combinations of mass, radius, T_{eff}, and abundance. Bayesian methods provide a natural way of taking these effects into account.

In this work, we adopt a Bayesian method implemented as an extension to the PARAM code[1] (da Silva et al., 2006), which estimates stellar properties by comparing observational data with the values derived from stellar models, in this case a data set of theoretical isochrones. It is similar to the methods developed by Hernandez, Valls-Gabaud & Gilmore (1999) and Jørgensen & Lindegren (2005), in the sense that it (1) provides the likelihood of all stellar parameters, after computing every possible solution, it (2) provides an easy and reliable way to estimate uncertainties, since it considers the observational ones and weights the contribution of each component according to its observational uncertainties, and it (3) applies Bayesian inference, i.e., it takes into account prior information on the data set. PARAM was extended to build a well-sampled grid of stellar models including seismic properties. Similar grid-based methods are described in Stello et al. (2009) and Basu, Chaplin & Elsworth (2010).

---

[1]http://stev.oapd.inaf.it/param

Our method works as follows: first, it determines the intrinsic stellar properties, and in a second step it estimates the distances and extinctions. These two steps are explained in Sec. 2.2.1 and 2.2.2, respectively. Sec. 2.2.3 explains why the method is separated in these two steps. Sec. 2.2.4 explains a more direct way to estimate distances that was also implemented in our code. Sections 2.2.5, 2.2.6, and 2.2.7 describes the impact of knowing the evolutionary stage, applying priors on distances, and the effects of systematic shifts in metalicitty and effective temperature, respectively. Distances and extinctions for the first data release of APOKASC are in Sec. 2.2.8, and comparisons with distances from stars cluster and other catalogues in the literature are in Sec. 2.2.9, 2.2.10, and 2.2.11. We then implement our code in order to estimate distances and extinctions to the entire APOGEE catalogue (Sec. 2.3). Finally we compute the stellar properties, distances, and extinctions for the entire set of APOKASC stars (last data release) in Sec. 2.4.

2.2 Description of the method and application to the first APOKASC catalogue

2.2.1 Step 1: determining intrinsic stellar properties

The adopted set of isochrones is PARSEC v1.1[2] (Bressan et al., 2012), from the Padova-Trieste stellar evolution group, which rely on updated input physics, and includes a solar model that reproduces tight constraints from helioseismology. For this work, isochrones were re-generated with a very small stepsize in both age and metallicity – namely 0.02 dex in $\log \tau$ and 0.01 dex in [M/H]. At every point on the isochrones $\Delta\nu$ and $\nu_{\max}$ are computed from the scaling relations

$$\frac{\Delta\nu}{\Delta\nu_\odot} = \left(\frac{\mathcal{M}}{M_\odot}\right)^{1/2} \left(\frac{R}{R_\odot}\right)^{-3/2},$$
$$\frac{\nu_{\max}}{\nu_{\max\odot}} = \frac{\mathcal{M}}{M_\odot} \left(\frac{R}{R_\odot}\right)^{-2} \left(\frac{T_{\text{eff}}}{T_{\text{eff}\odot}}\right)^{-1/2}, \tag{2.1}$$

where the solar values of $\Delta\nu_\odot = 135.03$ μHz and $\nu_{\max\odot} = 3140.0$ μHz have been used (see Pinsonneault et al., 2014). The top panel of Fig. 2.1 illustrates how the isochrones appear in a $\Delta\nu$ versus $\nu_{\max}$ diagram, in comparison with the more familiar Hertzsprung–Russell (H–R) diagram (inset). In order to clarify, the bottom panel shows the ratio $\nu_{\max}^{0.75}/\Delta\nu \propto M^{0.25}T_{\text{eff}}^{-0.375}$ (cf. Huber et al., 2011), which removes the radius dependence, consequently the luminosity.

---

[2]http://stev.oapd.inaf.it/cmd

In addition, we have stored information about the evolutionary stage along the isochrones, which allows us to separate isochrone sections into two broad groups of 'core-He burners' and 'non-core He burners'. Many stars in the APOKASC catalogue can be safely classified into these two groups via the so-called period spacing of mixed modes, ΔP (Bedding et al., 2011; Beck et al., 2011; Mosser et al., 2011; Stello et al., 2013). Mixed modes result from gravity waves propagating in the radiative interior which couple to pressure waves in the envelope, so that they become observable at the stellar surface, providing direct information about the stellar deep interior.

From the T_{eff}, [M/H], $\Delta\nu$ and ν_{max} measurements, PARAM derives a probability density function (PDF) for the following stellar parameters: $\mathcal{M}$, R, $\log g$, age (τ), mean density, and absolute magnitudes in several passbands, M_λ. First, the code computes the posterior probability, which is the probability of a chosen set of models given the prior probability on the models and the measured data, expressed as

$$p(\mathbf{x}|\mathbf{y}) = \frac{p(\mathbf{y}|\mathbf{x})p(\mathbf{x})}{p(\mathbf{y})}, \tag{2.2}$$

where $p(\mathbf{x})$ represents the prior function, $p(\mathbf{y}|\mathbf{x})$ the likelihood function, and $p(\mathbf{y})$ is a normalization factor (which does not depend on $\mathbf{x}$, and can be ignored); $\mathbf{x}$ and $\mathbf{y}$ are the set of parameters to be derived and of measured data, respectively,

$$\mathbf{x} = (\mathcal{M}, R, \log g, \tau, M_\lambda),$$
$$\mathbf{y} = ([\text{M/H}], T_{\text{eff}}, \Delta\nu, \nu_{\text{max}}).$$

The theoretical isochrones make the connection between $\mathbf{x}$ and $\mathbf{y}$, $\mathbf{y} = \mathcal{I}(\mathbf{x})$. Assuming that the uncertainties of the measured data can be described as a normal distribution with a mean y' and standard deviation $\sigma_{y'}$, the likelihood function can be written as

$$p(\mathbf{y}'|\mathbf{x}) = L(\mathbf{y}', \mathcal{I}(\mathbf{x}))$$
$$= \prod_i \frac{1}{\sqrt{2\pi}\sigma_{y_i}} \times \exp\left(\frac{-(y_i' - y_i)^2}{2\sigma_{y_i}^2}\right). \tag{2.3}$$

The prior function is given by

$$p(\mathbf{x}) = p(\mathcal{M}) \times p(\tau) \times p([\text{M/H}]), \tag{2.4}$$

where we adopted a flat prior for metallicity and age, $p(\tau) = p([\text{M/H}]) = 1$, i.e., that all metallicities and ages are equally probable, inside the interval $[10^6, 10^{10}]$ yr. The prior in mass, $p(\mathcal{M})$, is given by the Chabrier (2001) initial mass function, $p(\mathcal{M}_{\text{i}})$, but corrected for the small amount of mass lost close to the tip of the RGB, by adopting a relation $\mathcal{M} = \mathcal{M}_{\text{i}} - \Delta\mathcal{M}_{\text{i}}$. This correction $\Delta\mathcal{M}_{\text{i}}$ is computed from

13
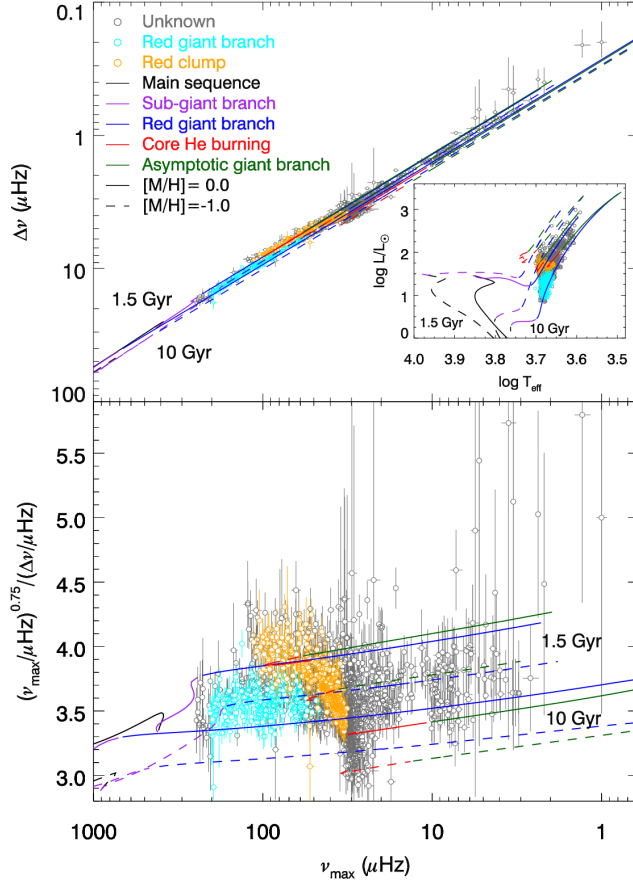
Figure 2.1: Top panel: an illustration of stellar isochrones in the $\Delta\nu$ versus $\nu_{\max}$ plane, covering the same range as the APOKASC giants. The isochrones are shown for two different ages (1.5 and 10 Gyr) and metallicities (0.0 and -1.0). Different evolutionary stages along the isochrones are marked with different colors. The grey, cyan, and orange dots are stars with asteroseismic evolutionary stage classification as unknown, RGB, and RC. The inset shows the same models and data in the more familiar H–R diagram. Bottom panel: same as in the top panel, but plotting the ratio between $\nu_{\max}^{0.75}$ and $\Delta\nu$, which removes the radius dependence.

a Reimers (1975) law with efficiency parameter $\eta = 0.2$ (Miglio et al., 2012), and turns out to be close to null for the bulk of RGB stars, and smaller than 0.1 $M_\odot$ for all RC stars. No additional prior was adopted for the other parameters.

Finally, the marginal distribution $p(x_i|\mathbf{y}')$ (hereafter $p(x_i)$) can be calculated, which is the PDF of each parameter x_i obtained by integrating the posterior PDF given in Eq. 2.2 over all parameters, except x_i.
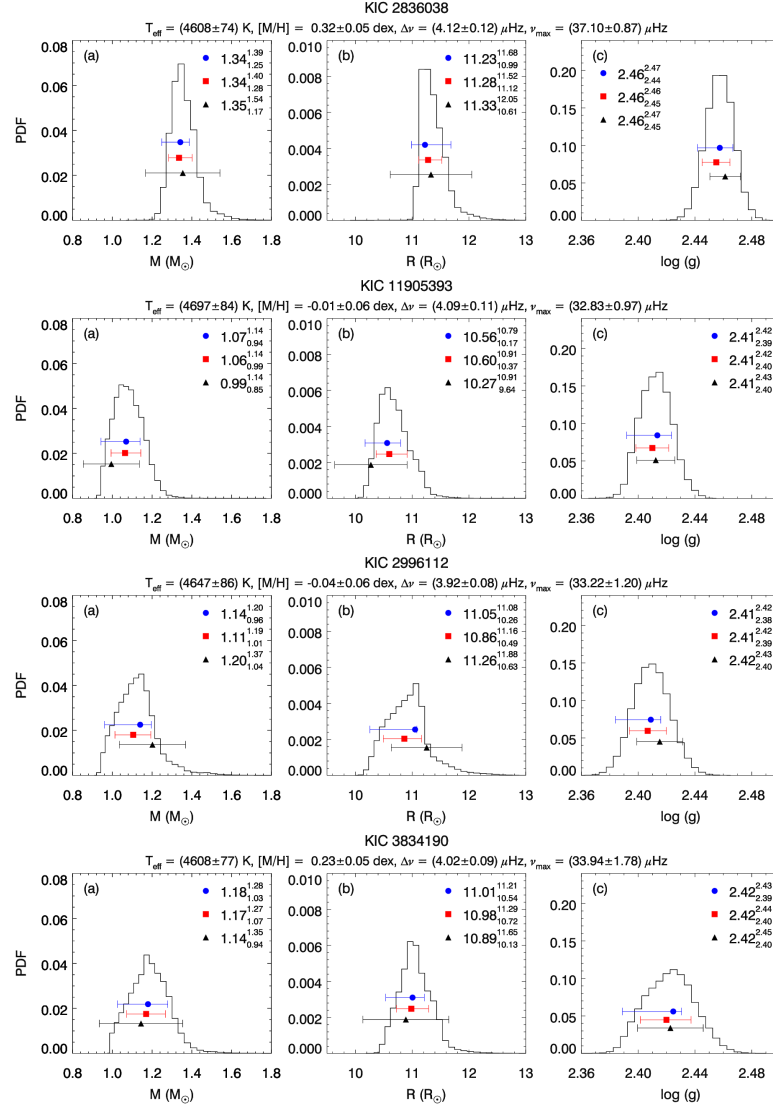
Figure 2.2: (a) PDF of the mass, (b) radius, and (c) logarithm of surface gravity, for a set of typical APOKASC targets presenting single-peaked PDFs, and in a sequence of increasing uncertainties in the derived parameters. The adopted values of T_{eff}, [M/H], $\Delta\nu$ and ν_{max} are indicated in the plots. The median and its 68 per cent CI, and the mode and its 68 per cent CI are represented by red and blue symbols, respectively. The black triangles are the results of the direct method.

As an example, Fig. 2.2 presents the resulting marginal PDFs of $\mathcal{M}$, R, and $\log g$ for a series of four stars with well-behaved, single-peaked results. The adopted values of T_{eff}, [M/H], $\Delta\nu$ and ν_{max} are indicated in the plots. For each PDF we have

15

computed the median and 68 per cent credible intervals (CI; red symbols) by simply determining the points along the cumulative distribution function where suitable values were reached. In addition, we also indicate the mode and the 68 per cent CI (blue symbols), which are more suitable to represent the parameters inferred via the Bayesian method. The 68 per cent CI of the mode is determined by looking at the shortest interval that contains 68 per cent of the PDF area (Box & Tiao, 1973). For simplicity, in what follows, the half-widths of these 68 per cent CI will be referred to as $\sigma(x)$, and used as an estimate of the uncertainties for each parameter x.
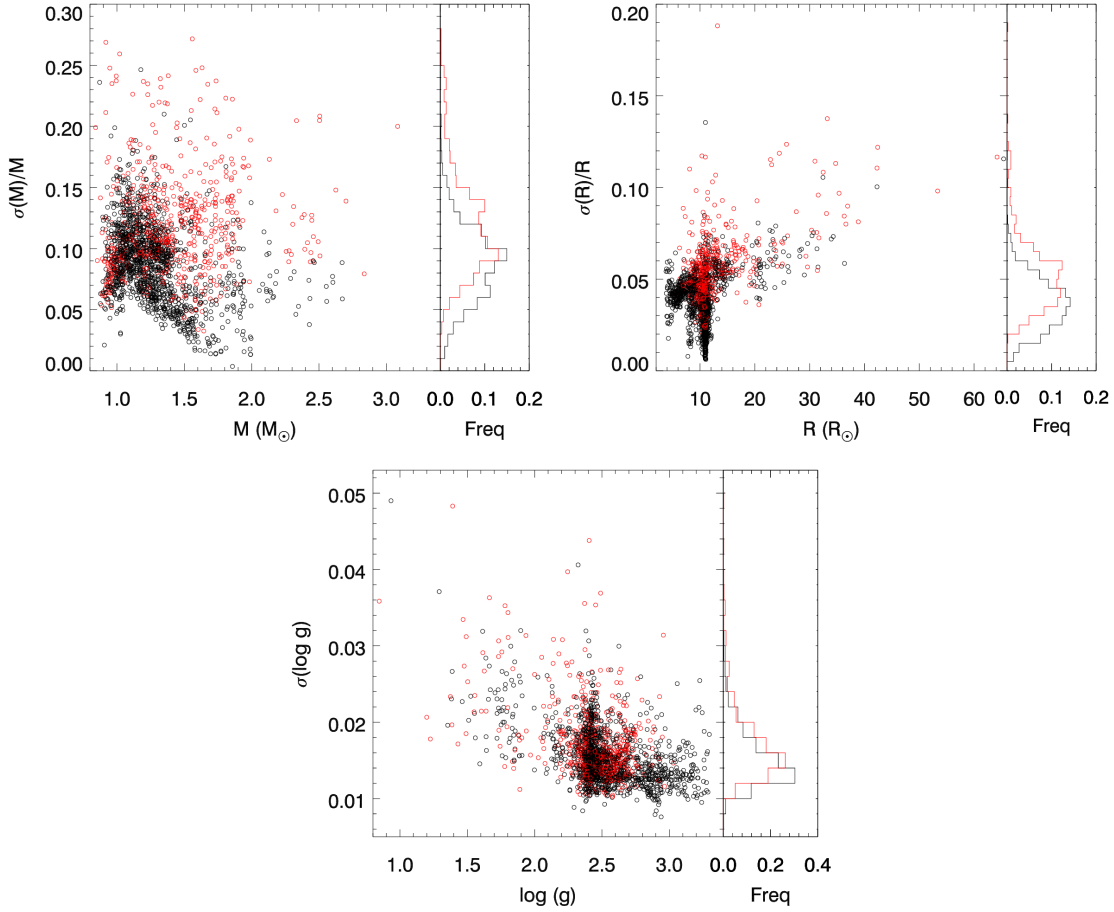
Figure 2.3: Distributions of relative (left and middle panels) and absolute (right) uncertainties for the stars in the sample, for the quantities derived in Step 1 (Sec. 2.2.1) – namely mass, radius, and $\log g$. Black dots are stars with single-peaked PDFs, red dots are with broad/multiple-peaked ones. The right sub-panels show histograms of these uncertainty distributions.

It is worth noting that the PDFs for $\mathcal{M}$ and R are usually asymmetric, although

they are derived from parameters with assumed Gaussian-distributed uncertainties. Uncertainties in mass have a median of $\sigma(\mathcal{M})/\mathcal{M} = 0.09$. More important in the context of this work is that the PDFs for R and $\log g$ are usually quite well-constrained, with median values of $\sigma(R)/R = 0.040$ and $\sigma(\log g) = 0.015$ dex, respectively. The full distribution of relative and absolute uncertainties is presented in Fig. 2.3.

Fig. 2.4 shows a small set of stars for which the PDFs are extremely broad, and present multiple peaks. A large number of such situations appear in our results; a total of ~ 600 out of 1989 stars. These stars are indicated as red dots in Fig. 2.3. These cases happen more frequently in the upper part of the color-magnitude diagram, where confusion between stars in different long-lived evolutionary stages is possible, for instance: confusion between stars in the RGB and RC, between the RC and the RGB-bump, and between the asymptotic giant branch bump and upper RGB. Such confusion happens simply because the typical distance between such evolutionary stages, both in the ν_{max} versus $\Delta\nu$ plane and in the H–R diagram, is small and comparable to the error bars, as can be seen in Fig. 2.1.

As a rule, multiple peaks are often present in $\mathcal{M}$ and R PDFs, but rarely in $\log g$. This happens because $\log g$ is a direct output of ν_{max} (see also Gai et al., 2011). The most likely values for $\mathcal{M}$ and R may turn out to be poorly defined in these cases, which will reflect on the results of the next section.

The situation is much improved for stars in which ΔP – and hence the evolutionary stage – is measured. These stars often present single-peaked PDFs, although the compact nature of the RC in the ν_{max} versus $\Delta\nu$ diagram, and the presence of a slight halt in the RGB evolution at the RGB-bump, may still cause the presence of broad and multiple-peaked PDFs.

We recall that our results compare very well with the results of the direct method, as shown in Fig. 2.5. In the direct method, the mass, radius, and $\log g$ are calculated directly by the scaling relations in Eq. 2.1, and their uncertainties by a simple propagation of the involved uncertainties. For comparison, these values are also plotted with the Bayesian ones in Figs. 2.2 and 2.4 (black triangles). Their relative (median) uncertainties are $\sigma(\mathcal{M}_{\mathrm{Dir}})/\mathcal{M}_{\mathrm{Dir}} = 0.13$, $\sigma(R_{\mathrm{Dir}})/R_{\mathrm{Dir}} = 0.055$ and $\sigma(\log g_{\mathrm{Dir}}) = 0.012$ dex. Since the Bayesian method constrains the derived parameters to be within the grid provided by the stellar models, its uncertainties are, in general, smaller than those provided by the direct method (by a factor of ~ 1.4 in radius, see also Gai et al., 2011). It is also interesting to note the much smaller spread in the parameters of stars at $\log g \simeq 2.4$, $R \simeq 10\ R_\odot$, which correspond to the RC. Just a handful of outliers are observed in Fig. 2.5; they correspond to stars with high relative uncertainties ($\gtrsim 0.2$) in their seismic parameters. The mean differences of the parameters between both methods are $(\mathcal{M}_{\mathrm{Dir}} - \mathcal{M}_{\mathrm{Bay}})/\mathcal{M}_{\mathrm{Bay}} = -0.003 \pm 0.004$, $(R_{\mathrm{Dir}} - R_{\mathrm{Bay}})/R_{\mathrm{Bay}} = 0.003 \pm 0.002$ and $(\log g_{\mathrm{Dir}} - \log g_{\mathrm{Bay}}) = 0.0020 \pm 0.0004$ dex.

Our results also compare very well with the final result of the grid-based models
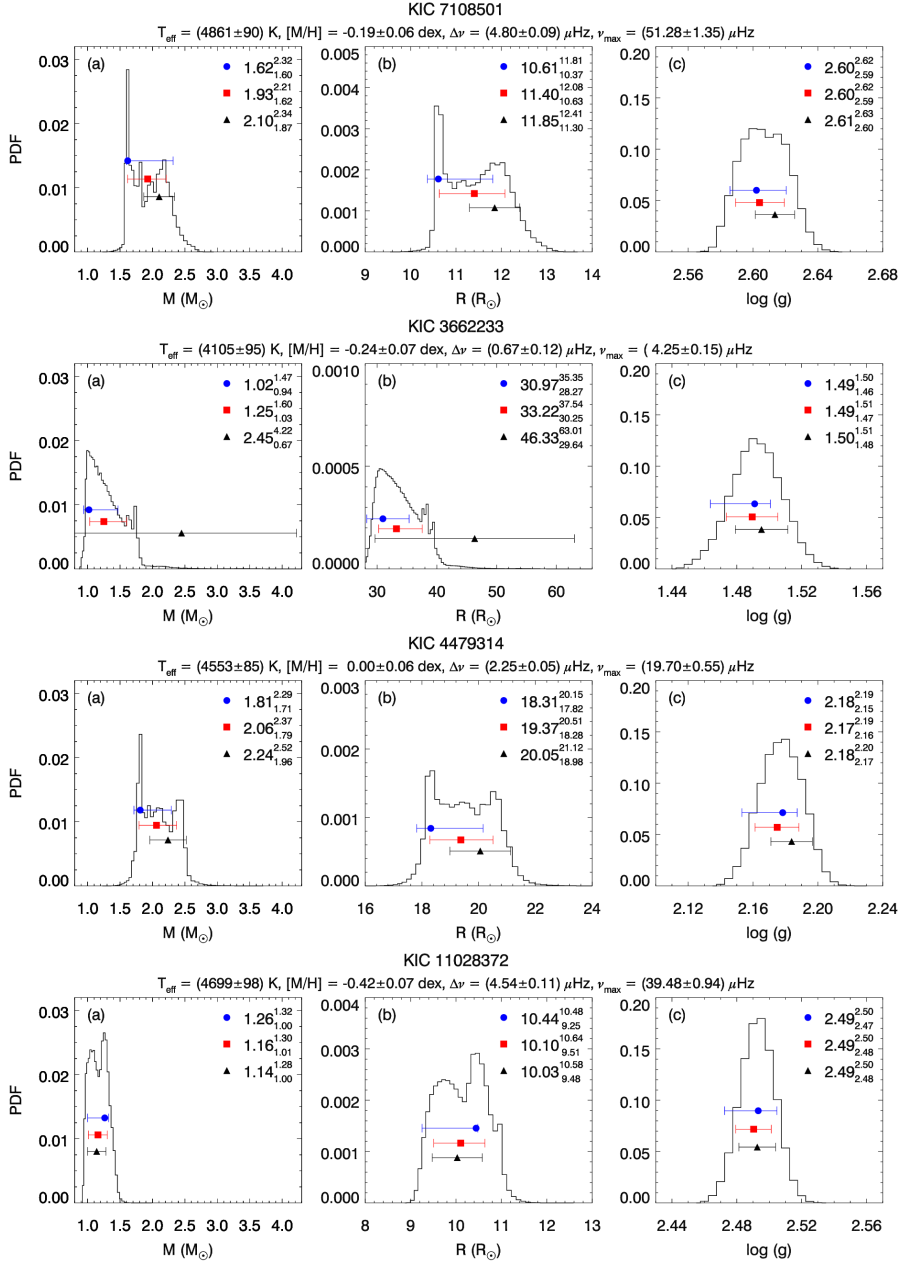
Figure 2.4: The same as in Fig. 2.2, but for some stars with broad and/or multiple-peaked PDFs.

presented in the APOKASC catalogue (Pinsonneault et al., 2014). These authors employed the Bellaterra Stellar Properties Pipeline (Serenelli et al., 2013), the grid of the BaSTI models of Pietrinferni et al. (2004), and the corrected spectroscopic parameters, referred as Scale 2 in the catalogue paper. The mean of the relative
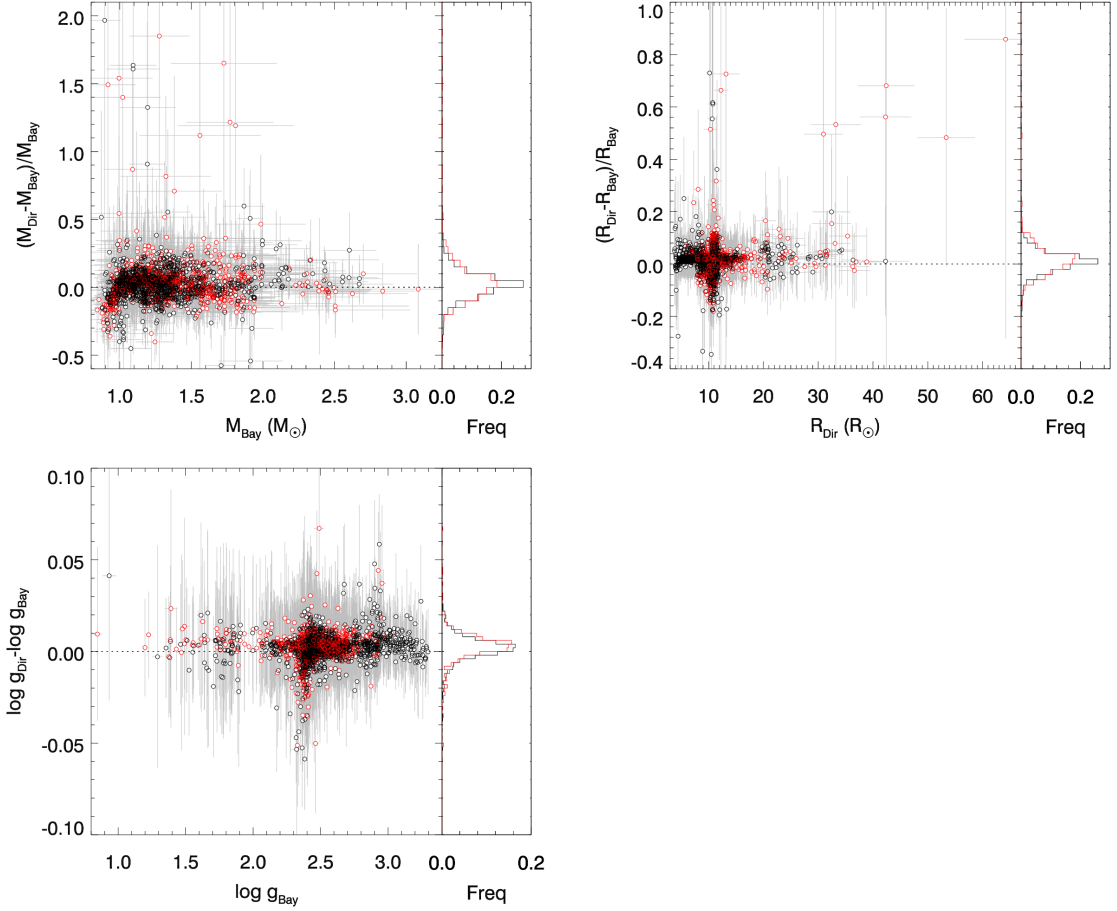
Figure 2.5: Relative (left and middle panels) and absolute (right) differences between masses, radii and log g for the stars in the sample, derived with the Bayesian and the direct methods. The dashed line is the identity line. Black dots are stars with single-peaked PDFs, red dots are with broad/multiple-peaked ones. The right sub-panels show histograms of the distribution of these differences.

differences are $(\mathcal{M}_{\mathrm{Scale2}} - \mathcal{M}_{\mathrm{Bay}})/\mathcal{M}_{\mathrm{Bay}} = 0.0003 \pm 0.0034$, $(R_{\mathrm{Scale2}} - R_{\mathrm{Bay}})/R_{\mathrm{Bay}} = 0.003 \pm 0.001$ and $(\log g_{\mathrm{Scale2}} - \log g_{\mathrm{Bay}}) = 0.0017 \pm 0.0004$ dex.

2.2.2 Step 2: Determining distances and extinctions

In the second step, we *assume* that the spectroscopically derived T_{eff} and [M/H], as well as the asteroseismic log g, are of superior quality with respect to the photometrically-derived values. This assumption is based on the fact that the results of spectroscopy

19

and asteroseismology are essentially not affected by the stellar distances and extinctions. This allows us to derive the PDFs of the absolute magnitudes, $p(M_\lambda)$, exactly in the same way as the other stellar parameters discussed in the previous section, by properly weighting the absolute magnitudes of different isochrone sections. Details about the tables of bolometric corrections used inside the isochrones are provided in Girardi et al. (2002, 2004); Bonatto, Bica & Girardi (2004); and, Marigo et al. (2008). For the ranges of T_{eff} and $\log g$ relevant to our work, the bolometric corrections are based on the library of ATLAS9 synthetic spectra from Castelli & Kurucz (2003).

Based on the above, we have the PDFs of the stellar absolute magnitudes in several passbands from Step 1. These can be used to derive distances d (in parsecs) via the distance modulus μ_0,

$$d = 10^{0.2\mu_0+1} = 10^{0.2(\mu_\lambda - A_\lambda)+1} = 10^{0.2(m_\lambda - M_\lambda - A_\lambda)+1}, \tag{2.5}$$

where μ_λ, m_λ, M_λ, and A_λ are the apparent distance modulus, apparent magnitude, absolute magnitude, and extinction in a passband denoted by λ, respectively. Assuming further that all A_λ are related by a single interstellar extinction curve expressed in terms of its V-band value (that is, $A_\lambda(A_V)$), this equation can be used to derive the total extinction, A_V, and d simultaneously. More specifically, we can derive the joint PDF: $p(d, A_V)$ or $p(\mu_0, A_V)$. We choose the second form for computational convenience, since $p(\mu_0)$ can be easily converted into a $p(d)$,

$$p(d) = \frac{5}{ln10} \frac{p(\mu_0)}{d}. \tag{2.6}$$

Since we have now obtained the PDFs of M_λ, it is easy to show that the PDF of the apparent distance modulus, $p(\mu_\lambda)$, is given by the cross-correlation between the PDF of m_λ and M_λ, assuming a normal distribution for the apparent magnitude:

$$p(\mu_\lambda) = p(m_\lambda) \star p(M_\lambda). \tag{2.7}$$

The $p(\mu_\lambda)$ is then translated by a given value of A_λ, resulting in the joint PDF of the apparent distance modulus

$$p(\mu_{0\lambda}, A_\lambda) = p(\mu_\lambda - A_\lambda), \tag{2.8}$$

which is more conveniently written as a function of the V-band extinction only:

$$p(\mu_{0\lambda}, A_V) = p\left[\mu_\lambda - A_\lambda(A_V)\right]. \tag{2.9}$$

Finally, when all the passbands are combined, the result is a joint PDF for the distance modulus and extinction,

$$p(\mu_0, A_V) = \prod_i p(\mu_{0\lambda_i}, A_V). \tag{2.10}$$

The best agreement between $p(\mu_{0\lambda})$ will occur for a particular value of extinction that maximizes $p(\mu_0, A_V)$. This allows us to estimate the extinction simultaneously with the distance modulus. The implicit assumption that we have to make is that the extinction curve – i.e., the coefficients A_λ/A_V – is well known for every star.

For the filters considered in this work, extinction coefficients are computed as described in Girardi et al. (2002, 2008), after adopting the Cardelli, Clayton & Mathis (1989) and O'Donnell (1994) extinction curve with $R_V = A_V/E(B-V) = 3.1$. We adopt, for each star, the extinction coefficients derived for the measured T_{eff} and $\log g$, and for the solar metallicity. This is a fairly good approximation, indeed. For instance, changes of 250 K in T_{eff}, 0.2 dex in $\log g$, and 0.5 dex in [M/H], cause changes in the A_g/A_V coefficient of just ~ 0.003, and even smaller changes for redder passbands.

Following this procedure, we computed $p(\mu_0, A_V)$ for a range of A_V varying from -0.5 to 1.0 mag, in steps of 0.01 mag, and covering a sufficiently large range of μ_0, hence mapping the joint PDF of both parameters. The range of extinction includes negative values, which are obviously unphysical. Statistically, one should consider an infinite range for the parameters when building the PDFs, but in practice, one allows a very large range around the expected values to cover all the possible solutions with a significant probability. In this case, a small dispersion around $A_V = 0.0$ is expected, since this is a statistical method.

The entire procedure is illustrated in Figs. 2.6 and 2.7, which present the PDFs of the apparent and absolute magnitudes, apparent distance modulus, and distance modulus for the same stars as in Figs. 2.2 and 2.4, and for all available passbands as detailed in the legend. The value of A_V that provides the best agreement between all curves is indicated in panel (d), for each star.

The four left panels in Fig. 2.8 present the contour levels of distance modulus and extinction probability space, for the same stars with single-peaked $p(\mu_{0\lambda})$ of Fig. 2.6. The solid and triple-dot-dashed contours represent the 68 and 95 per cent credible regions. The dashed-blue and dotted-red lines represent the same credible interval calculated from the marginal PDF of each parameter, for the mode and median, respectively. The plus symbol is the maximum of the joint probability. What is remarkable in this plot is the excellent precision in determining the distances and A_V, with typical (median) uncertainties of $\sigma(d)/d = 0.018$ and $\sigma(A_V) = 0.077$ mag. The uncertainties in extinction and relative uncertainties in distance for the full sample are presented in Fig. 2.9.

The four right panels in Fig. 2.8 present the contour levels of $p(\mu_0, A_V)$ for the stars with multimodal PDFs of the Fig. 2.4. The effect of broad/multiple-peaked PDFs is evident: the uncertainty in distance and extinction is much larger, with the presence of secondary peaks (or 'extended islands') which represent alternative values for distance and extinction. We treat these cases exactly as before. These stars will appear with larger uncertainties in our final catalogue.
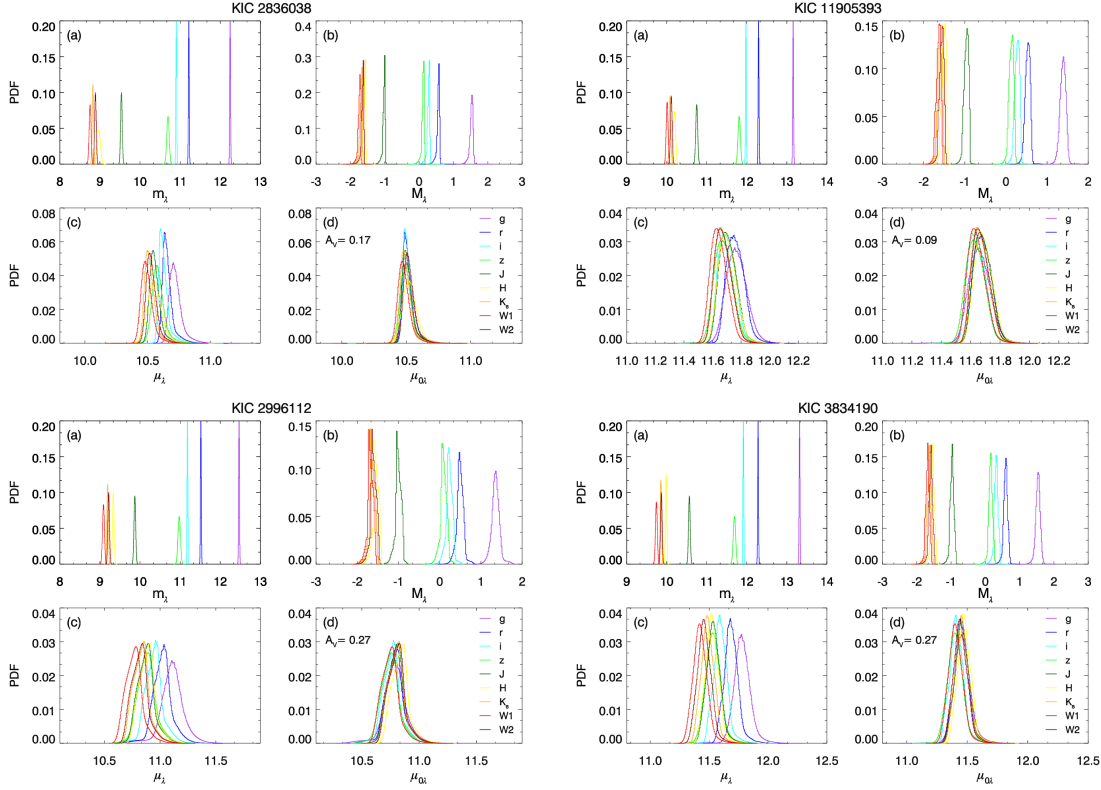
Figure 2.6: (a) PDF of the apparent magnitude, (b) absolute magnitude, (c) apparent distance modulus, and (d) distance modulus for the same stars as in Fig. 2.2, and for all available passbands as detailed in the legend. The best fitting extinction is indicated in panel (d).

Finally, Fig. 2.10 illustrates that our method is in a way similar to a classical 'spectral energy distribution (SED) fitting'. We find the combination of extinction and distance that fits the overall spectrum of the star (as sampled by the photometric points), but in addition, *we consider the tight constraints imposed by the asteroseismic plus spectroscopic data.* In such plots, the bulk of our stars are well-described by a single SED from the g to $W2$ passbands. There are a few cases of stars for which there appears to be a slight excess flux either in the blue or infrared portions of the spectrum, which might indicate the presence of stellar companions. The stars KIC 9479404 and KIC 10157507 present excess flux in the middle of the spectrum, which more likely indicates a problem with the photometry. Such cases will be examined in detail before the next release of the APOKASC catalogue.
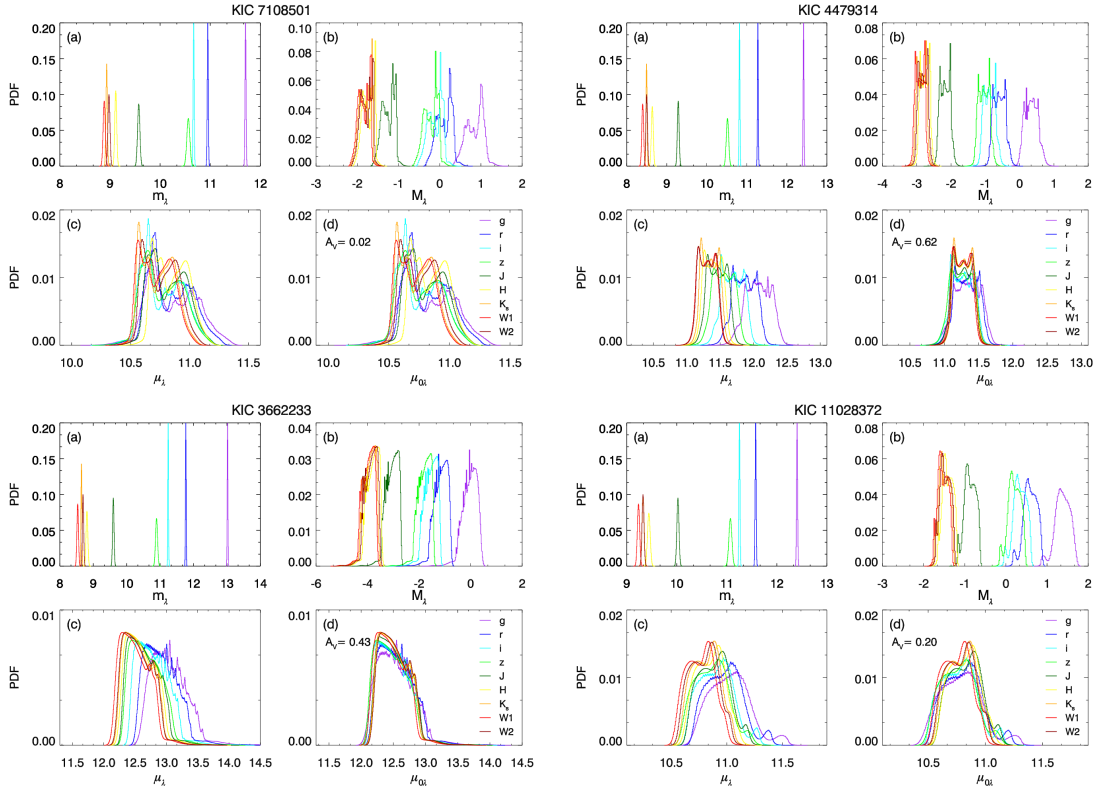
Figure 2.7: The same as in Fig. 2.6, but for the stars in Fig. 2.4.

2.2.3 Why two separate steps?

It is important to note that the entire procedure of Step 2, as summarized in Eq. 2.5, apparently does not involve anything else from Step 1 than the PDFs for the absolute magnitudes (Sec. 2.2.1), and hence it can be kept separated from the derivation of the other stellar properties performed in Step 1. In other words, we have chosen to approximate $p(\mathcal{M}, R, \log g, \tau, M_{\lambda_i}, A_V, \mu_{0\lambda_i}) \sim p(\mathcal{M}, R, \log g, \tau, M_{\lambda_i})\, p(A_V, \mu_{0\lambda_i})$. This approximation is not perfectly ideal, because Eq. 2.5 involves quantities that depend on the spectral shape – and hence on T_{eff}, $\log g$, and [M/H] – namely, the set of M_{λ_i}, and the set of A_{λ_i}/A_V. Therefore, the most correct procedure would have been a simultaneous derivation of the PDF of all stellar parameters in Steps 1 and 2, using every possible point of the parameter space $(\mathcal{M}, \tau, [\mathrm{M/H}], T_{\mathrm{eff}}, \Delta\nu, \nu_{\mathrm{max}}, m_{\lambda_i})$ in the derivation of a posterior probability for $(\mathcal{M}, R, \log g, \tau, M_{\lambda_i}, A_V, \mu_{0\lambda_i})$. The reasons why we do not follow this procedure here are: (1) to keep the required computing resources within reasonable limits; and, mainly, (2) because both effects have a limited impact in our distance estimates, as quantified below.

The full set of M_λ varies primarily as a function of T_{eff}, which is the origin of
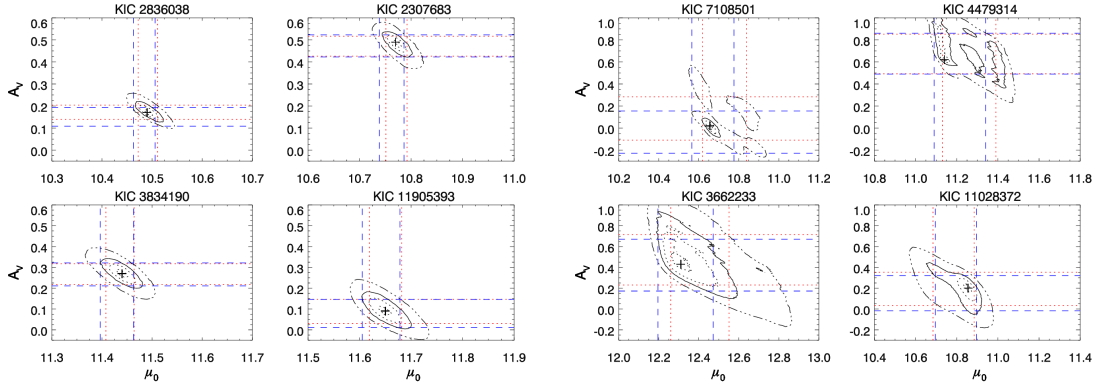
Figure 2.8: Contour levels of the distance modulus and extinction probability space, for the same single-peaked PDF stars as in Fig. 2.2 (four left panels) and the broad/multiple-peaked PDF stars as in Fig. 2.4 (four right panels). The solid and triple-dot-dashed contours represent the 68 and 95 per cent credible regions. The dashed blue and dotted red lines represent the 68 per cent credible interval for the mode and median of both A_V and μ_0. The plus symbol is the maximum of the joint probability.
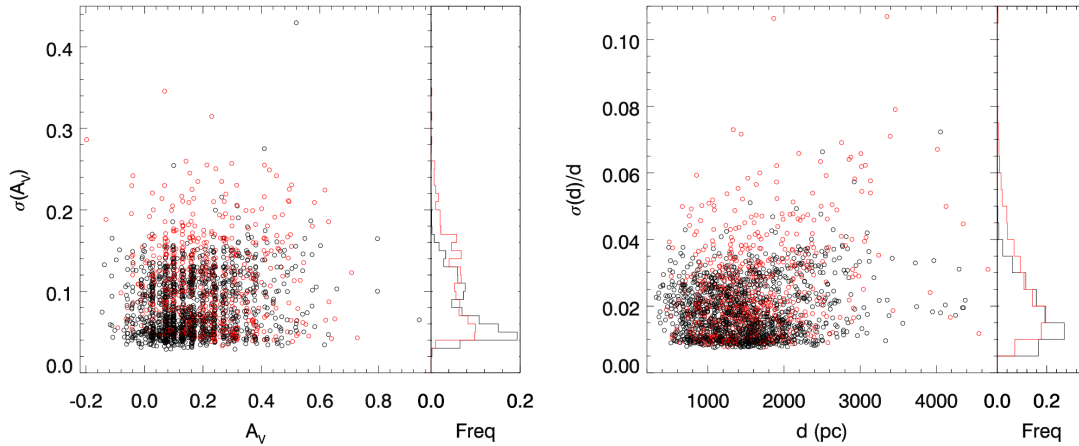
Figure 2.9: The same as in Fig. 2.3, but for the quantities derived in Step 2 (Sec. 2.2.2) – namely A_V and d.

the well-known $T_{\rm eff}$–color relations. So stars with different $T_{\rm eff}$ ranges will result in systematically different sets of intrinsic colors (in Step 1). This may be mistaken by different values of reddening and hence A_V, which impacts the distances. This is likely the mechanism that, for stars with multiple-peaked PDFs, result in alternative peaks in the (A_V, μ_0) plane in Fig. 2.8. These cases comprise of less than 30 per cent of our sample. For stars with single-peaked PDFs, we have investigated the effect
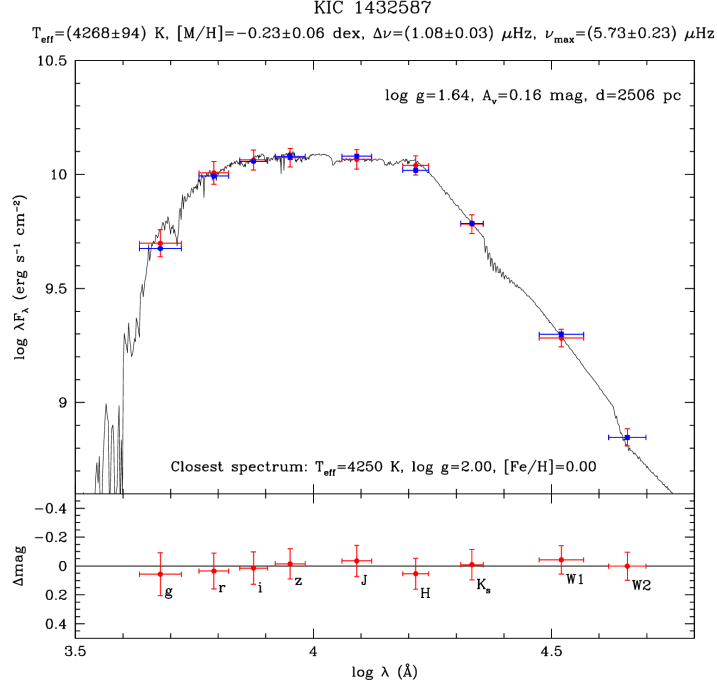
Figure 2.10: Example of the 'SED fitting' being performed by our method. Top panel: The plotted spectrum represents the flux (or, better, λF_λ) at the stellar surface, for the entry in the ATLAS9 data base with the closest value in T_{eff}, $\log g$, and [M/H], as the observed star; it is shown for illustrative purposes only. The red dots represent the absolute magnitudes of the star, as inferred from the asteroseismic plus spectroscopic constraints, and converted to the same flux scale as the spectrum. Vertical error bars represent the 68 per cent CI interval, while the horizontal error bars are simply indicating the approximate spectral range of each filter. The blue dots with error bars are the same but for the observed magnitudes, after corrected by the inferred (mode) distance and extinction. Bottom panel: The difference between the inferred magnitudes and the observed ones, as a function of wavelength.

of a 100 K *systematic change* in the T_{eff} scale in Sec. 2.2.7, which in turn produces a small, although non-negligible effect, in the extinction value. Since the typical uncertainties in our T_{eff} are $\sim$86 K (2 per cent), it is unlikely that the variations of M_{λ_i} with T_{eff} (internally to the Bayesian method) can have such a large impact on the final results.

The extinction coefficients A_λ/A_V are also a function of the spectral shape, and hence of T_{eff}, $\log g$, and [M/H] (see e.g., Grebel & Roberts, 1995; Girardi et al., 2008). However, as already mentioned, the changes of A_λ/A_V with (T_{eff}, $\log g$, [M/H]), inside

25

the intervals considered in this work, are actually very small, and much less than those caused by spatial variations in the interstellar extinction law (Zasowski et al., 2009).

2.2.4   Comparison with a direct method

Distances and extinctions can also be derived in a more direct way, starting from the stellar parameters provided by the direct method with Eq. 2.1. Essentially, we enter the R and T_{eff} in Eq. 1.1 to derive L, which is then transformed into a bolometric absolute magnitude, and into the absolute magnitude in several filters using the bolometric corrections (BC_λ) inferred from our library of synthetic stellar SEDs. These are then processed through Step 2 of our method, which allows us to identify the distance and extinction, d_{Dir} and $A_{\mathrm{V,Dir}}$, that best fit the set of observed apparent magnitudes. Error bars are obtained by simply propagating the uncertainties in the quantities R, T_{eff}, and BC_λ, into the absolute magnitudes. The final uncertainties in d_{Dir} and $A_{\mathrm{V,Dir}}$ are derived given by the joint PDF, exactly as in the Bayesian method. The median uncertainties turn out to be $\sigma(d_{\mathrm{Dir}})/d_{\mathrm{Dir}} = 0.038$ and $\sigma(A_{\mathrm{V,Dir}}) = 0.15$ mag, respectively.
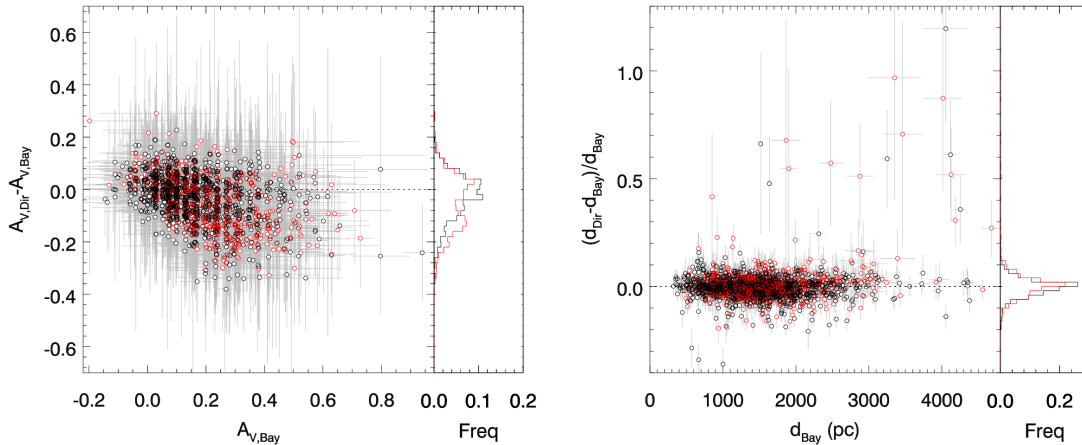
Figure 2.11: Relative (left panel) and absolute (right) differences between extinctions and distances for the stars in the sample, derived with the Bayesian and the direct methods. The dashed line is the identity line. Black dots are stars with single-peaked PDFs, red dots are with broad/multiple-peaked ones. The left sub-panels show histograms of the differences.

Fig. 2.11 shows a comparison between these distances and extinctions with those obtained with the Bayesian method. It is readily evident that they compare well with mean differences $(d_{\mathrm{Dir}} - d_{\mathrm{Bay}})/d_{\mathrm{Bay}} = -0.009 \pm 0.001$ and $(A_{\mathrm{V,Dir}} - A_{\mathrm{V,Bay}}) =$

-0.032 ± 0.004 mag. The large dispersion in extinctions is due the broad PDFs provided by the direct method, which allow a high-probability matching to a wide range of extinctions.

2.2.5 Impact of knowing the evolutionary stage

Stellar parameters derived via the Bayesian method are 'forced' to be consistent with the grid of evolutionary tracks being used. This results in smaller uncertainties, which are, typically, a factor of $\sim$2.1 smaller for the Bayesian method than for the direct method. There are, however, situations in which the Bayesian method produces distance uncertainties similar to the direct method. This happens, in general, for stars with broad and multipeaked PDFs, which often arise from the star being compatible with either a RC or a RGB star.

Fig. 2.12 illustrates the impact of knowing the evolutionary stage on the joint μ_0–A_V PDFs of two stars, classified as CLUMP and RGB in the APOKASC catalogue, respectively. As can be seen, if we assume these stars have an 'unknown' classification (red contours), their μ_0 PDFs (bottom panels) are clearly bimodal. When we adopt the correct CLUMP classification (black contour) for the RC star KIC 11295720, the peak with the larger distance and extinction is favoured (middle-left panel). If the classification was not available, the peak corresponding to RGB models would have been favoured (bottom-left panel), producing distances $\sim$10 per cent smaller. Curiously, the direct method would have indicated a distance intermediate between those two (the 68 per cent CI being between $\mu_0 = 11.06$ and 11.21 mag), although more similar to the 'wrong' solution. A similar situation – but working in the opposite sense – occurs for the RGB star KIC 9772366, which has its derived distance increased by $\sim$15 per cent when assigned an unknown evolutionary stage. Such significant changes in the distances and extinctions were found for 2 per cent (6 out of 291) of the stars classified as RC, and for 3 per cent (5 out of 199) of those classified as RGB.

Since the initial release of the APOKASC catalogue contains a large number of stars without ΔP measurements in the interval of $\log g < 2.5$, for which confusion between RC and RGB stages can easily occur, it is possible that similar situations are actually present in the catalogue, leading to an increased scatter in our derived distances. Such scatter is likely to be reduced in future versions of the catalogue, when more asteroseismic classification information becomes available.

2.2.6 Effect of distance priors

Since the basic stellar properties derived from $\nu_{\max}$, $\Delta\nu$, T_{eff}, and [M/H] are independent of distance, we have not applied any distance prior in our method. We can, however, estimate the maximum effect that different distance priors would have had,
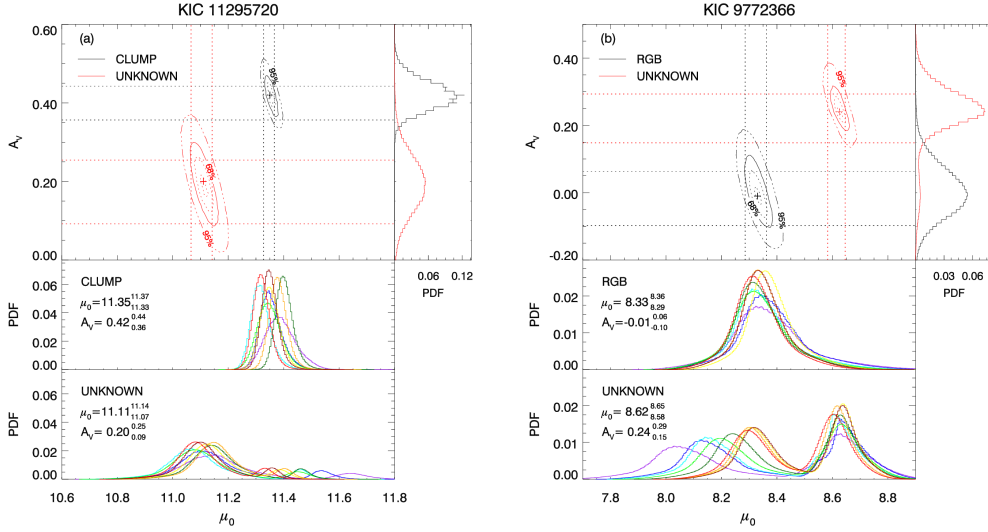
Figure 2.12: Examples of the joint (μ_0,A_V) and marginal A_V PDFs (top panels) of two stars for which we know the evolutionary stage classification, either using this information (black contours), or not using it (red contours). The solid and triple-dot-dashed contours represent the 68 and 95 per cent credible regions. The dotted lines represent the 68 per cent credible interval for the mode of both A_V and μ_0. Their $\mu_{0\lambda}$ PDFs with 'unknown' and 'known' evolutionary stage classification are shown in the bottom and middle panels, respectively.

were the distances fully incorporated into the Bayesian part of the method. For this, we have multiplied the distance PDFs by functions of the form

$$p(d) \propto \exp\left(-\mathcal{R}/\mathcal{R}_s\right), \quad p(d) \propto \exp\left(-z/z_s\right)$$

or a combination of both, where $\mathcal{R}$ and z are the Galactocentric radius and height above the plane, respectively. These represent the spatial distribution of stars expected in the MW's stellar disk. We adopted as scale factor $\mathcal{R}_s = 2600$ pc, and two extreme values of z_s, namely $z_s = 100$ pc and $z_s = 900$ pc. These span the possible range of z_s in going from a young thin disk (e.g., Maíz-Apellániz, 2001) to the thick disk (Jurić et al., 2008).

The effect of these multiplicative functions on the PDF medians and modes is very modest, namely: less than 1 per cent changes in the distances for the bulk of the stars, increasing to maximum values of ~ 4 per cent for stars with broad and/or multiple-peaked PDFs. Since these changes are typically smaller than the 68 per cent CI, we can conclude that including prior information on the distances is not worthwhile at this stage.

2.2.7 Effect of systematic shifts in T_{eff} and [M/H]

We simply assume that observed stars are well-described by current evolutionary tracks of single stars, which is reasonable as a first approximation. However, it is well known that evolutionary tracks frequently present systematic offsets in the H–R diagram, and especially in the T_{eff} scale of the red giants. This happens primarily because of the approximations used to model the energy transport by convection, such as mixing length theory. In our case, we use evolutionary tracks in which the mixing length parameter is calibrated on a solar model and then applied to all stars (see Bressan et al., 2012). This approach could cause systematic offsets in the T_{eff} scale of the models.

We explore the possible effect of such offsets by applying the same methods with a grid of stellar models shifted by $\Delta T_{\mathrm{eff}} = +100$ K. The main effect of this shift is that the Bayesian method compares the observed stellar parameters with older/metal-poorer isochrones, causing a mismatch between the derived and the observed stellar SED, which is compensated by an additional extinction. On average, we obtain a change of $A_{V,\Delta T_{\mathrm{eff}}} - A_V = 0.062$ mag. This also slightly impacts the derived distances, which are decreased by $(d_{\Delta T_{\mathrm{eff}}} - d)/d = -0.017$, corresponding to $\sim 0.9\sigma(d)/d$.

Systematic offsets between the model and data metallicity scales are also possible. We have tested the method applying a systematic shift of Δ[M/H] $= +0.1$ dex to the models, which makes the Bayesian method match the observed stellar parameters with younger/metal-richer isochrones. The effect in this case is to produce smaller extinctions with a mean value of $A_{V,\Delta[\mathrm{M/H}]} - A_V = -0.062$ mag, and to slightly increase the distances by $(d_{\Delta[\mathrm{M/H}]} - d)/d = 0.004$. Moreover, in this case we found that a large number of stars have $\mu_{0\lambda}$ PDFs that are better matched with negative A_V: ~ 8 per cent have $A_{V,\Delta[\mathrm{M/H}]} \leq -0.05$ mag, and ~ 12 per cent have -0.05 mag $< A_{V,\Delta[\mathrm{M/H}]} \leq 0.0$.

Since systematic offsets of this order of magnitude are perfectly possible, they can be taken as a rough indication of the possible systematic errors in our distance and extinction estimates.

As the typical uncertainties in spectroscopic ASPCAP metallicity in the APOKASC sample are of $\sigma([\mathrm{M/H}]) \simeq 0.06$ dex, the experiment of applying Δ[M/H] $= +0.1$ dex also gives us an indication about the maximum changes we would have in our distance and extinction estimates, if we had adopted a metallicity prior in the Bayesian method. Indeed, higher metallicities are much more likely in the sample, and could have been more weighted by applying a suitable prior. It is very unlikely, however, that the method would have favoured models more than 2σ (0.12 dex) away from the measured [M/H], which is about the size of the 0.1 dex shift explored here.
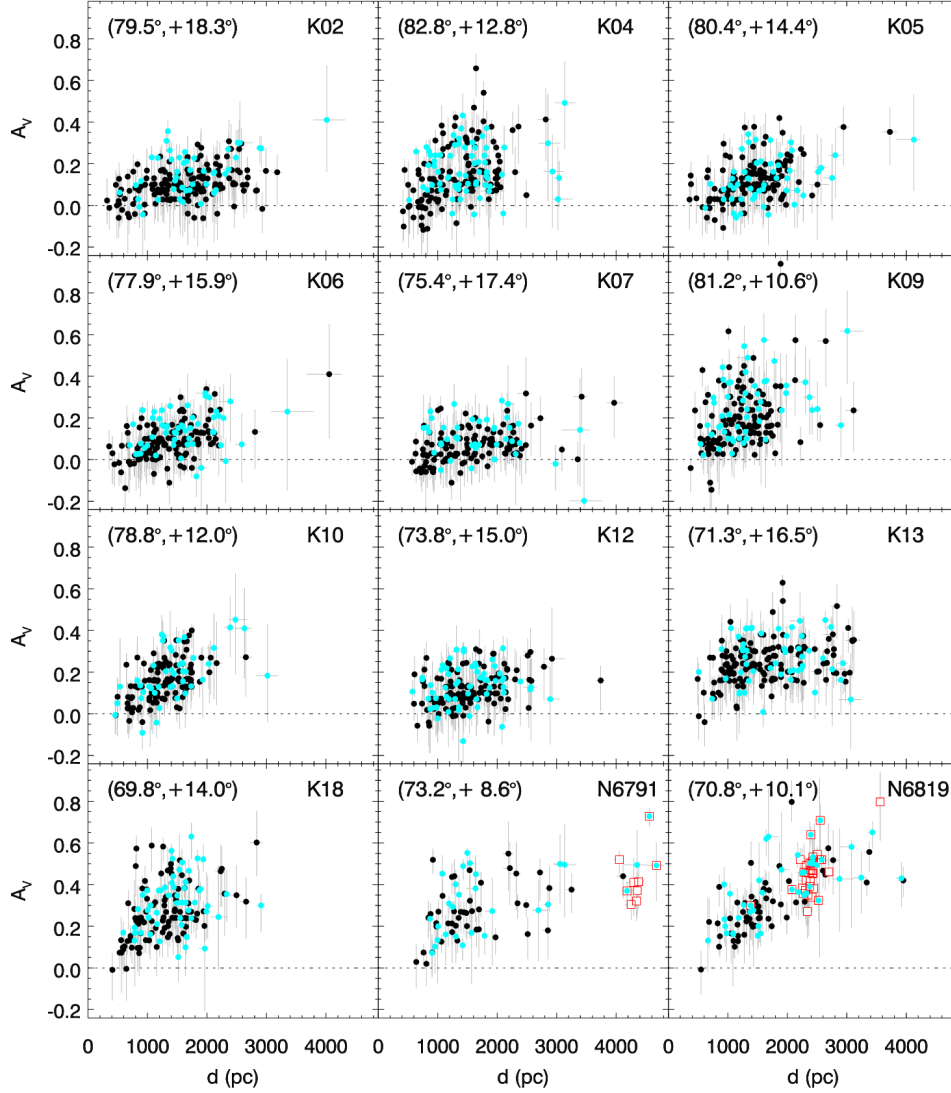
Figure 2.13: A_V versus distance (d) for the APOKASC fields indicated in Fig. 1.1. The Galactic coordinates of field centers are indicated in the top-left of each panel. The cyan dots are stars whose $\mu_{0\lambda}$ PDFs are broad or multiple-peaked. The small red squares are stars that likely belong to the star clusters NGC 6791 and NGC 6819.

2.2.8   Typical distances and extinction maps

Fig. 2.13 shows A_V versus distance (d) for all fields showed in Fig. 1.1. This figure indicates that most of the observed stars are located within 2 kpc, whereas almost all stars are within 4 kpc. The cyan dots are stars with broad/multiple-peaked

$\mu_{0\lambda}$ PDFs, and hence with more uncertain locations. Note that some stars ($\sim$6 per cent) have $\mu_{0\lambda}$ PDFs that are better matched with slightly negative A_V. As shown in Fig. 2.14, there is a trend for stars at larger distances to be cooler than the nearest ones, which is consistent with them being more luminous. Also, high extinction stars (with, say, $A_V > 0.4$ mag) are observed at larger distances (Figs. 2.13 and 2.14). These plots indicate the potential of APOKASC data to provide improved 3D dust extinction maps in the *Kepler* fields (see also Zasowski, 2014).
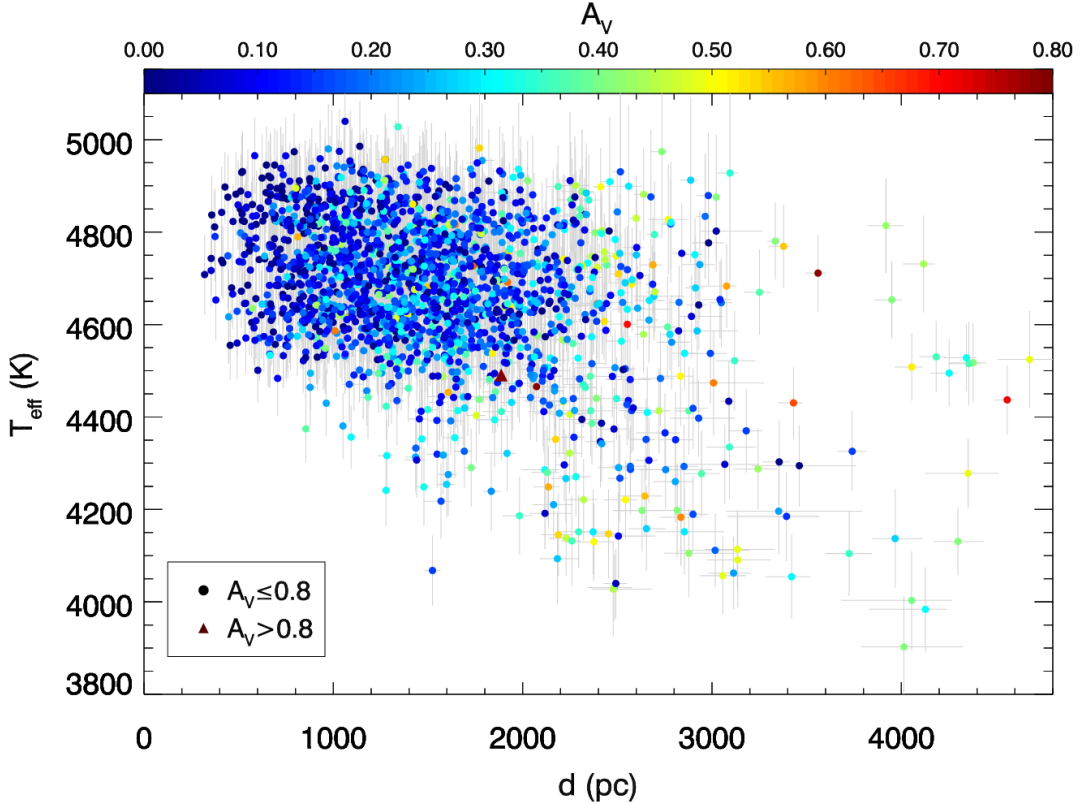
Figure 2.14: Correlation between $T_{\rm eff}$, distance, and A_V.

The distance distribution of APOKASC stars results from a series of factors, comprising the many criteria used to select *Kepler* targets, the actual determination of their asteroseismic parameters, and the target prioritization by APOGEE (Zasowski et al., 2013; Pinsonneault et al., 2014). Discussion of this distribution is postponed to future papers. We note that a large fraction of the targets are RC stars, which in the *Kepler* field are preferentially observed within distances of 6 kpc (Bovy et al., 2014).

Fig. 2.15 compares the extinction maps from this work with those derived from the KIC (Brown et al., 2011), from Schlegel, Finkbeiner & Davis (1998, hereafter
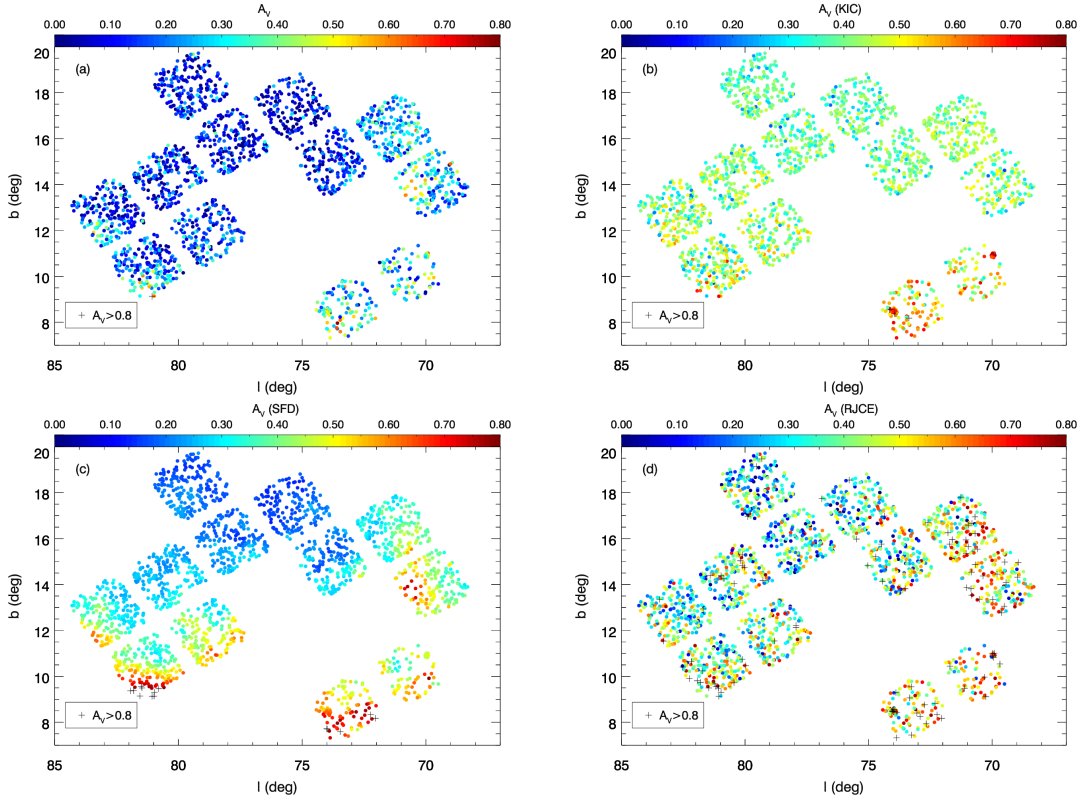
Figure 2.15: (a) Our extinction map as compared to (b) KIC, (c) SFD, and (d) RJCE. Extinctions greater than 0.8 mag are represented by a plus symbol. See text for more details.

SFD), and with the Rayleigh-Jeans Color Excess (RJCE, Majewski, Zasowski & Nidever, 2011) method. The comparison with the KIC extinction map will be commented further down in this section. The comparison with SFD shows some evident similarities in the position of the highly-extincted regions; the SFD extinctions tend to be much larger than our values, especially in low-latitude fields. This is expected since SFD gives the extinction at infinity, and not along the line-of-sight to every star. Indeed, the excess in the SFD extinction is larger along lines-of-sight close to the Galactic plane, where substantial interstellar material exists between our target stars and infinity. In addition, there are claims that SFD maps overestimate the extinction for regions with $A_V > 0.5$ mag anyway (Arce & Goodman, 1999).

The comparison with RJCE deserves some additional explanation. RJCE uses the color excess in $H - W2$ to derive the extinction in the K_s band, A_{K_s}. Since it uses only infrared measurements, it is especially useful to derive extinction values in the regimes of high extinction (say, for $A_V \gtrsim 1$ mag) that frequently happen towards the Galactic bulge and across the Galactic mid-plane (see also Schultheis
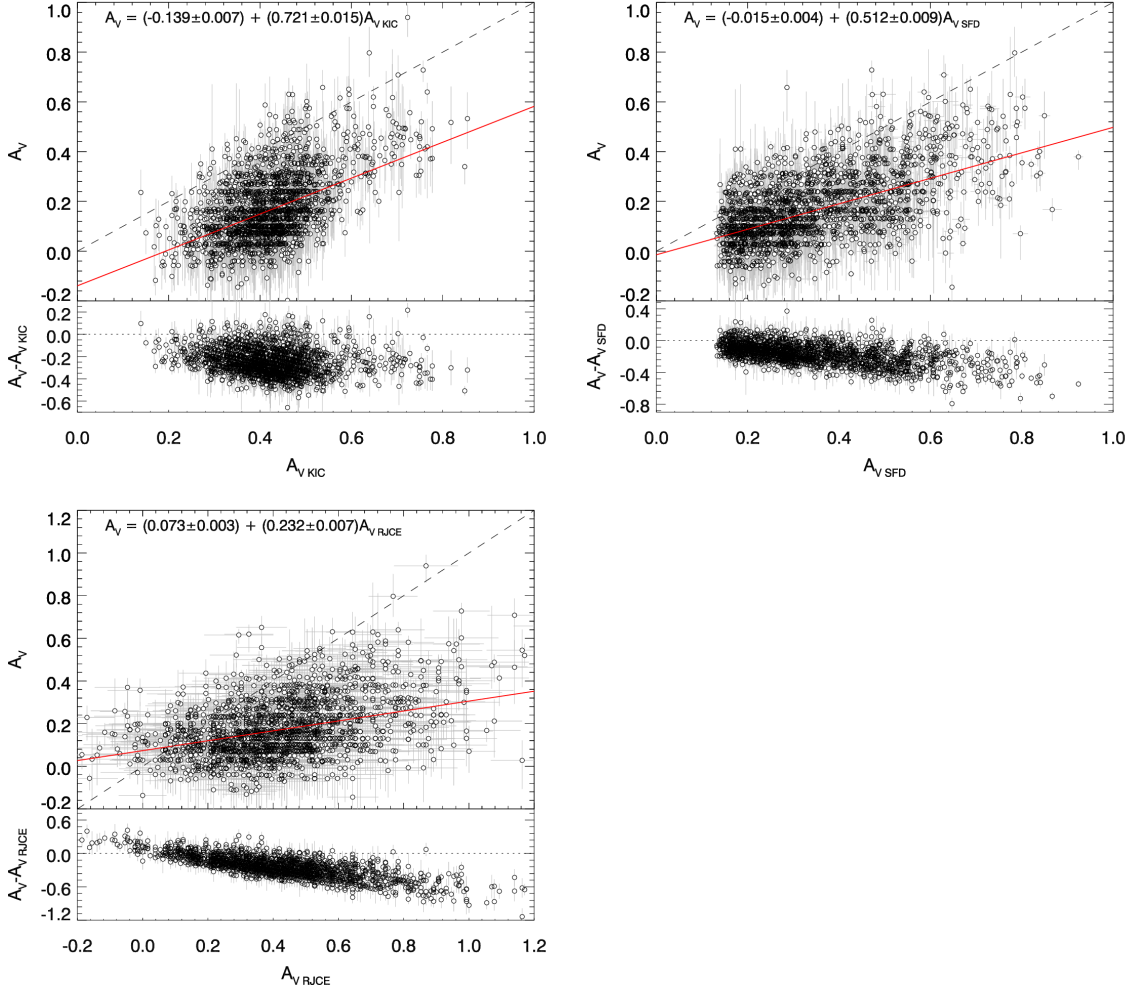
Figure 2.16: Comparisons between our A_V values, with KIC (left panel), SFD (middle), and RJCE (right) extinctions for the sample. The dashed black and solid red lines represent the identity line and the weighted least-squares fit, respectively. The bottom sub-panels show the absolute differences.

et al., 2014). In the case of the APOKASC stars, extinction values are never that large, and the typical values of A_{K_s} derived with RJCE are of just ~ 0.025 mag. These low values of A_{K_s} are then multiplied by 8.45 to convert them to A_V. These two facts – the use of only two photometric measurements, plus the amplification of uncertainties when converting A_{K_s} to A_V – is likely to cause a significant dispersion in the RJCE-derived A_V values of slightly-reddened stars, exactly what we observe in Fig. 2.15. Our extinction maps turn out to be somewhat smoother than the RJCE's; in addition, they also tend to present smaller A_Vs. It is interesting to

note that RJCE produces larger extinction values towards the high-latitude fields of *Kepler*, where both our and the SFD maps exhibit relatively low extinction values. The origin of this discrepancy will be investigated in a future paper.

Fig. 2.15 also indicates that our A_V are valid solutions for the extinctions, since they show close-to-null mean values in the top half of the *Kepler* field, at higher latitudes, in rough agreement with the near-absence of dust shown by the SFD maps.

Fig. 2.16 shows comparisons between our A_V and KIC, SFD, and RJCE extinctions for the full sample, together with the fitted linear relations between them. Such linear fits could be used to infer the expected extinctions for other *Kepler* stars, still not observed by APOKASC. The zero-points in the derived linear relations between A_V and $A_{V,\mathrm{SFD}}$, and between A_V and $A_{V,\mathrm{RJCE}}$ are close to null. Null zero-points can be interpreted as a first evidence that systematic errors, although possible, are probably smaller than those explored in Sec. 2.2.7.

It is clear that the KIC extinctions appear overestimated with respect to our values. The rms deviation around the linear fit presented in Fig. 2.16 (left panel) is 0.12 mag. If we assume that both are simply proportional to each other (i.e., with no zero-point offset), we obtain that

$$A_V = (0.409 \pm 0.003)\, A_{V,\mathrm{KIC}}. \tag{2.11}$$

with a mean rms deviation of 0.12 mag around this relation.

KIC extinctions are derived from a simple geometrical model for the distribution of the dust (Brown et al., 2011), which is a useful first-order approach for many applications. In this model, the dust density is assumed to decrease exponentially with height $|z|$ above the Galactic plane, with a scaleheight of $h_{z,\mathrm{dust}} = 150$ pc, and a local extinction density of $\kappa_V = 1$ mag kpc^{-1}. Thus, we use our distance and extinction values to recalibrate the values of $h_{z,\mathrm{dust}}$ and κ_V. For each pair of values, we integrate the KIC extinction model from the Sun up to every observed star, thus obtaining new estimates of $A_{V,\mathrm{KIC}}$. For the $h_{z,\mathrm{dust}}$ and κ_V adopted by KIC, we obtain a mean difference between our A_V and the new $A_{V,\mathrm{KIC}}$ of -0.39 mag, and an rms dispersion of 0.12 mag around this mean. We then identify the pair of $h_{z,\mathrm{dust}}$ and κ_V values that minimizes the residuals between our A_V and $A_{V,\mathrm{KIC}}$. These values are $h_{z,\mathrm{dust}} = 234$ pc and $\kappa_V = 0.25$ mag kpc^{-1}. This modified model for KIC extinctions presents a null mean difference with respect to our estimates, but still a r.m.s. dispersion of 0.12 mag. This significant dispersion probably reflects the fact that dust extinction is much more patchy along the Galactic disk than assumed in these simple models.

Finally, our revised A_V values allow us to reevaluate the consistency between the different T_{eff} scales included in the APOKASC catalogue. As discussed thoroughly in Mészáros et al. (2013), the zero-point of the ASPCAP T_{eff} was calibrated so as

to coincide, on average, with T_{eff} determinations based on the IRFM calibration by González Hernández & Bonifacio (2009a), using $J-K_{\text{s}}$ colours. We can derive the IRFM T_{eff} for all APOKASC targets using the same relations, but the results will be slightly dependent on the extinction values used in the de-reddening of the observed $J-K_{\text{s}}$ colors. Using our A_V values, we find IRFM T_{eff} estimates that are systematically cooler by -74 K, on average, if compared to the ASPCAP-corrected values. Pinsonneault et al. (2014), using the KIC extinction maps, find a value of -193 K for this offset. Therefore, our smaller extinction values help to reduce, but do not completely eliminate, this systematic difference between the different T_{eff} scales.

2.2.9 Results for the star clusters

The last two panels of Fig. 2.13 show clear concentrations of stars at distances of ∼2.4 and 4.4 kpc, which are obviously caused by the star clusters NGC 6819 and NGC 6791, respectively (red squares). Stars in these clusters provide a useful check of the uncertainties in our methods, since they are expected to be located within a distance interval much smaller than the expected uncertainties. As for the extinction, both clusters spread over tens of arcmin across the *Kepler* fields, so that the star-to-star extinction may vary significantly, as indeed indicated by the vertical spread in Fig. 2.13.

Fig. 2.17 shows the distance modulus for all cluster members selected by Stello et al. (2011, same stars as red squares in Fig. 2.13), based on photometric membership by Stetson, Bruntt & Grundahl (2003) for NGC 6791, and with at least 80 per cent membership probability from the radial velocity survey of Hole et al. (2009) for NGC 6819. For NGC 6791, nine stars in APOKASC are classified as seismic members by Stello et al. (2011), and indeed there is a good overlap between their distance modulus PDFs (grey lines in panel a). The stars KIC 2435987, 2436688, and 2570214 present broad or double-peaked PDFs (cyan dots in panel a). The second star is classified as potentially affected by blending by Stello et al. (2011). Also particular is the case of the star KIC 2569055 (sixth in the plot), whose W1 and W2 magnitudes favour a slightly smaller distance.

For NGC 6819, 32 stars selected by Stello et al. (2011) are in the APOKASC sample, out of which 29 were classified as seismic members. The non-seismic members are KIC 4937011, KIC 4937257, and KIC 5023889. Fig. 2.17(b) shows the distance modulus PDFs for the 32 stars (grey lines); it is clear that the PDF of these three non-seismic members do not overlap with the others. We have verified that KIC 5023889 presents multiple-peaked PDFs, while the other two stars appear with normal PDFs. Among the other members, we find stars which are somewhat problematic, such as: KIC 4937576, 4937770, 5023732, 5024043, 5024476, 5024851, 5111940, 5112734, 5112744, 5112880, and 5113041 have broad or double-peaked
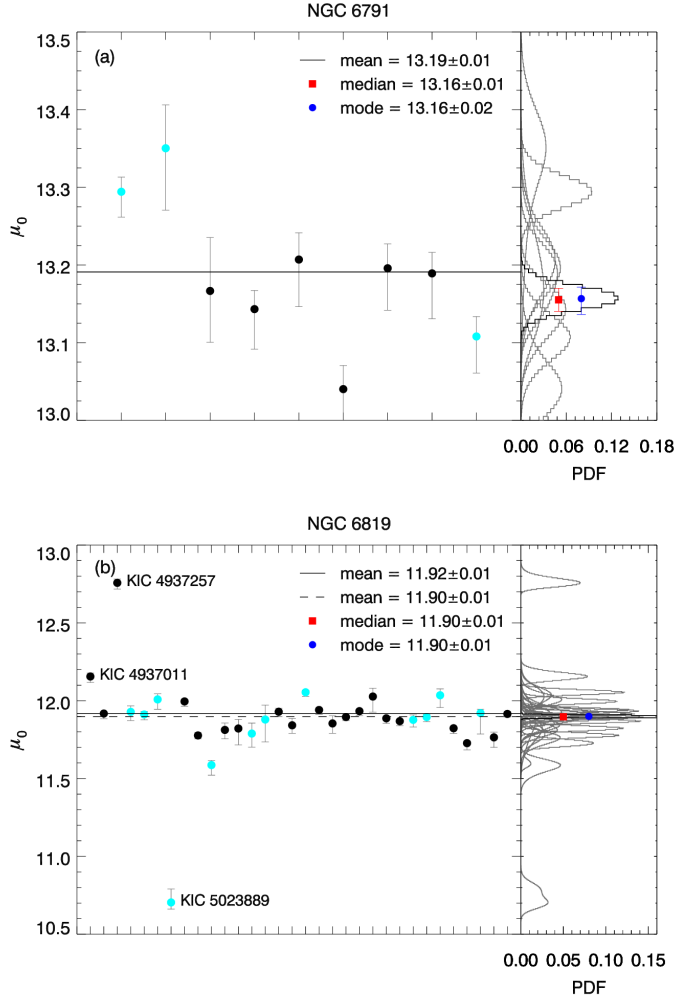
Figure 2.17: Distances derived for stars in (a) NGC 6791 and (b) NGC 6819. In both cases, the main panel shows the mode μ_0 and 68 per cent CI for all cluster members. The solid and dashed lines represent the mean weighted values for all stars, and excluding the outliers denoted by their KIC numbers, respectively (see text for more details). The cyan dots are stars whose $\mu_{0\lambda}$ PDFs are broad or multiple-peaked. The smaller sub-panels to the right show the μ_0 PDFs for all cluster members (grey lines). The black line show the results of deriving the distance modulus PDF of the cluster using the product of all individual PDFs, whose mode and median (with their 68 per cent CI) are shown by the blue and red symbols, respectively.

PDFs (cyan dots in panel b); KIC 5024476 is listed as binary likely member by Hole

et al. (2009); KIC 4937770 could be considered a binary star as argued by Corsaro et al. (2012); KIC 5112734 has a known blended star according to Stello et al. (2011); KIC 5024240 and 5024851 are binary and likely binary members with somewhat widened PDFs; KIC 5112481 and KIC 4937257 have only 2MASS and WISE photometry and hence a somewhat increased uncertainty in A_V; for KIC 5024967 the WISE photometry is probably affected by the diffraction spikes of a bright nearby star.

The black lines in the right sub-panels show the results of deriving the distance modulus PDF of the cluster using the product of all individual PDFs. The mode and its 68 per cent CI are represented by the blue symbols and the median and its 68 per cent CI, by red symbols. The mode in the μ_0 PDFs – 13.16 ± 0.02 mag and 11.90 ± 0.01 mag for NGC 6791 and NGC 6819, respectively – compare well with Basu et al. (2011) who found $\mu_0 = 13.11 \pm 0.06$ mag (4.19 ± 0.12 kpc) and $\mu_0 = 11.85 \pm 0.05$ mag (2.34 ± 0.05 kpc), respectively. They also agree very well with Wu, Li & Hekker (2014), who found $\mu_0 = 13.09 \pm 0.10$ mag for NGC 6791 and $\mu_0 = 11.88 \pm 0.14$ mag for NGC 6819. Eclipsing binaries independently indicate distance moduli of $\mu_0 = 13.01 \pm 0.08$ mag for NGC 6791 (Brogaard et al., 2011) and $\mu_0 = 12.07 \pm 0.07$ mag for NGC 6819 (Jeffries et al., 2013, assuming $E(B-V) = 0.12$ in this case).

The left main-panels show a summary of the mode and its 68 per cent CI for each star (black and cyan dots). The solid black lines represent the mean weighted values, which is a simpler way to estimate the distance modulus of the cluster without considering the shape of the PDF. The dashed black line in the (b) panel is the mean weighted value for NGC 6819 without the three non-seismic members.

The wide variety of situations we meet in stars belonging to these well-studied clusters – double-peaked PDFs, binaries, stars with incomplete photometry and/or without evolutionary status – represents situations we likely have in the entire APOKASC sample. But overall, it is quite encouraging that we find good agreement in the distances of these stars within their CI.

2.2.10 Distances to stars in the APOGEE-RC catalogue

Bovy et al. (2014) have recently released the APOGEE red clump (APOGEE-RC) catalogue, containing stars which, due to their particular values of T_{eff}, spectroscopic $\log g$, [M/H], and 2MASS $(J - K_{\mathrm{s}})_0$, are very likely RC stars with a well-defined absolute magnitude. Comparison with the *Hipparcos*-based absolute magnitude of the RC (Laney, Joner & Pietrzyński, 2012) then allows a good determination of their distances. A total of 593 such stars are presen1t in the APOKASC catalogue, and a comparison between our, and the Bovy et al. (2014) distances is presented in Fig. 2.18. The mean relative difference between them is only 0.4 per cent. Note that the comparison includes all stars common to both catalogues, which likely includes some misclassified RGB stars in Bovy et al. (2014), as well as stars with unknown evolutionary stages in APOKASC; those could easily explain the few outliers in the plot.
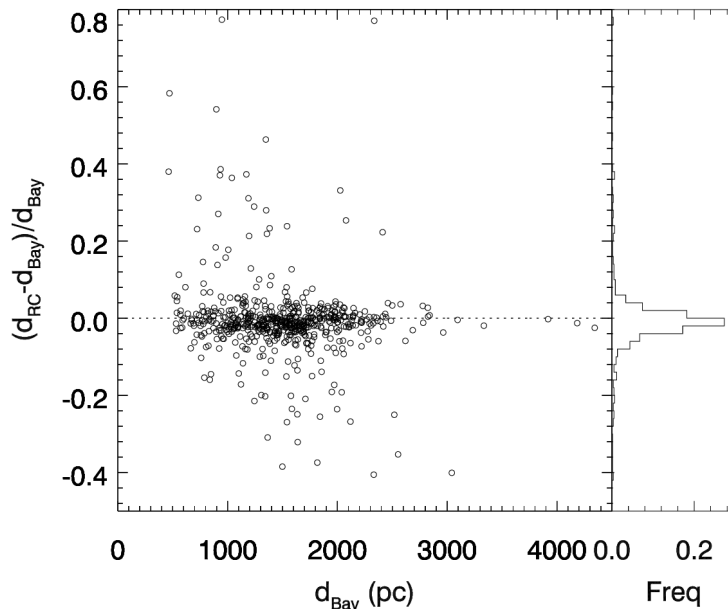
Figure 2.18: Relative difference between our Bayesian distances (d_{Bay}; mode) and the RC distances (d_{RC}) derived by Bovy et al. (2014). The dashed line is the identity line. The right sub-panel show a histogram of the distribution of this difference.

Such a tight relation between these two distance scales is remarkable, and very encouraging. It is true that both scales are expected to be somewhat correlated, because they are based on the same set of stellar models from Bressan et al. (2012) to describe the behaviour of the RC as a function of metallicity and mass. However,

the zero-point of the Bovy et al. (2014) distances does not depend on stellar models. Moreover, the APOGEE-RC catalogue was dereddened using a method quite different from ours, namely the RJCE method by Majewski, Zasowski & Nidever (2011). The comparison between the distances obtained by the direct method (hence independent of stellar models, see Sec. 2.2.4) and the Bovy et al. (2014) distances has also produced excellent agreement, as mentioned in Bovy et al. (2014).

2.2.11   Distances to stars in the SAGA catalogue
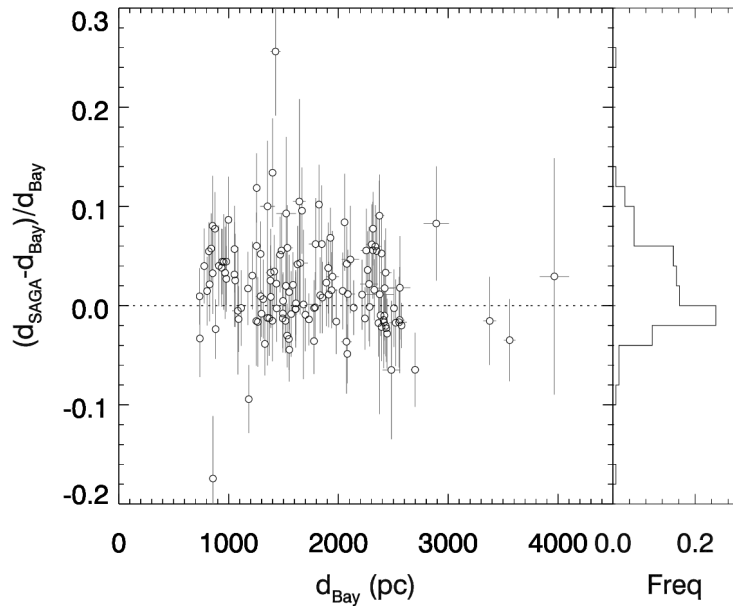
Figure 2.19: Relative difference between our Bayesian distances (d_{Bay}; mode) and the distances (d_{SAGA}) estimated in the SAGA catalog by Casagrande et al. (2014). The dashed line is the identity line. The right sub-panel show a histogram of the distribution of this difference.

We also compared our distances with those estimated in the SAGA catalogue (Casagrande et al., 2014), in which the stellar parameters are estimated in a completely independent way, using a combination of Strömgren photometry, the IRFM, and several extinction estimates. For the 136 stars in common with the APOKASC catalogue, the mean relative difference in distances is only 1.2 per cent, as shown in Fig. 2.19.

Such good agreement is surprising, considering that SAGA T_{eff} are ≈ 90 K hotter and [M/H] are ≈ 0.14 dex smaller than the calibrated ASPCAP ones. Indeed, if

we apply these zero-point shifts in T_{eff} and [M/H] in our method, the simulations in Sec. 2.2.7 indicate that we should obtain a distance scale 2.1 per cent shorter on average. It is likely that differences in the underlying methods, isochrones (and color-T_{eff} relationships), or in the extinction estimates from SAGA are affecting the results in a way that largely compensates to the offsets between the two T_{eff} and [M/H] scales.

2.3 Distances and extinctions for APOGEE DR12

In the second part of this work, we used the entire APOGEE DR12 survey (Alam et al., 2015). In addition to the 2MASS apparent magnitudes included inside APOGEE, in order to cover a wide wavelength range to constrain the spectral energy distribution and be able to estimate distances and extinctions, we gathered photometry from:

1. AAVSO Photometric All-Sky Survey (APASS) DR9 – Sloan $g'r'i'$ and Jonhson BV (Henden et al., 2015);

2. SDSS – $g'r'i'z'$ (Ahn et al., 2012);

3. WISE – $W1W2$ (3.35 and 3.6 μm, Wright et al., 2010).

We started with a catalogue with 89150 stars, which was a result of a cross-matching between the APOGEE DR12, APASS DR9 and WISE, out of 10243 stars have at least one SDSS photometry. The matching was based on 1 arcsec radius, using right ascension and declination on sphere. We disregarded stars without WISE or APASS records. We also disregarded the apparent magnitude i from APASS and SDSS, because there is a large number of stars with divergent magnitudes (see figure 2.20), most likely due to saturation in SDSS images[3].

The final APOGEE DR12 results included a recommended set of corrections intended to make the ASPCAP results consistent with the values from external checks (see Mészáros et al., 2013; Holtzman et al., 2015). We use the T_{eff}, $\log g$, and [M/H] 'corrected ASPCAP values' provided in DR12, instead of the raw ones. The T_{eff} are calibrated using the photometric relation of González Hernández & Bonifacio (2009b) based on the infrared-flux method. The [M/H] are calibrated with the literature values of [Fe/H] from ∼20 star clusters, and the red giant branch (RGB) stars have their $\log g$ calibrated with the asteroseismic gravities given by the APOKASC catalogue (Pinsonneault et al., 2014).

---

[3]http://classic.sdss.org/dr7/instruments/technicalPaper/index.html
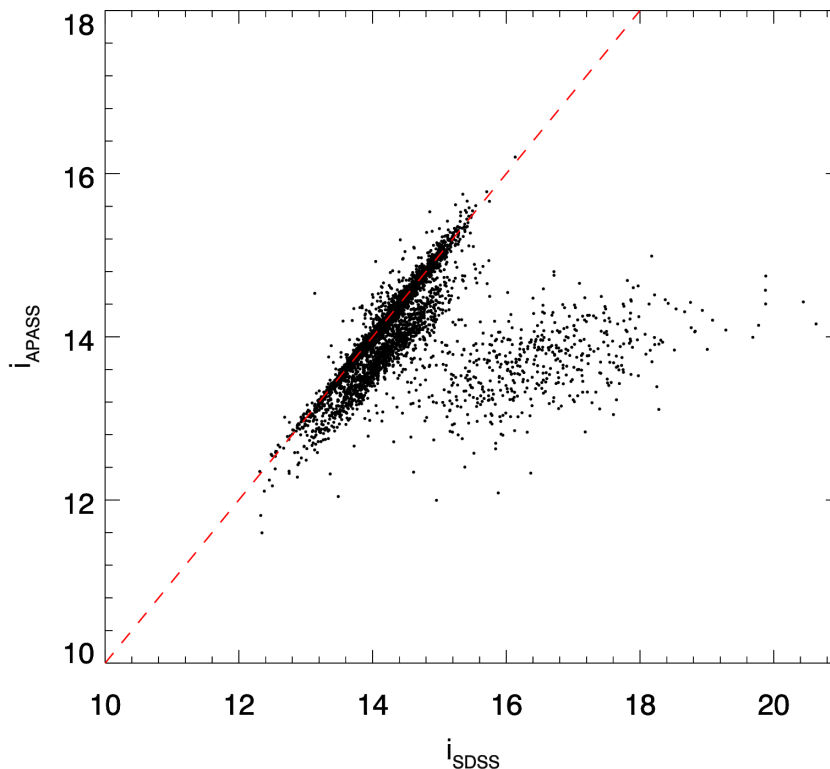
Figure 2.20: Comparison between apparent magnitudes i from APASS and SDSS surveys. The red dashed line is the identity line. A large number of stars with $12 < i_{\mathrm{APASS}} < 14$ present divergent SDSS magnitudes.

We implemented PARAM to compute the stellar properties taking into account the surface gravity provided by ASPCAP in the likelihood function (equation 2.3), instead of using seismic parameters ($\Delta\nu$ and $\nu_{\max}$) as was done with the APOKASC sample in Rodrigues et al. (2014). The surface gravity is a crucial parameter to estimate distances, since it depends on stellar radius and consequently on luminosity. Since the surface gravity (hence mass and radius) can be inferred in a direct and more precise way when $\nu_{\max}$ is combined with T_{eff} via the scaling relation (equation 1.3), asteroseismic uncertainties are one order of magnitude lower than the spectroscopic ones (~0.01 dex, Hekker et al., 2013), therefore higher uncertainties are expected for the stellar properties of the APOGEE stars.

The adopted set of isochrones is PARSEC v1.2s (Bressan et al., 2012), the same used for the analysis of APOKASC from the Padova-Trieste stellar evolution group.

In order to use our code, we selected stars with available T_{eff}, [M/H], and $\log g$ values, which returned 56042 stars, out of 4616 have at least SDSS g magnitude.

41

Figure 2.21 shows log *g versus T*_{eff} in the left panel and [M/H] *versus T*_{eff} in the right panel for these stars (black dots). The red dots are 49 stars that did not have a solution according to the first step of our method, because they are metal-poor stars located at older/metal-richer regions of the HR diagram, hence their spectroscopic parameters are not matching with any set of isochrones. To illustrate this, we also plotted isochrones with 1 and 10 Gyr (solid and dashed lines, respectively) and different metallicities, [M/H] = 0.0 and 0.5 (green and blue lines, respectively). Note that the red dots would be fitted with an older and metal-rich isochrone.
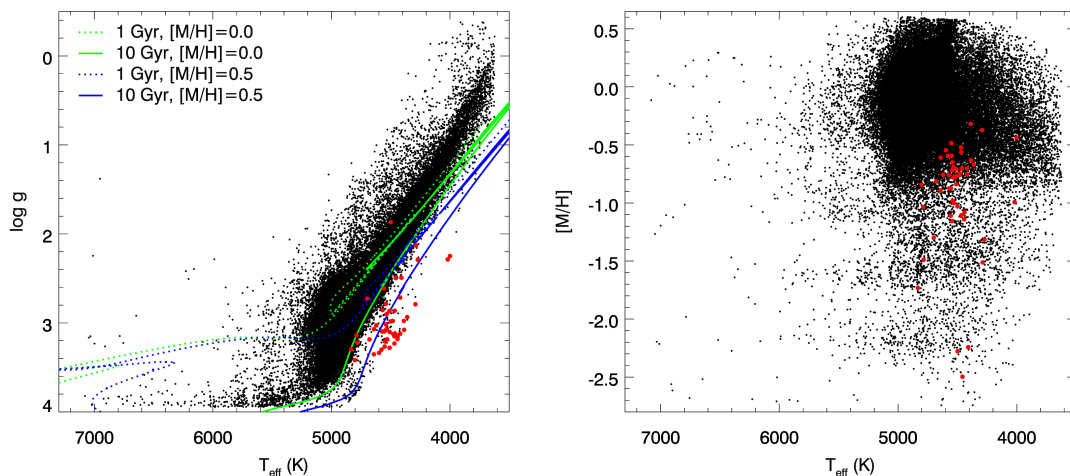
Figure 2.21: Left panel: log *g versus T*$_{\mathrm{eff}}$ for 61336 stars with available *T*$_{\mathrm{eff}}$, [M/H], and log *g* values (black dots). The solid and dashed lines are isochrones with 1 and 10 Gyr, respectively, and different metallicities, [M/H] = 0.0 and 0.5 (green and blue lines, respectively). Right panel: [M/H] *versus T*$_{\mathrm{eff}}$ for the same sample. The red dots are 49 stars that did not have a solution according to our method.

Only 47 stars did not have a distance/extinction solution according to step 2 of our method, probably because the photometric measurements are not accurate. Approximately 7 per cent of the stars have the extinction better fitted by negative values. As the ASPCAP log *g* is calibrated based only in the APOKASC RGB stars, the stellar properties derived for red clump stars may be biased, thus we decided to present results only for *non-RC stars*. We used the updated DR12 APOGEE-RC catalogue (Alam et al., 2015) to separate the RC stars (see the results for DR10 in Bovy et al., 2014, and also in Sect. 2.2.10). Figure 2.22 shows the log *g versus T*_{eff} diagram with the stars selected as RC ($\sim$ 22 per cent, red dots). Note that we did not adopt any priors on evolutionary stage in our code.

The distributions of uncertainties for extinctions and distances are presented in Figure 2.23. The average (absolute and relative) uncertainties are $\langle \sigma A_V \rangle =$
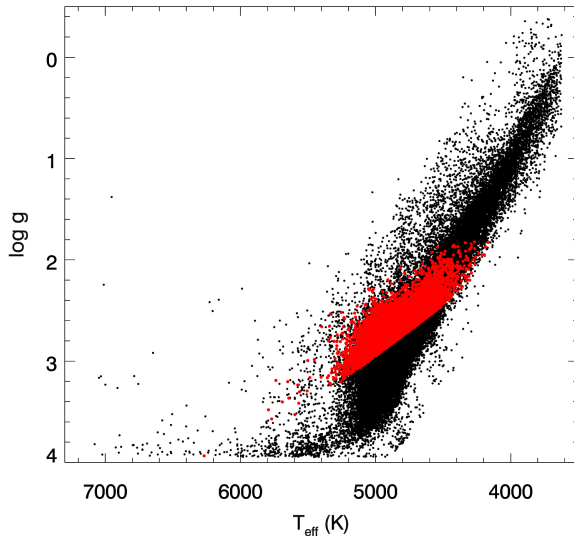
Figure 2.22: $\log g$ *versus* $T_{\rm eff}$ diagram showing the RC stars (red dots) selected by Bovy et al. (2014) – $\sim$ 22 per cent of our sample.

0.212 mag and $\langle \sigma d/d \rangle = 0.062$. These average uncertainties increase when the number of available photometric measurements decrease (see Table 2.1), thus the estimated values for stars with number of observed passbands < 6 should be used with caution, although most of the stars ($\sim$ 70 per cent) have at least 9 measurements of apparent magnitudes.
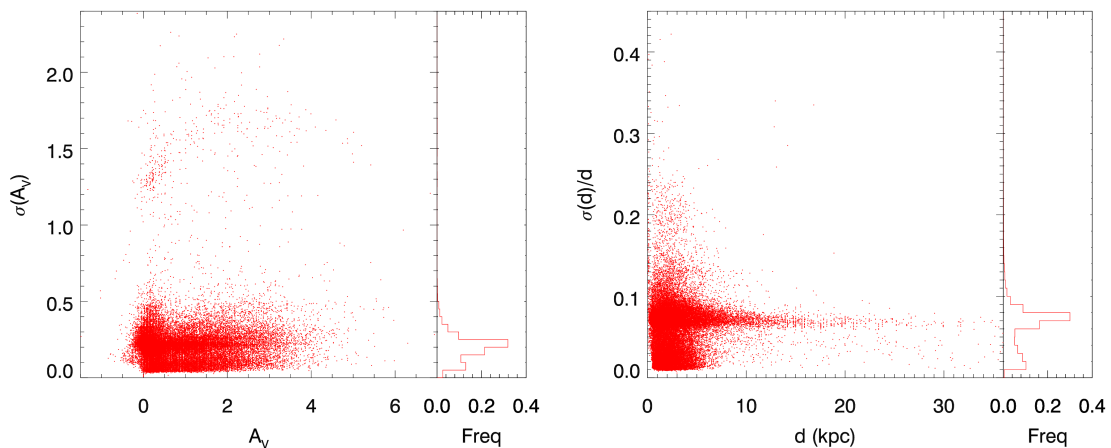
Figure 2.23: Distribution of relative and absolute uncertainties for extinctions (left panel) and distances (right panel) for APOGEE survey, respectively. The right sub-panels show histograms of these uncertainties distributions.

Table 2.1: Average uncertainties for extinctions and distances according to the number of passbands used for APOGEE survey.

Number of passbands	$\langle\sigma A_V\rangle$ mag	$\langle\sigma d/d\rangle$ %	Number of stars
2	1.779	0.371	21
3	1.410	0.157	21
4	1.154	0.135	36
5	1.215	0.102	532
6	0.361	0.066	1390
7	0.259	0.064	4696
8	0.208	0.062	6790
9	0.179	0.061	26649
>9	0.178	0.061	30254

2.3.1 Comparison with APOKASC

In order to check the distances and extinctions estimated for APOGEE stars, we compared them with the ones from APOKASC catalogue. There are ~ 3300 RGB stars with seismic parameters ($\Delta\nu$ and ν_{max}) derived according to Mosser & Appourchaux (2009) and spectroscopic parameters (T_{eff} and [Fe/H]) from APOGEE DR12 (Alam et al., 2015). We adopted the same photometry as for APOGEE stars and derived stellar parameters using as input observational data in our code PARAM: T_{eff}, [Fe/H], $\Delta\nu$, and ν_{max}.

Figure 2.24 shows the comparison between extinctions and distances using seismic parameters (APOKASC) and only spectroscopic parameters (APOGEE). The average difference between extinctions is (0.070 ± 0.002) mag with a dispersion of 0.115 mag. The solid line is the linear fit:

$$A_{\mathrm{V,APOGEE}} = (0.105 \pm 0.003) + (0.872 \pm 0.010)A_{\mathrm{V,APOKASC}}.$$

While for distances, the agreement is very good, the relative difference is $\langle(d_{\mathrm{APOGEE}} - d_{\mathrm{APOKASC}})/d_{\mathrm{APOKASC}}\rangle = (0.013 \pm 0.001)$ with a dispersion of 0.197.

2.3.2 APOGEE extinctions

Figure 2.25 shows our extinction map. We display also in Figures 2.26 and 2.27 the extinction maps of Schlegel, Finkbeiner & Davis (1998, SFD), Schlafly et al. (2014), Majewski, Zasowski & Nidever (2011, RJCE) and Green et al. (2015). A short description about extinctions from SFD and RJCE can be seen in Sect. 2.2.8.
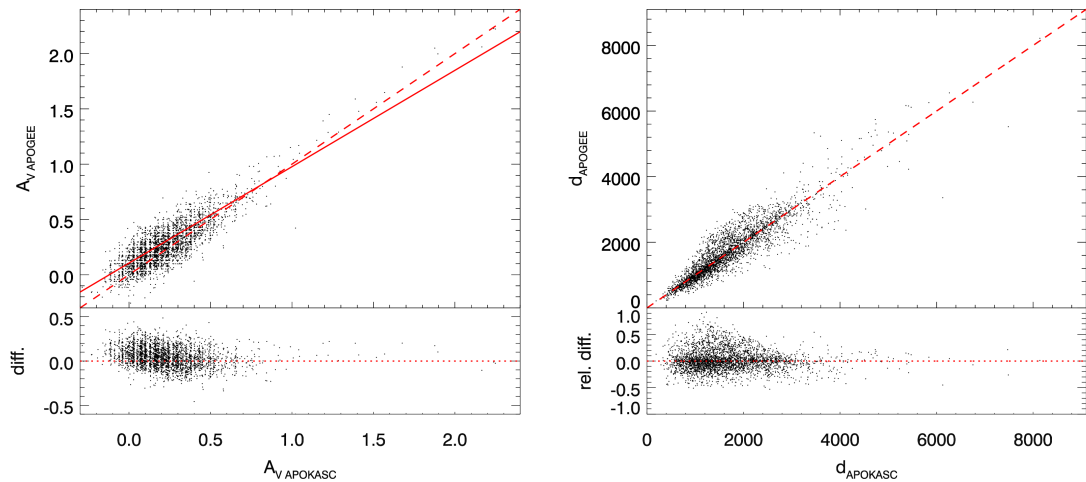
Figure 2.24: Comparison between extinctions (left panel) and distances (right) estimated using seismic parameters and only spectroscopic parameters for APOGEE stars in the *Kepler* field. Sub-panels show the absolute and relative differences.
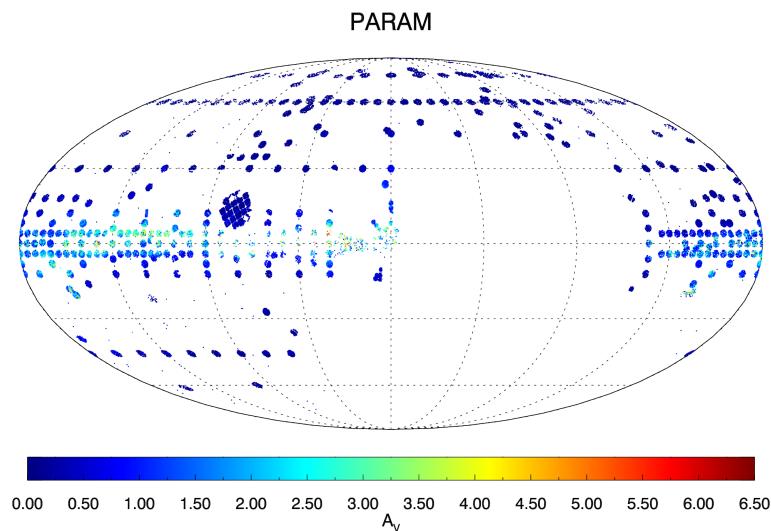
Figure 2.25: Our extinction map for APOGEE survey.

Schlafly et al. (2014) provide a map of the cumulative reddening out to 4.5 kpc using the Pan-STARRS1 (PS1) survey (Kaiser et al., 2010; Tonry et al., 2012), which observed the entire Northern sky, with declination greater than $-30°$ in five filters ($grizy_{P1}$, 400–1000 nm). The method is explained in detail in Green et al. (2014). The photometry of each star is modelled as function of distance, reddening,
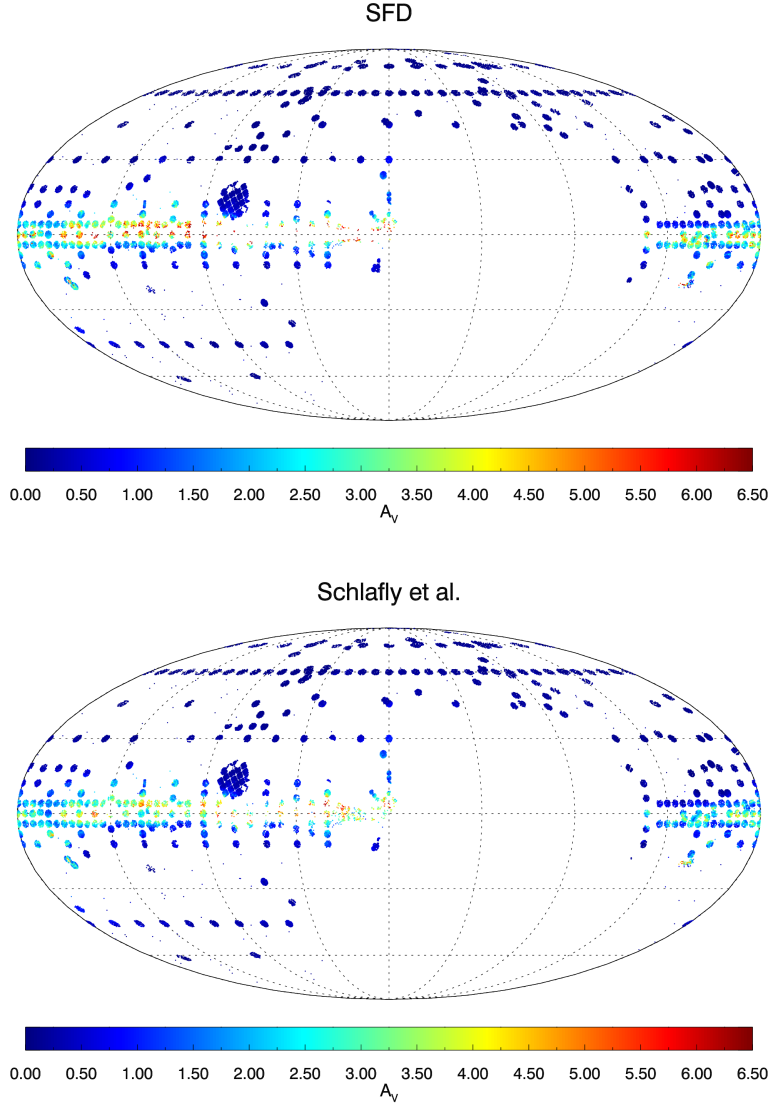
Figure 2.26: SFD and Schlafly et al. (2014) extinction maps for APOGEE survey.

and stellar type. An empirical set of models for the PS1 colors is adopted and related with absolute magnitudes and metallicity as given in Ivezić et al. (2008). The authors take into account priors based on the distribution of stars and their types using the Galactic model of Jurić et al. (2008) and the metallicity distribution of Ivezić et al. (2008). The luminosity function is described using the PARSEC stellar evolution models (Bressan et al., 2012) adopting the initial mass function of Chabrier (2001). Finally, the joint probability distribution function that describes

46
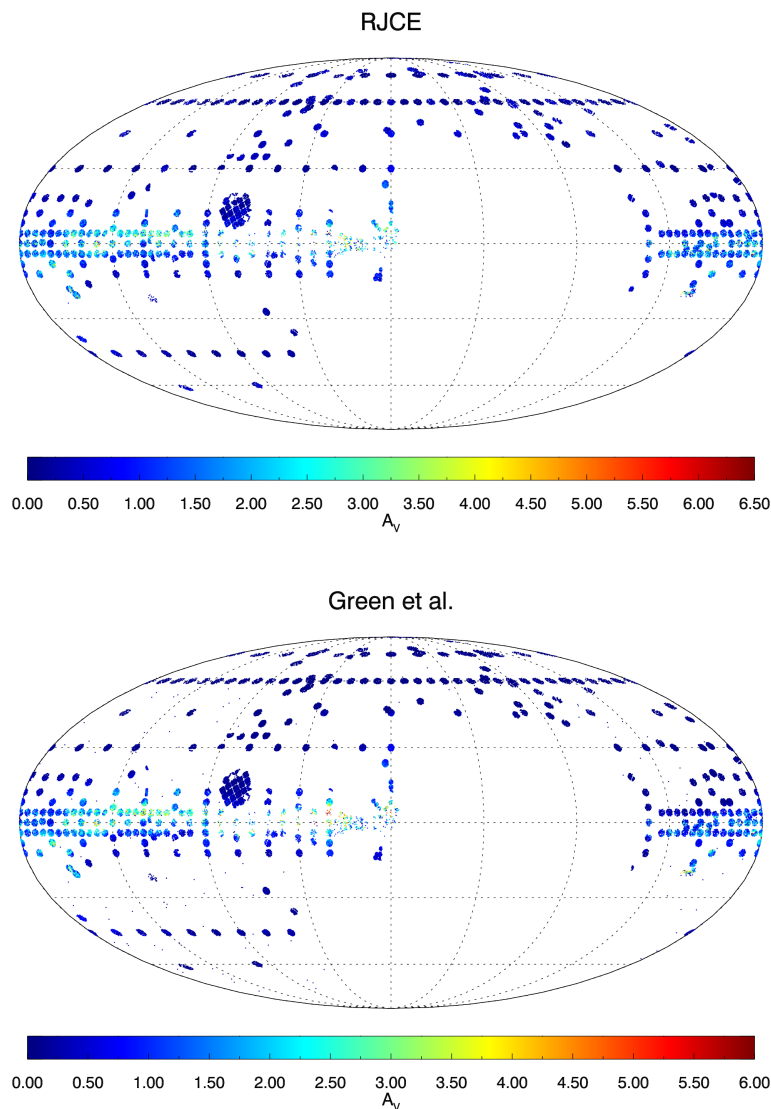
RJCE

Green et al.

Figure 2.27: RJCE (top panel) and Green et al. (2015) (bottom) extinction maps for APOGEE survey.

the range of possible reddenings and distances to each star is computed. In order to draw the map, the sky is split into individual line of sight with an area of $7' \times 7'$, so that the reddening profile as a function of distance is computed using all the stars along each line of sight. The reddening is then integrated to distance equal 4.5 kpc.

Green et al. (2015) provide a 3D map of the dust reddening, applying the same method explained in Green et al. (2014) with some modifications: (i) the 2MASS

photometry was added to approximately one quarter of the sample that has PS1 magnitudes; (ii) in this case, the dust density can also vary with the angle within a given pixel, instead than only be a function of the distance, i.e., each star can have slightly different reddening from the overall reddening profile in that pixel; (iii) some parameters that describe the distribution of the stars were changed, as the disk scale lengths and heights and the density of the halo. As the map is 3D, they also estimated the minimum and maximum distances in which the extinction map is reliable in each pixel, according to the number of stars. We then computed the extinction for each star of our sample by interpolating the distance modulus resulting from PARAM in the line of sight $E(B-V)$ *versus* distance modulus curve given by Green et al. (2015)[4]. The bottom map of the Figure 2.27 only shows stars in which the distance is in the range of the reliable extinction map.

Figure 2.28 presents the comparison between our extinction and SFD, Schlafly et al. (2014), RJCE, and Green et al. (2015). The blue dots are the weighted mean extinction in each of the 412 APOGEE fields, including the *Kepler* fields. Dashed red lines represent the identity line. Solid lines are the following linear fits:

$$A_V = (0.190 \pm 0.001) + (0.514 \pm 0.001)A_V^{\mathrm{SFD}}$$
$$A_V = (0.098 \pm 0.001) + (0.678 \pm 0.001)A_V^{\mathrm{Schlafly}}$$
$$A_V = (0.111 \pm 0.001) + (1.034 \pm 0.001)A_V^{\mathrm{Green}}$$
$$A_V = (0.016 \pm 0.001) + (0.972 \pm 0.001)A_V^{\mathrm{RJCE}}. \tag{2.12}$$

The average difference and dispersion are given in table 2.2. It is important to note:

- It is expected that SFD and Schlafly et al. extinctions are greater than ours, because they are computed at infinite and 4.5 kpc, respectively. Following this, the SFD extinctions show a larger dispersion than Schlafly et al..

- Our extinctions are slightly greater than Green et al. ones. In any case, it is remarkable the good agreement between both and clear that it is important to take into account the distance in each line of sight.

- Our extinctions are also in very good agreement with RJCE, with a dispersion slightly greater than of Green et al..

2.3.3 APOGEE clusters

Several stars belonging to 20 (open and globular) clusters are used to calibrate ASPCAP results (Mészáros et al., 2013; Holtzman et al., 2015). From this sample,

---

[4]http://argonaut.skymaps.info/
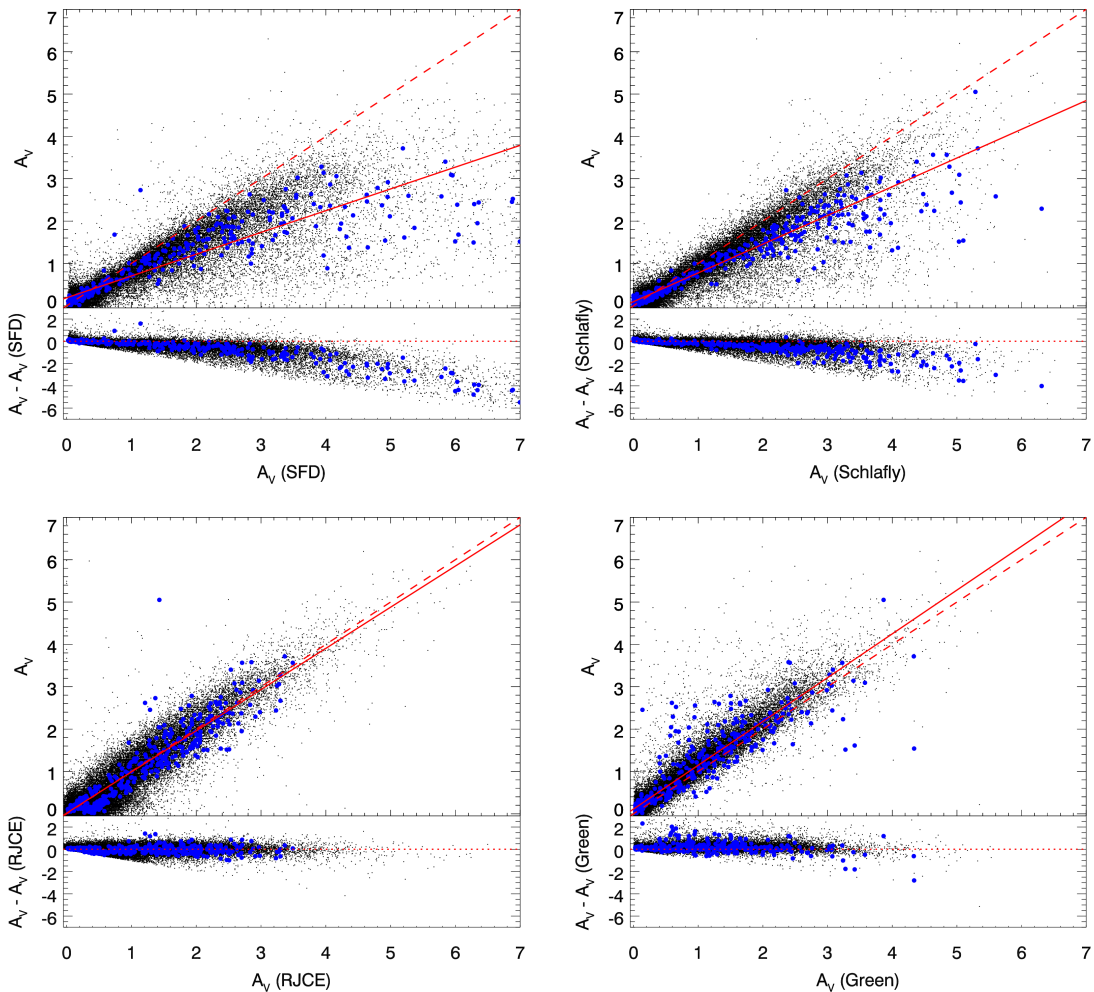
Figure 2.28: Comparison between our extinctions and SFD (top left panel), Schlafly et al. (2014) (top right), RJCE (bottom left), and Green et al. (2015) (bottom right). The blue dots are the weighted mean extinction in each of the 412 APOGEE fields, including the *Kepler* fields. Dashed red lines represent the identity line. Solid lines are a linear fitting.

214 stars belonging to 13 clusters have distances estimated by PARAM. Figure 2.29 shows the comparison between our individual distances (d_{PARAM}) and the cluster distances (d_{cluster}; black dots) for clusters with at least 3 stars. We adopted cluster distances from WEBDA[5] cluster database and Harris (1996) for open and globular clusters, respectively. We derived the cluster distances by averaging the distances of

---

[5] : http://www.univie.ac.at/webda/

Table 2.2: Average differences and dispersions between our extinctions and SFD, Schlafly et al. (2014), RJCE, and Green et al. (2015) for the APOGEE survey.

	$A_V - A_V(X)$	dispersion
SFD	-0.363	0.666
Schlafly et al.	-0.235	0.456
Green et al.	0.133	0.301
RJCE	-0.007	0.350

the individual stars (red filled circles; error bars represent the standard deviation). The clusters are located between 0.8 and 20 kpc (see Table 2.3). The average difference is $\langle (d_{\mathrm{PARAM}}^{\mathrm{cluster}} - d_{\mathrm{cluster}})/d_{\mathrm{cluster}} \rangle = -0.15 \pm 0.03$ with a dispersion of 17 per cent.

The cluster members were selected according to radial velocity or proper motion with a probability > 50 per cent, what indicates that some stars may not actually be members. This may explain the large scater in distances inside some clusters. Other causes may be binary members and interaction between stars that could result in a non-standard evolution.
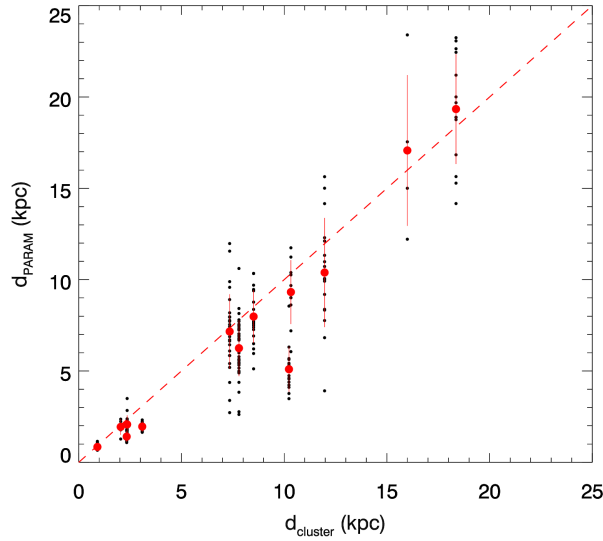
Figure 2.29: Comparison of our individual distances (black dots) and the cluster distances from the literature. Red filled circles and error bars display our mean distances and standard deviations for each cluster. The red dashed line is the identity line.

Table 2.3: Cluster distances for some star clusters observed by APOGEE survey.

Name	d_{cluster} kpc	$d_{\mathrm{PARAM}}^{\mathrm{cluster}}$ kpc	Number of stars
M 3	10.33	9.32	10
M 5	7.80	6.25	40
M 13	7.35	7.16	29
M 15	11.97	10.39	17
M 53	18.37	19.34	14
M 67	0.91	0.84	22
M 92	8.51	7.98	21
M 107	10.23	5.10	15
NGC 188	2.04	1.94	5
NGC 2420	3.09	1.96	8
NGC 5460	16.00	17.07	5
NGC 6819	2.36	2.07	20
NGC 7789	2.33	1.41	8

2.4 Distances and extinctions for APOKASC-2 using data from APOGEE DR13

The entire set of APOKASC-2 data was not published together with the APOGEE DR13 data (SDSS Collaboration et al., 2016), however it will be released soon in a paper describing all the details of the catologue (Pinsonneault et al., in preparation). As we are external collaborators, we have access to the data. Approximately ~ 11880 stars were observed by APOGEE and ~ 90 per cent have basic stellar parameters derived by ASPCAP. Figure 2.30 shows these stars in Galactic coordinates relative to the *Kepler* field.

In order to derive the global seismic parameters ($\Delta\nu$ and ν_{max}), four seismic pipelines were used, then the entire set went through different grid-based models to estimate stellar properties, including our code PARAM. The analysis of this large amount of data will be done in Elsworth et al. (in preparation). Here we are going to focus in only one seismic pipeline, called COR (Mosser & Appourchaux, 2009), combined with the last data release from ASPCAP (DR13). The APOGEE raw data remain the same as DR12, but with changes in the ASPCAP processing and analysis, which improved and enhanced the stellar parameters and abundances (SDSS Collaboration et al., 2016). No calibration was applied to the T_{eff}, because they have a good agreement with photometric T_{eff} for most of the stars that have near solar-metallicity. However there are a significant offset up to 200-300 K for stars with lower metallicity. As the surface gravities are calibrated based on asteroseismology
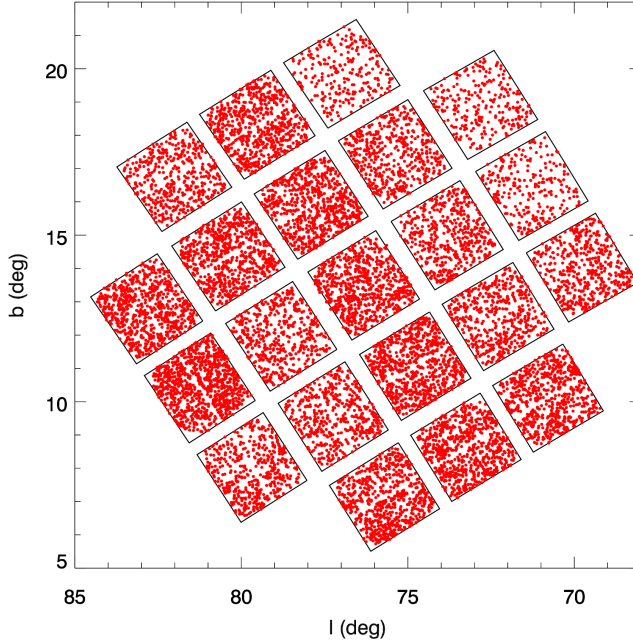
Figure 2.30: Entire set of the APOKASC stars (red dots) observed by APOGEE in Galactic coordinates relative to the *Kepler* field (squares).

gravities, they also present an offset regarding low metallicity stars. This offset will be discussed in details in Holtzman et al. (in preparation). In the time we ran the entire set in our code PARAM, this offset was not corrected. This will be done during the next months and we will recompute the stellar properties in order to released them with the APOKASC catalogue.

We analysed $\sim$ 5800 stars with seismic and spectroscopic parameters available, out of 5774 have stellar properties, distances, and extinctions derived with PARAM. The distribution of the relative and absolute uncertainties are presented in Figure 2.31. The median uncertainties are $\sigma(M)/M = 0.057$, $\sigma(R)/R = 0.022$, $\sigma(\log g) = 0.008$ dex, $\sigma(A_V) = 0.057$ mag, and $\sigma(d)/d = 0.013$. These values are slightly smaller than the first analysis of APOKASC.

Figure 2.32 compares our extinction maps for the entire *Kepler* field with those derived from SFD, KIC, and Green et al. (2015). Figure 2.33 shows the comparison between our extinctions $A_V(\text{COR})$ with these three maps; the red solid lines are the
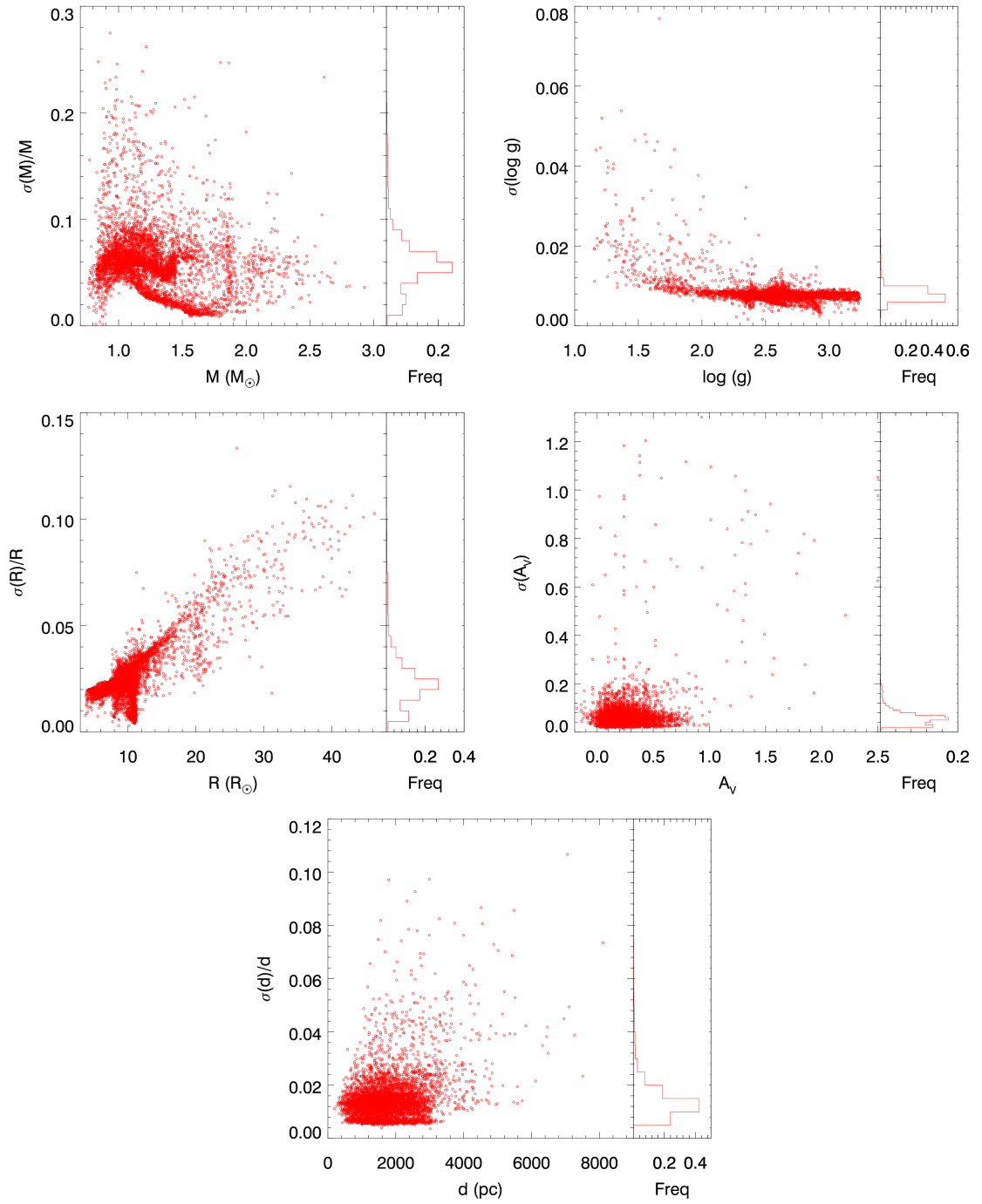
Figure 2.31: Distribution of relative and absolute uncertainties for mass, radius, $\log g$, A_V, and distances for stars in APOKASC-2 catalogue.
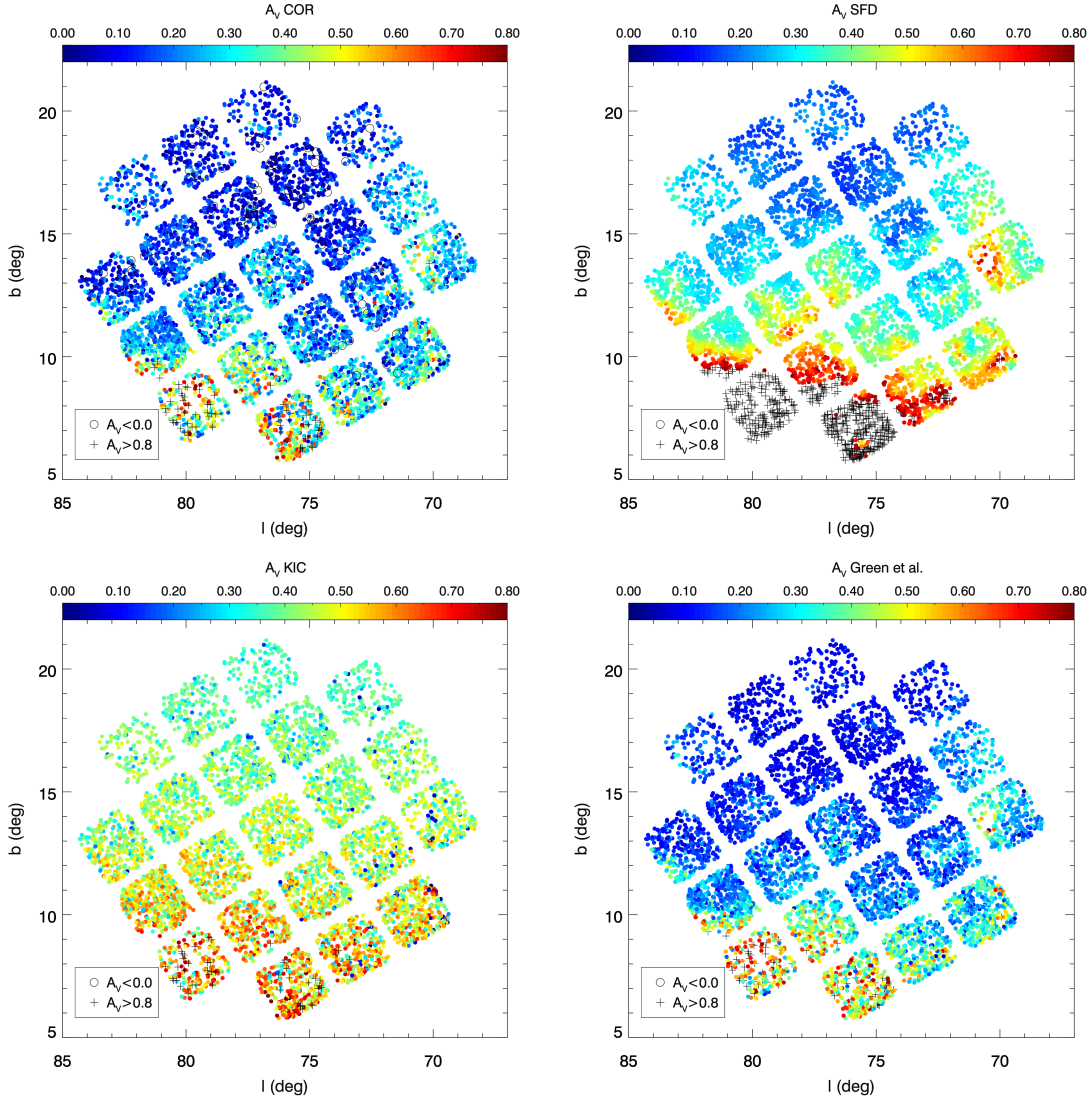
Figure 2.32: Our extinction maps as compared to SFD, KIC, and Green et al. (2015). Extinctions greater than 0.8 mag are represented by a plus symbol.

following linear fit:

$$A_V = (0.163 \pm 0.001) + (1.077 \pm 0.001)A_V^{\text{SFD}}$$
$$A_V = (0.349 \pm 0.001) + (0.455 \pm 0.001)A_V^{\text{KIC}}$$
$$A_V = (0.023 \pm 0.001) + (0.904 \pm 0.001)A_V^{\text{Green}}. \tag{2.13}$$

As already discussed in Sec. 2.2.8, it is expected that the SFD A_V are much larger than ours, as they are extinctions at the infinity. The average difference is 0.21 mag

with a dispersion of 0.29 mag. While KIC values have a smaller dispersion, their values do not follow the one to one relation and are larger than ours for lower extinctions. The KIC relation presented in equation 2.13 is important in order to estimate extinctions for stars in the *Kepler* field that were not yet observed by APOGEE, as the KIC extinctions are based in a simple geometrical model for the distribution of dust (Brown et al., 2011) and do not seem to reproduce well the A_V in these latitudes. The Green et al. values were computed as explained in Sec. 2.3.2, they are in good agreement with ours values and present a dispersion of only 0.11 mag.
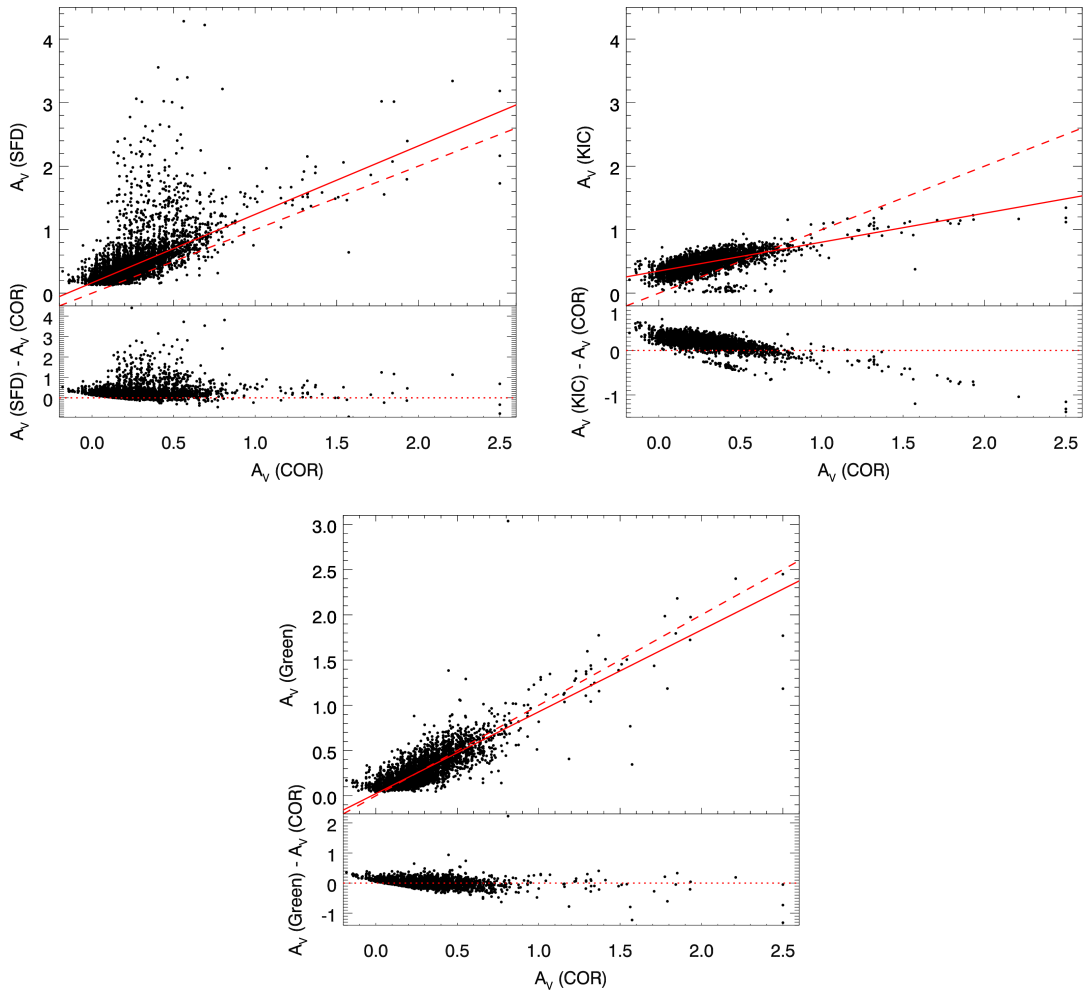
Figure 2.33: Comparison between our extinctions and SFD, KIC, and Green et al. (2015). Dashed red lines represent the identity line. Solid lines are a linear fitting.

Chapter 3

Going beyond the use of scaling relations

3.1 Introduction

With the detection of solar-like oscillation in thousands of red giant stars, *Kepler* and CoRoT missions have opened the way to the derivation of basic stellar properties such as mass and age even for single stars located at distances of several kiloparsecs. As described in Sec. 1.2.2, this derivation is based on the two more easily-measured asteroseismic properties: $\Delta\nu$ and ν_{max}. These parameters give rise to the so-called scaling relations:

$$\begin{aligned} \Delta\nu &\propto \overline{\rho}^{1/2} \propto M^{1/2}/R^{3/2} \\ \nu_{\mathrm{max}} &\propto g T_{\mathrm{eff}}^{-1/2} \propto (M/R^2) T_{\mathrm{eff}}^{-1/2} \quad . \end{aligned} \tag{3.1}$$

It is straightforward to invert these relations and derive masses M and radii R as a function of ν_{max}, $\Delta\nu$, and T_{eff} (as explained in Chapter 2). The latter has to be estimated in an independent way, for instance via the analysis of high-resolution spectroscopy. M and R can then be determined either (1) in a model-independent way by the "direct method", which consists in simply applying the scaling relations with respect to the solar values, or (2) via some statistical method that takes into account stellar theory predictions and other kinds of prior information. In the latter case, the methods are usually referred to as either "grid-based" or "Bayesian" methods.

Determining the radii and masses of giant stars brings consequences of great astrophysical interest: the radius added to a set of apparent magnitudes can be used to estimate the stellar distance and the foreground extinction. The mass of a giant is generally very close to the turn-off mass of its parent population, and hence closely related with its age; the latter is otherwise very difficult to estimate for

isolated field stars. In addition, the surface gravities of asteroseismic targets can be determined with an accuracy generally much better than allowed by spectroscopy.

Although these ideas are now widely-recognized and largely used in the analyses of CoRoT and *Kepler* samples, there are also several indications that asteroseismology can provide even better estimates of masses and ages of red giants, than allowed by the scaling relations above. First, there are significant evidences of corrections of a few percent being necessary (see White et al., 2011; Miglio, 2012; Miglio et al., 2013; Brogaard et al., 2016; Miglio et al., 2016; Guggenberger et al., 2016; Sharma et al., 2016; Handberg et al., submitted) in the $\Delta\nu$ scaling relation. Although such corrections are expected to have little impact on the stellar radii (and hence on the distances), they are expected to reduce the errors in the derived stellar masses, hence on the derived ages for giants. Second, there are other asteroseismic parameters as well – like for instance the period spacing of mixed modes, ΔP (Beck et al., 2011; Mosser et al., 2014) – that can be used to estimate stellar parameters, although not via so easy-to-use scaling relations as those above-mentioned.

In the third part of this thesis, we go beyond the use of simple scaling relations in the estimation of stellar properties via Bayesian methods, first by replacing the $\Delta\nu$ scaling relation by using frequencies actually computed along the evolutionary tracks, and second by including the period spacing ΔP in the method. We study how the precision and accuracy of the inferred stellar properties improve with respect to those derived from scaling relations, and how they depend on the set of available constraints. The set of additional parameters to be explored includes also the intrinsic stellar luminosity, which will be soon determined for a huge number of stars in the Milky Way thanks to the upcoming Gaia parallaxes (Lindegren et al., 2016, and references therein). The results are tested both on synthetic data and on the star cluster NGC 6819, for which *Kepler* has provided high-quality oscillation spectra for about 50 giants (Basu et al., 2011; Stello et al., 2011; Corsaro et al., 2012; Handberg et al., submitted).

The structure of this Chapter is as follows. Sec. 3.2 presents the grids of stellar models used in this work, describes how the $\Delta\nu$ and ΔP are computed along the evolutionary tracks, which was done in collaboration with Andrea Miglio, Diego Bossini, and Josefina Moltabán; and how the same parameters are accurately interpolated in order to generate isochrones. Sec. 3.3 employs the isochrone sets incorporating the new asteroseismic properties to evaluate stellar parameters by means of a Bayesian approach. The method is tested both on synthetic data and on real data for the NGC 6819 cluster.

3.2 Models

3.2.1 Physical inputs

The grid of models was computed using the MESA code (Paxton et al., 2011, 2013). We computed 21 masses in a range between $M = 0.6 - 2.5 M_\odot$, in combination with 7 different metallicities ranging from [Fe/H]$= -1.00$ to 0.50 (Table 3.1)[1]. The following points summarize the relevant physical inputs used:

- The tracks were computed starting from the pre-main sequence (PMS) up to the first thermal pulse of the asymptotic giant branch (TP-AGB).

- We adopt Grevesse & Noels (1993) heavy elements partition.

- The OPAL equation of state (Rogers & Nayfonov, 2002) and OPAL opacities (Iglesias & Rogers, 1996) were used, augmented by low-temperature opacities from Ferguson et al. (2005). C-O enhanced opacity tables were considered during the helium-core burning (HeCB) phase.

- A custom table of nuclear reaction rates was used (NACRE, Angulo et al., 1999).

- The atmosphere is taken according to Krishna Swamy (1966) model.

- Convection was treated according to mixing-length theory, using the solar-calibrated parameter ($\alpha_{\mathrm{MLT}} = 1.9657$).

- Overshooting was applied during the core-convective burning phases in accordance with Maeder (1975) step function scheme. We use overshooting with a parameter of $\alpha_{\mathrm{ovH}} = 0.2 H_p$ during the main sequence, while we consider $\alpha_{\mathrm{ovHe}} = 0.5 H_p$ penetrative convection in the HeCB phase (following the definitions in Zahn 1991 and the result in Bossini et al. 2015).

- Element diffusion, mass loss, and effects of rotational mixing were not taken in account.

- Metallicities [Fe/H] were converted in mass fractions of heavy elements Z by the approximate formula $Z = Z_\odot \cdot 10^{[\mathrm{Fe/H}]}$, where $Z_\odot = 0.01756$, coming from

---

[1]According to the simulations by Girardi et al. (2015), less than one per cent of the giants in the Kepler fields are expected to have masses larger than 2.5 $M_\odot$.

the solar calibration. The initial helium mass fraction Y depends on Z and was set using a linear helium enrichment expression

$$Y = Y_p + \frac{\Delta Y}{\Delta Z} Z \qquad (3.2)$$

with the primordial helium abundance $Y_p = 0.2485$ and the slope $\Delta Y/\Delta Z = (Y_\odot - Y_p)/Z_\odot = 1.007$. Table 3.1 shows the relationship between [Fe/H], Z, and Y for the tracks computed.

Table 3.1: Initial masses and chemical composition of the computed tracks.

Mass ($M_\odot$)		
0.60, 0.80, 1.00, 1.10, 1.20, 1.30, 1.40, 1.50, 1.55, 1.60,		
1.65, 1.70, 1.75, 1.80, 2.00, 2.15, 2.30, 2.35, 2.40, 2.45, 2.50		
[Fe/H]	Z	Y
-1.00	0.00176	0.25027
-0.75	0.00312	0.25164
-0.50	0.00555	0.25409
-0.25	0.00987	0.25844
0.00	0.01756	0.26618
0.25	0.03123	0.27994
0.50	0.05553	0.30441

3.2.2 Structure of the grid

To build the tracks actually used in our Bayesian-estimation code, we select from the original tracks computed with MESA about two hundred structures well-distributed in the HR diagram and representing all evolutionary stages. From these models we extract global quantities, such as the age, the photospheric luminosity, the effective temperature (T_{eff}), the period spacing of gravity modes (ΔP, see Section 3.2.4). In addition, each structure is also used to compute individual radial mode frequencies with GYRE (Townsend & Teitler, 2013) in order to calculate large separations ($\Delta \nu$), as described in Sec. 3.2.3.

3.2.3 Average large frequency separation

Determination of the large frequency separation

In a first approximation, the large separation $\Delta \nu$ can be estimated in the models by the equation 3.1. However, this estimation can be inaccurate, since is affected by a

systematic effects which depend e.g. on the evolutionary phase and, more generally, on how the sound speed behaves in the stellar interior. To go beyond the seismic scaling relations, we calculate individual radial-mode frequencies for each of the models in the grid. Based of the frequencies we compute an average large frequency separation $\langle \Delta\nu \rangle$. We adopt a definition of $\langle \Delta\nu \rangle$ as close as possible to the observational counterpart. The average $\Delta\nu$ as measured in the observations depends on the number of frequencies identified around ν_{max} and on their uncertainties. Therefore, with the aim of a self-consistent comparison between data and models, any $\langle \Delta\nu \rangle$ calculated from stellar oscillation codes must take in account the restrictions given by the observations. Handberg et al. (submitted) estimated the quantity $\Delta\nu_{\text{fit}}$ for the stars in the *Kepler*'s cluster NGC 6819. In that paper, $\Delta\nu_{\text{fit}}$ is estimated by a simple linear fit of the individual frequencies (weighted on their errors) as function of the radial order. The value of the slope resulting from the fitting line gives the estimated $\Delta\nu$.

Surface effects

It is well known that current stellar models suffer from an inaccurate description of near-surface layers leading to a mismatch between theoretically predicted and observed oscillation frequencies. These so-called surface effects have a sizable impact also on the large frequency separation, and on its average value. When using model-predicted $\Delta\nu$ it is therefore necessary to correct for such effects. As usually done, a first attempt at correcting is to use the Sun as a reference, hence by normalising the $\langle \Delta\nu \rangle$ of a solar-calibrated model with the observed one.

In our solar model, α_{MLT} and $X_\odot$ are calibrated to reproduce, at the solar age $t_\odot = 4.57$ Gyr, the observed luminosity $L_\odot = 3.8418 \cdot 10^{33}$ erg s^{-1}, the photospheric radius $R_\odot = 6.9598 \cdot 10^{10}$ cm (Bahcall et al., 2005), and the present-day ratio of heavy elements to hydrogen in the photosphere ($Z/X = 0.02452$, Grevesse & Noels 1993). We used the same input physics as described in Sec. 3.2. We find that the predicted average large separation, $\langle \Delta\nu_{\odot,\text{mod}} \rangle = 136.1 \ \mu$Hz (defined cf. Sec. 3.2.3), is 0.8 per cent larger than the observed one ($\langle \Delta\nu_{\odot,\text{obs}} \rangle = 135.0 \ \mu$Hz). We then follow the approach by White et al. (2011) and adopt as a solar reference value that of our calibrated solar model ($\langle \Delta\nu \rangle_\odot = \langle \Delta\nu \rangle_{\text{mod},\odot} = 136.1 \mu$Hz).

This is an approximation which should be kept in mind, and an increased accuracy when using $\langle \Delta\nu \rangle$ can only be achieved by both improving our theoretical understanding of surface effects in stars other than the Sun (e.g. see Sonoi et al., 2015; Ball et al., 2016), and by trying to mitigate surface effects when comparing models and observations. In this respect a way forward would be to determine the star's mean density by using the full set of observed acoustic modes, not just their average frequency spacing. This approach was carried out in at least two RGB stars (Huber et al., 2013; Lillo-Box et al., 2014), and led to determination of the stellar

mean density which is $\sim 5 - 6$ per cent higher than derived from assuming scaling relations, and with a much improved precision of ~ 1.4 per cent. Furthermore, the impact of surface effects on the inferred mean density is mitigated when determining the mean density using individual mode frequencies rather than using the average large separation (e.g., see Chaplin & Miglio, 2013). This approach is however not yet feasible for populations studies, mostly because individual mode frequencies are not available yet for such large ensembles, but it is a path worth pursuing to improve both precision and accuracy of estimates of the stellar mean density.

$\Delta\nu$: deviations from simple scaling

Small-scale deviations from the $\langle\Delta\nu\rangle$ scaling relation have been investigated in several papers. This is usually done by comparing how well model predicted $\langle\Delta\nu\rangle$ scales with $\bar{\rho}^{1/2}$, taking the Sun as a reference point (see White et al., 2011; Miglio, 2012; Miglio et al., 2013; Brogaard et al., 2016; Miglio et al., 2016; Guggenberger et al., 2016; Sharma et al., 2016; Handberg et al., submitted).

Such deviations may be expected primarily for two reasons. First, stars in general are not homologous to the Sun, hence the sound speed in their interior (hence the total acoustic travel time) does not simply scale with mass and radius only. Second, the oscillation modes detected in stars do not adhere to the asymptotic approximation to the same degree as in the Sun (see e.g. Belkacem et al., 2013, for a more detailed explanation).

The combination of these two factors is what eventually determines a deviation from the scaling relation itself. Cases where a small correction is expected are likely the result of a fortuitous cancellation of the two effects (e.g. in RC stars).

We would like to stress that beyond global trends e.g. with global properties, such corrections are also expected to be evolutionary-state and mass dependent, as discussed e.g. in Miglio (2012), Miglio et al. (2013), and Christensen-Dalsgaard et al. (2014). The middle panel of figure 3.1 shows the ratio between the large separation from scaling relation ($\Delta\nu_{\text{scal.}}$) and $\langle\Delta\nu\rangle$ (calculated as described in Sec. 3.2.3) as a function of ν_{max} for a large number of tracks in the grid.

3.2.4 Period spacing

It has been shown by Mosser et al. (2012) that is possible to infer the asymptotic period spacing of a star, by fitting a simple pattern on their oscillation spectra. This is particularly relevant for those stars that present a rich forest of dipole modes ($l = 1$), like, for instance, the red giants. The asymptotic theory of stellar oscillation tells us that the g-modes are related by an asymptotic relation where their periods are equally spaced by ΔP_l. The relation states that the asymptotic period spacing is proportional to the inverse of the integral of the Brunt-Väisälä frequency N inside

the trapping cavity:

$$\Delta P_l = \frac{2\pi^2}{\sqrt{l(l+1)}} \left(\int_{r_1}^{r_2} \frac{N}{r} \mathrm{d}r \right)^{-1}, \tag{3.3}$$

where r_1 and r_2 are the coordinates in radius of turning points that limit the cavity. It is easy to see that its value depends, among other things, on the size and the position of the internal cavity, fact that will become particularly relevant in the helium-core-burning phase, giving the uncertainties on the core convection (Montalbán et al., 2013; Bossini et al., 2015). On the RGB the period spacing is an excellent tool to set constrains on other stellar quantities, like radius, and luminosity (see for instance Lagarde et al. 2016 and Davies & Miglio 2016). Moreover the period spacing gives an easy and immediate discrimination between stars in helium-core-burning and in RGB phases, since the former have a ΔP systematically larger of about $\sim 200 - 300$ s than the latter, while after the early-AGB phase it decreases to similar or smaller values.

3.2.5   Interpolating the $\Delta\nu$ deviations to make isochrones

The $\Delta\nu$ computed along the tracks appropriately sample stars in the most relevant evolutionary stages, and over the interval of mass and metallicity to be considered in this work. However, in order to be useful in Bayesian codes, a further step is necessary: such calculations need to be interpolated for *any* intermediate value of evolutionary stage, mass, and metallicity. This would allow us to derive detailed isochrones, that can enter easily in any estimation code which involves age as a parameter. Needless to say, such isochrones may find many other applications.

The computational framework to perform such interpolations is already present in our isochrone-making routines, which are described elsewhere (see Marigo et al., 2017). In short, the following steps are performed: our code reads the evolutionary tracks of all available initial masses and metallicities; these tracks contain age (τ), luminosity (L), T_{eff}, $\Delta\nu$, and ΔP from the ZAMS until TP-AGB. These quantities are interpolated between the tracks, for any intermediate value of initial mass and metallicity, by performing linear interpolations between pairs of "equivalent evolutionary points", i.e., points in neighbouring tracks which share similar evolutionary properties. An isochrone is then built by simply selecting a set of interpolated points for the same age and metallicity. In the case of $\Delta\nu$, the interpolation is done in the quantity $\Delta\nu/\Delta\nu_{\mathrm{SR}}$, where $\Delta\nu_{\mathrm{SR}}$ is the value defined by the scaling relation in equation 3.1. In fact, $\Delta\nu/\Delta\nu_{\mathrm{SR}}$ varies along the tracks in a much smoother way, and has a much more limited range of values than the $\Delta\nu$ itself; therefore the multiple interpolations of its value among the tracks also produce well-behaved results. Of course, in the end the interpolated values of $\Delta\nu/\Delta\nu_{\mathrm{SR}}$ are converted into $\Delta\nu$, for every point in the generated isochrones.
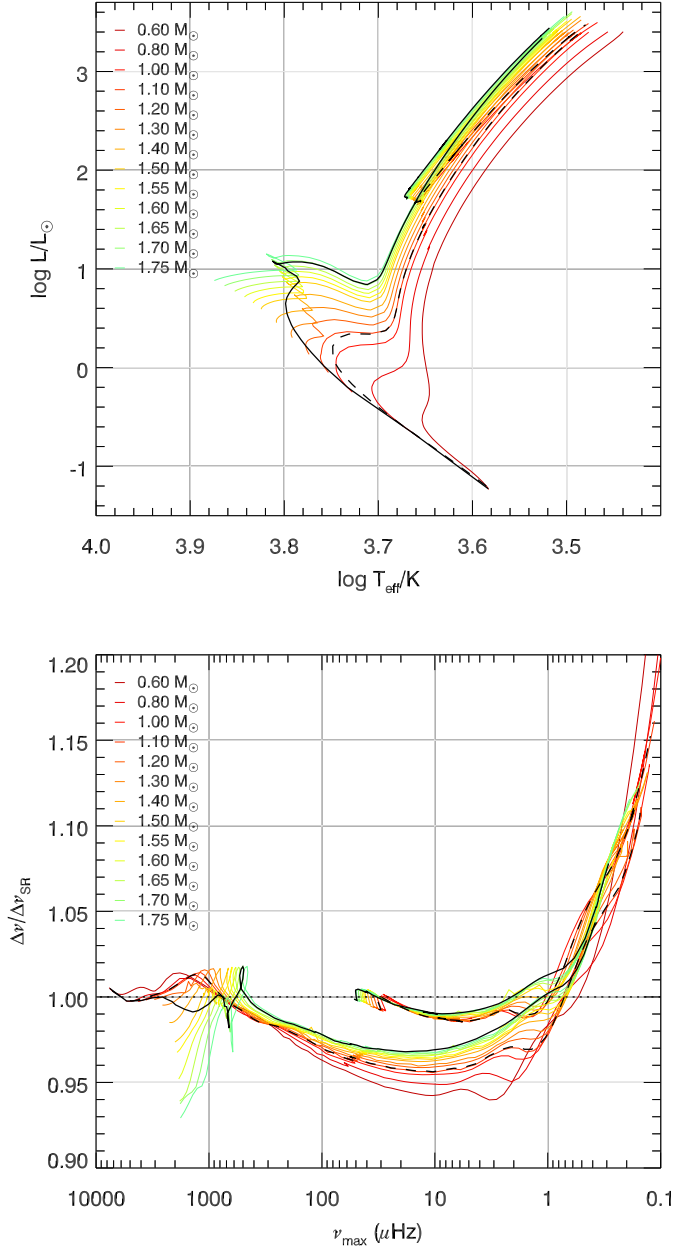
Figure 3.1: MESA evolutionary tracks color coded according to mass in the HR (top panel), $\Delta\nu/\Delta\nu_{\rm SR}$ *versus* $\nu_{\rm max}$(middle), and ΔP *versus* $\Delta\nu$ (bottom) diagrams. The solid and the dashed black lines are examples of interpolated isochrones of 2 and 10 Gyr, respectively.

64
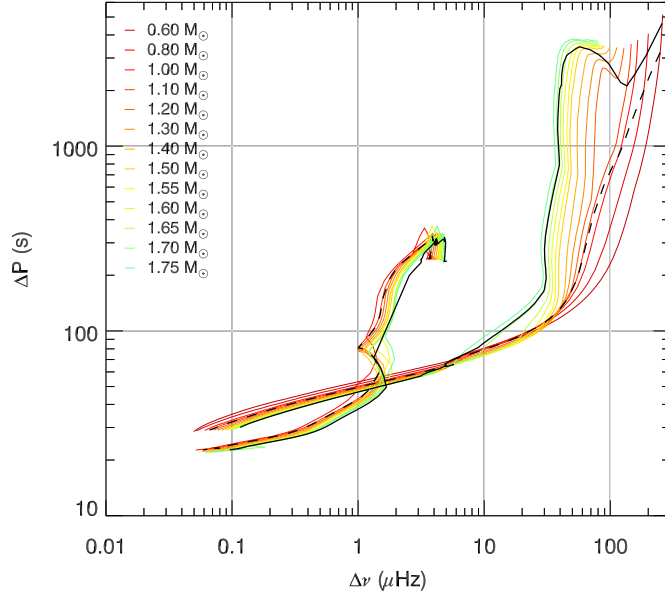
Figure 3.1 continued.

Figure 3.1 shows a set of evolutionary tracks until the TP-AGB phase in the range [0.60,1.75] $M_\odot$ for [Fe/H] = 0.25 ($Z = 0.03123$) and interpolated isochrones of 2 and 10 Gyr both in the Hertzsprung–Russell (HR), the ratio $\Delta\nu/\Delta\nu_{\rm SR}$ *versus* $\nu_{\rm max}$, and the ΔP *versus* $\Delta\nu$ diagrams. The middle panel shows the deviation of the scaling $\Delta\nu$ of few percents mainly over the RGB and early-AGB phases. Deviations at the stages of main sequence and core helium burning are generally smaller than one per cent.

The Fig. 3.1 also shows that our interpolation scheme works very well, with the derived isochrones reproducing the behaviour expected from the evolutionary tracks.

No similar procedure was necessary for the interpolation in ΔP, since it does not follow any simple scaling relation, and it varies much more smoothly and covering a smaller total range than $\Delta\nu$. The interpolations of ΔP are simply linear ones using parameters such as mass, age (along the tracks), and initial metallicity as the independent parameters.

3.3 Applications

We derived the stellar properties using the Bayesian tool PARAM (da Silva et al., 2006; Rodrigues et al., 2014). From the measured data – $T_{\rm eff}$, [M/H], $\Delta\nu$, and $\nu_{\rm max}$– the code computes PDFs for the stellar parameters: M, R, $\log g$, mean density,

absolute magnitudes in several passbands, and as a second step, it combines apparent and absolute magnitudes to derive extinctions A_V in the V band and distances d. The code uses a flat prior for metallicity and age, while for the mass, the Chabrier (2001) initial mass function was adopted with a correction for small amount of mass lost near the tip of the RGB computed from Reimers (1975) law with efficiency parameter $\eta = 0.2$ (cf. Miglio et al., 2012). The code also has a prior on evolutionary stage that, when applied, separates the isochrones into 3 groups: 'core-He burners' (RC), 'non-core He burners' (RGB/AGB), and only RGB (till the tip of the RGB). The statistical method and some applications are described in details in Rodrigues et al. (2014).

We expanded the code to read the additional seismic information of the MESA models described in Section 3.2. We implemented new variables to be taken into account in the likelihood function (equation 2.3), such as $\Delta\nu$ from the model frequencies, ΔP, $\log g$, and luminosity. Hence the entire set of measured data is

$$\mathbf{y} = ([\mathrm{M/H}], T_{\mathrm{eff}}, \Delta\nu, \nu_{\max}, \Delta P, \log g, L),$$

where $\Delta\nu$ can still be computed using the standard scaling relation (hereafter $\Delta\nu(\mathrm{SR})$). Therefore PARAM is now able to compute stellar properties using several different input configurations, i.e., the code can be set to use different combinations of measured data. Some interesting cases are, together with T_{eff} and $[\mathrm{M/H}]$,

- $\Delta\nu$ and $\nu_{\max}$ from scaling relation (equation 3.1);

- $\Delta\nu$ from model frequencies and $\nu_{\max}$ from scaling relation;

- $\Delta\nu$ (either from model frequencies or scaling relation), together with some other asteroseismic parameter, such as ΔP;

- $\log g$;

- any of the previous options together with the addition of a constraint on the stellar luminosity.

The first two cases constitute the main improvement we consider in this paper, which is already subject of significant attention in the literature (see e.g. Sharma et al., 2016; Guggenberger et al., 2016). The third case is particularly important given the fact that the $\nu_{\max}$ scaling relation is basically empirical and may still reveal small offsets in the future. Finally, the fourth and fifth cases are aimed at exploring the effect of lacking of seismic information, when only spectroscopic data is available for a given star; and adding independent information in the method, like e.g. the known distance of a cluster, or of upcoming Gaia parallaxes, respectively.

3.3.1 Tests with artificial data

To test the precision that we could reach with a typical set of observational constraints available for *Kepler* stars, we have chosen 6 models from our grid of models and considered various combinations of seismic, astrometric, and spectroscopic constraints (see Table 3.2).

The seismic constraints taken from the artificial data are $\Delta\nu$, $\nu_{\max}$, and ΔP. The latter is used by taking its asymptotic value as additional constraint in equation 2.3, and not as only a discriminant for the evoltionary phase as done in previous works (e.g. Rodrigues et al., 2014). Uncertainties on $\Delta\nu$ and $\nu_{\max}$ were taken from Handberg et al. (submitted) and on ΔP from Vrard, Mosser & Samadi (2016). We adopted 0.2 dex as uncertainties on $\log g$ based on average values coming from spectroscopy. For luminosity, we adopted uncertainties of the order of 3 per cent based on Gaia parallaxes, where a significant fraction of the uncertainty comes from bolometric corrections (Reese et al., 2016).

We derived stellar properties using 11 different combinations as input to PARAM, in all cases using T_{eff} and [Fe/H], explained as following:

  i $\Delta\nu$ – only $\Delta\nu$ from model frequencies;

  ii $\Delta\nu$ and $\nu_{\max}$ – to compare with the previous item in order to test if we can eliminate the usage of $\nu_{\max}$;

  iii $\Delta\nu(\mathrm{SR})$ and $\nu_{\max}$ – traditional scaling relations, to compare with the previous item and correct the offset introduced by using $\Delta\nu$ scaling;

  iv $\Delta\nu$ and ΔP – in order to test if we can eliminate the usage of $\nu_{\max}$ and improve precision using the period spacing not only as prior, but as a measured data;

  v $\Delta\nu$, $\nu_{\max}$, and ΔP – using all the asteroseismic data available;

  vi $\Delta\nu$, ΔP, and L – in order to test if we can eliminate the usage of $\nu_{\max}$, when luminosity is available (from the photometry plus parallaxes);

  vii $\Delta\nu$, $\nu_{\max}$, ΔP, and L – using all the asteroseismic data available and luminosity, simulating future data available for stars with seismic data observed by Gaia;

  viii $\nu_{\max}$ and L – in the case when it is not possible to derive $\Delta\nu$ from lightcurves, simulating possible data from K2 and Gaia surveys;

  ix $\log g$ and L – in the case when only spectroscopic data are available (in addition to L);

  x $\Delta\nu$ and $\log g$ – again in order to test if we can eliminate the usage of $\nu_{\max}$, replacing it by the spectroscopic $\log g$;

xi $\Delta\nu$ and L – again in order to test if we can eliminate the usage of $\nu_{\max}$, when luminosity is available.

In all cases, the prior on evolutionary stage was also tested. The resulting mass and age PDFs for each artificial star are presented using violin plots[2] in Figure 3.2 and 3.3, respectively. The x axis indicates each combination of input parameters, as discussed before; the left side of the violin (cyan color) represents the resulting PDF when prior on evolutionary stage is applied, while in the right side (white color) the prior is not being used. The violet dots and error bars represent the mode and its 68 per cent credible intervals of the PDF with prior on evolutionary stage (cyan distributions).

Table 3.2: Set of artificial data considered in Section 3.3.1.

Label	$M/\mathrm{M}_\odot$	logAge/yr	T_{eff} (K)	[Fe/H]	$\log g$
S1	1.00	9.8379	4813±70	-0.75±0.1	2.38±0.20
S2	1.00	9.8445	5046±70	-0.75±0.1	2.39±0.20
S3	1.60	9.3383	4830±70	0.0±0.1	2.92±0.20
S4	1.60	9.3461	4656±70	0.0±0.1	2.55±0.02
S5	1.60	9.3623	4769±70	0.0±0.1	2.54±0.20
S6	2.35	8.9120	5003±70	0.0±0.1	2.85±0.20
Label	$L/\mathrm{L}_\odot$	$\nu_{\max}$ (μHz)	$\Delta\nu$ (μHz)	ΔP (s)	Ev. State
S1	54.77±1.64	30.26±0.58	3.76±0.05	61.40±0.61	RGB
S2	64.52±1.94	30.31±0.58	4.04±0.05	304.20±3.04	RC
S3	25.57±0.77	105.01±1.83	8.66±0.05	70.80±0.71	RGB
S4	51.36±1.54	45.99±0.84	4.56±0.05	62.00±0.62	RGB
S5	58.40±1.75	43.97±0.81	4.60±0.05	268.30±2.68	RC
S6	51.41±1.54	86.79±1.54	6.86±0.05	251.20±2.51	RC

In most cases, we recover the stellar masses and ages within the 68 per cent credible intervals. Using only $\Delta\nu$ results in wider and more skewed PDFs (case i in the plots), while adding $\nu_{\max}$ confines the solution in a much smaller region (cases ii and iii). When combining with ΔP, the solution is tied better (case v). In most cases, the combination of $\Delta\nu$ and $\nu_{\max}$ provides narrower PDFs than $\Delta\nu$ and ΔP, which indicates that ΔP does not constrain the solution as tightly as $\nu_{\max}$ (cases ii and iv) even for RC stars. As expected, adding more information as luminosity, narrows the searching "area" in the parameter space which provides the narrowest PDFs when all asteroseismic parameters and luminosity are combined (case vii). The usage of only $\nu_{\max}$ and luminosity (case viii) is very interesting, because it

---

[2]Violin plots are similar to box plots, but showing the smoothed probability density function.
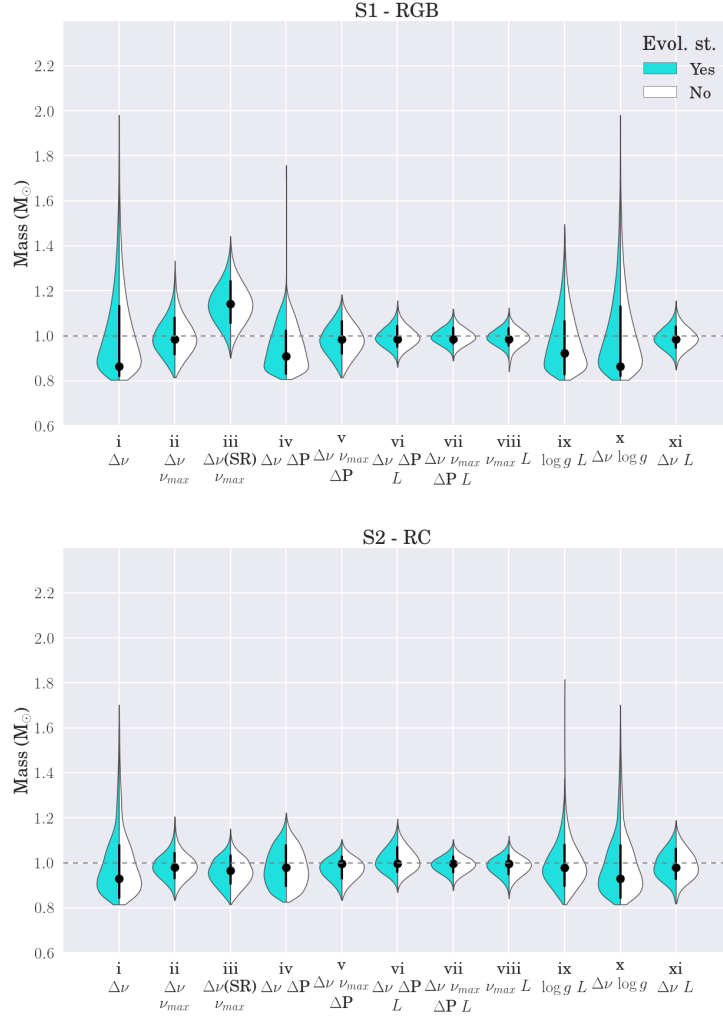
Figure 3.2: PDFs of mass for the 6 artificial stars presented in Table 3.2 using violin plots. Each panel shows the results of one star, named in the top together with its evolutionary stage. The x axis indicates each combination of input parameters for PARAM code as described in Section 3.3.1. The left side of the violin (cyan color) represents the resulting PDF when prior on evolutionary stage is applied, while in the right side (white color) the prior is not being used. The black dots and error bars represent the mode and its 68 per cent credible intervals of the PDF with prior on evolutionary stage (cyan distributions). The dashed line indicates the mass of the artificial stars.

provides PDFs slightly narrower than using the typical combination of $\Delta\nu$ and $\nu_{\max}$ or $\Delta\nu$ and luminosity (case xi), and it is similar to the v and vi cases. The lack
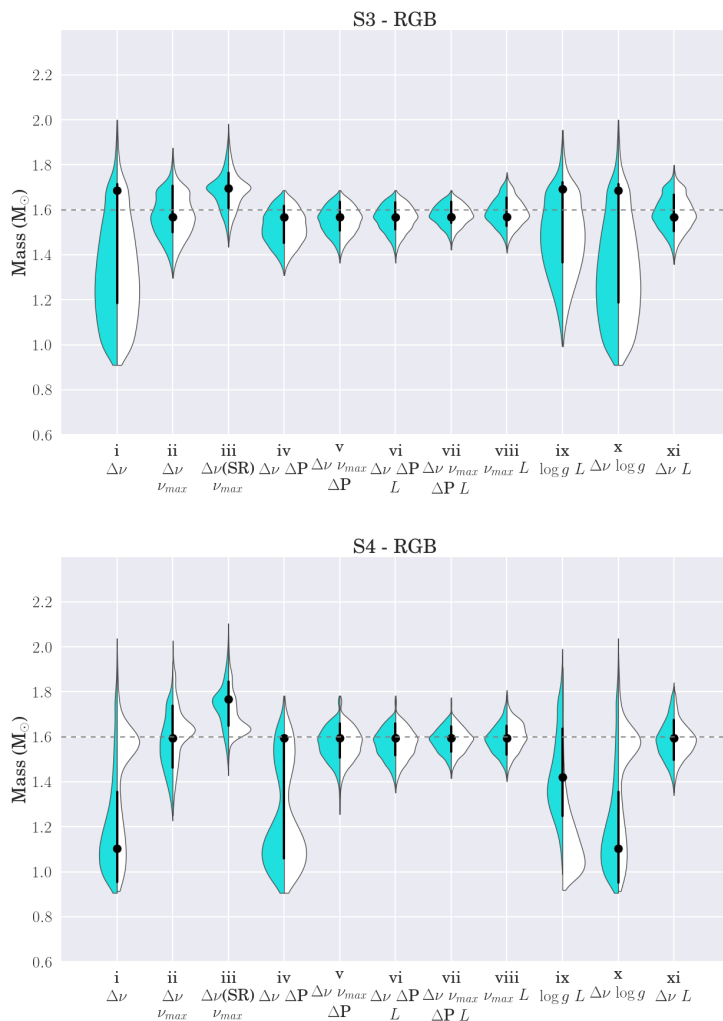
Figure 3.2 continued.

of asteroseismic information (cases ix) worsen the situation, providing a significant larger error bar than most other cases, simply because of large uncertainties on gravity coming from spectroscopic analysis. The case x results in PDFs very similar with case i. This is to be expected: including $\Delta\nu$ as a constraint (case i) leads to a typical $\sigma(\log g) \simeq 0.02$ dex (see also the discussion in Morel et al. 2014, page 4), i.e., adding the spectroscopic $\log g$ ($\sigma(\log g) \simeq 0.2$ dex) as a constraint (case x) has a negligible impact on the PDFs.

Finally, the prior on evolutionary stage does not change the shape of the PDFs in almost all cases, except for the RGB star S4. Regarding this case, it is interesting to note that S4 and S5 have similar $\Delta\nu$ and $\nu_{\max}$, but different ΔP, that is, they

70
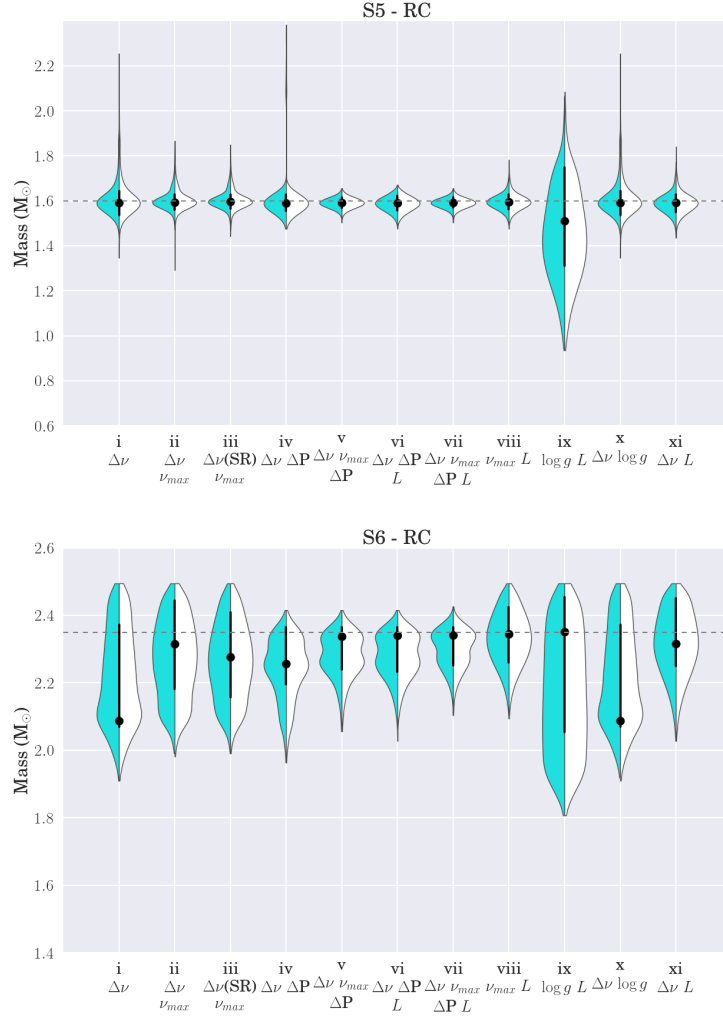
Figure 3.2 continued.

are in a region of the $\Delta\nu$ versus ν_{max} diagram that is crossed by both RC and RGB evolutionary paths. In similar cases, not knowing the evolutionary stage causes the Bayesian code to cover all sections of the evolutionary paths, meaning that there is a large parameter space to cover, which often causes the PDFs to become multi-peaked or spread for all possible solutions as the cases ix and x. Further examples of this effect are given in figure 5 of Rodrigues et al. (2014). Knowing the evolutionary stage, instead, limits the Bayesian code to weight just a fraction of the available evolutionary paths, hence limiting the parameter space to be explored and, occasionally, producing narrower PDFs. This is what happens for star S4, which, despite being a RGB star of 1.6 $M_\odot$, happens to have asteroseismic parameters too

71
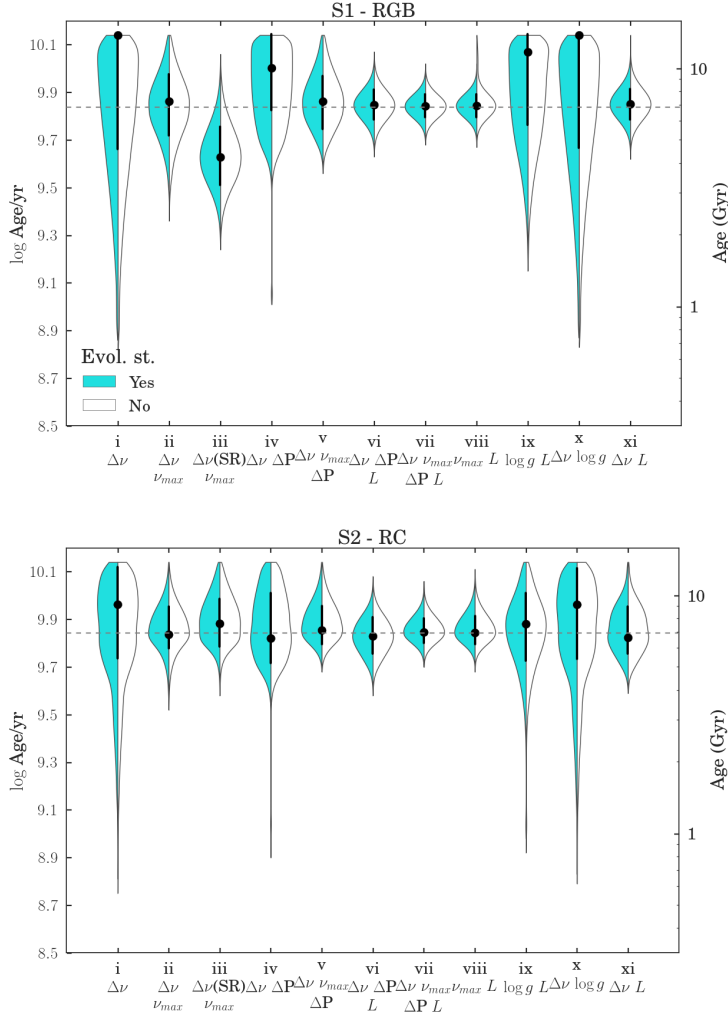
Figure 3.3: The same as figure 3.2 but for logarithm of the ages. The right y-axis gives the age in Gyr. The dashed line indicates the age of the artificial stars.

similar to those the more long-lived RC stars of masses $\sim 1.1\ M_\odot$.

Table 3.3 presents the average relative mass and age uncertainties for RGB and RC stars, which summarizes well the qualitative description given above. Cases i (very similar to case x) and ix results the largest uncertainties: 17 and 12 per cent for RGB, and 8 and 11 for RC masses; up 70 and 40 per cent for RGB, and 22 and 31 for RC ages, respectively. From the traditional scaling relations (case ii) to the addition of period spacing and luminosity (case vii, the uncertainties can decrease from 8 to 3 per cent for RGB and 5 to 3 for RC masses; 29 to 10 per cent for RGB and 14 to 8 for RC ages. It is remarkable that we can also achieve a precision around
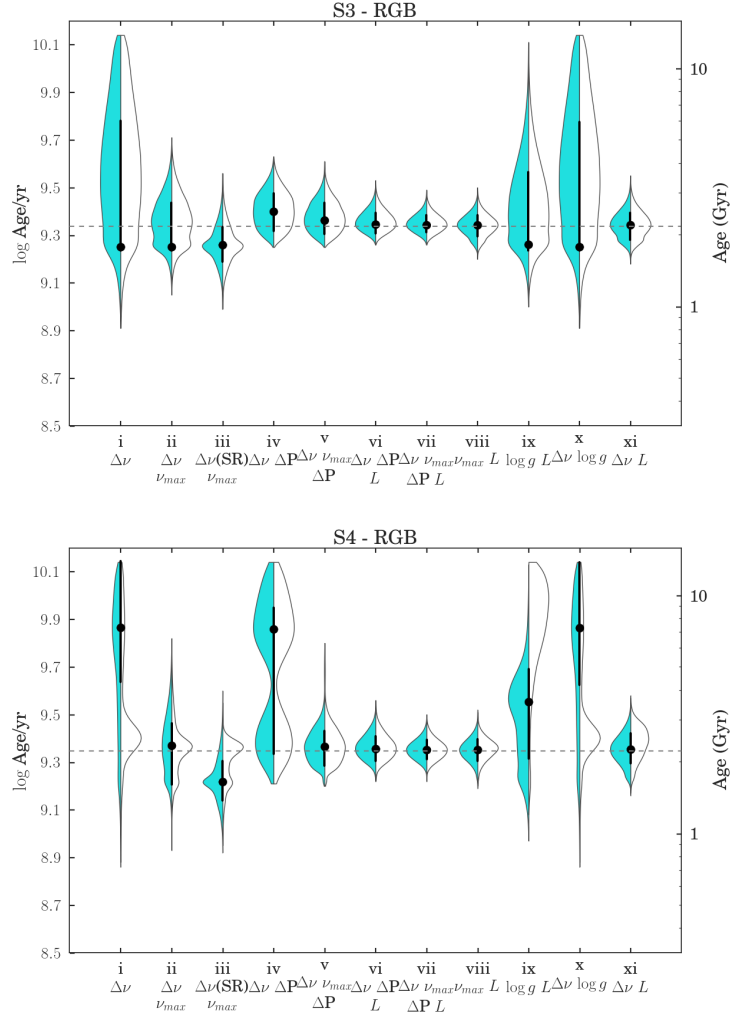
Figure 3.3 continued.

10 per cent on ages using $\nu_{\max}$ and luminosity (case viii), and 15 per cent using $\Delta\nu$ and luminosity (case xi).

Average relative differences between masses are ≤ 1 per cent for cases v, vi, vii, and viii, around 1 per cent for cases ii and xi, ~ 6 per cent for case iii, and greater than 6 per cent for cases i, ix, and x. Regarding ages, relative absolute differences are lesser than 5 per cent for cases v, vi, vii, viii, and xi, around 10 per cent when using $\Delta\nu$ and $\nu_{\max}$, ~ 20 per cent when using $\Delta\nu(SR)$ and $\nu_{\max}$, and greater than 40 per cent for cases i, ix, and x.

We also applied mass loss on the models. Figure 3.4 shows the resulting mass and age PDFs for stars S2 and S5 with the efficiency parameter $\eta = 0.2$ (cyan colors)
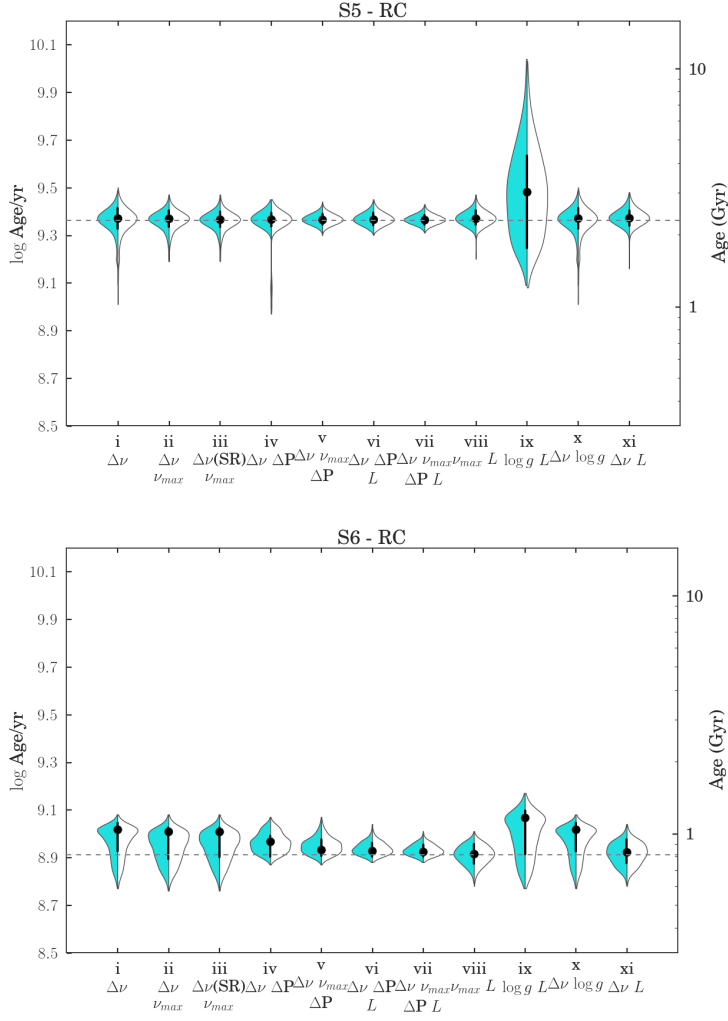
Figure 3.3 continued.

and $\eta = 0.4$ (white colors). For the cases v, vi, vii, viii, and xi, a mass loss with efficiency $\eta = 0.4$ produces differences on masses of ~ 1 per cent, while on ages, may be greater than 47 per cent for S2 and than 18 per cent for S5. The small difference in masses results from the fact that, in these cases, mass values follow almost directly from the observables – roughly speaking, they represent the mass of the tracks that pass closer to the observed parameters. As well known, red giant stars quickly lose memory of their initial masses and follow evolutionary tracks which are primarily just a function of their actual mass and surface chemical composition. So their derived masses will be almost the same, irrespective of the mass loss employed to compute previous evolutionary stages. But the value of η will affect the relationship
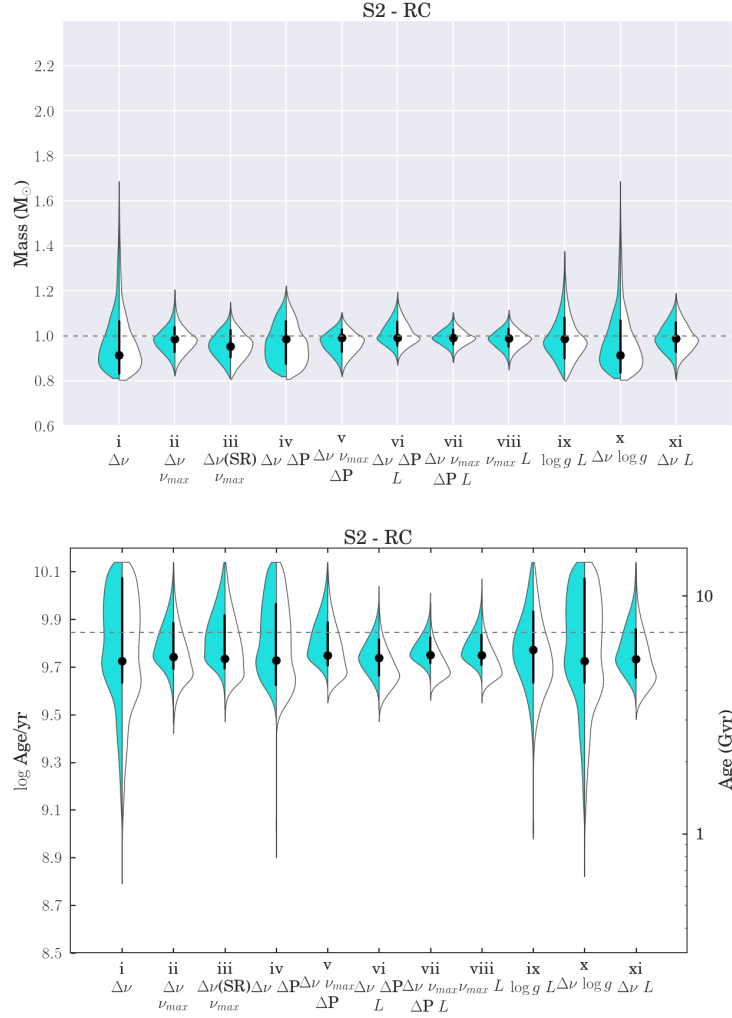
Figure 3.4: PDFs of mass (top panels) and ages (bottom panels) for the artificial RC stars S2 and S5 presented in Table 3.2 using violin plots. The left side of the violin (cyan color) represents the resulting PDF with the efficiency parameter on mass loss $\eta = 0.2$, while in the right side (white color) $\eta = 0.4$. The black dots and error bars represent the mode and its 68 per cent credible intervals of the PDF with $\eta = 0.2$ (cyan distributions). The dashed line indicates the mass and the ages of the artificial stars.

between the actual masses and the initial ones at the main sequence, which are those that determine the stellar age. For instance, S2 have nearly the same actual mass (very close to 1 $M_\odot$) for both $\eta = 0.2$ and $\eta = 0.4$ cases, but this actual mass can derive from a star of initial mass close to 1.075 $M_\odot$ in the case of $\eta = 0.2$, or from
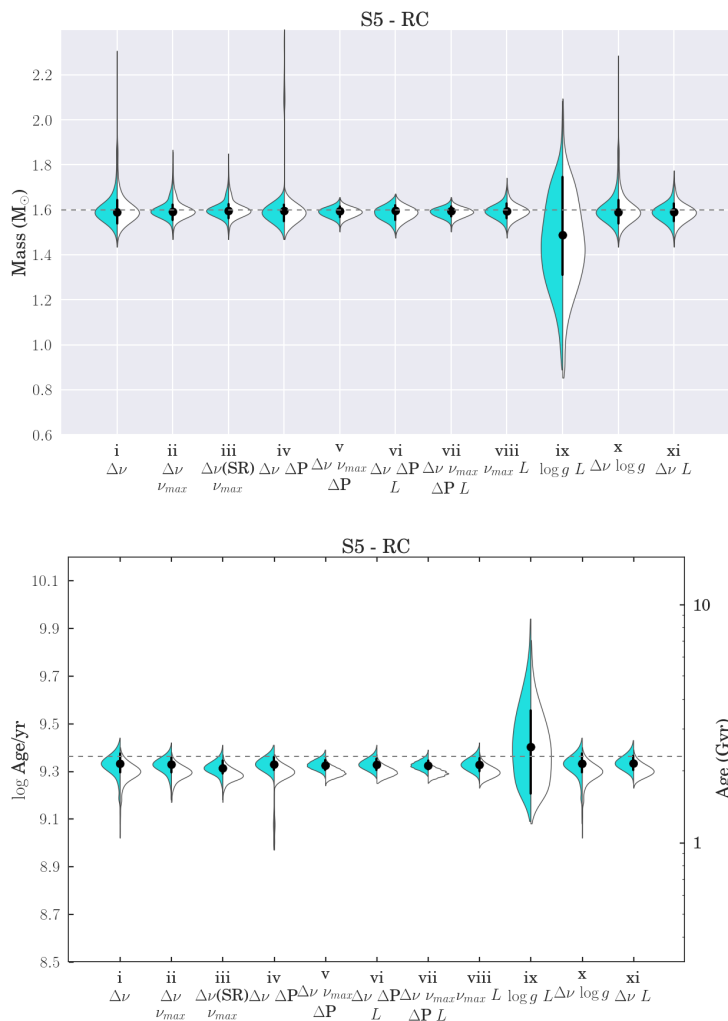
Figure 3.4 continued.

a star of initial mass close to 1.15 $M_\odot$ in the case of $\eta = 0.4$. This ~ 13 per cent difference in the initial, main sequence mass is enough to explain the ~ 47 per cent difference in the derived ages of S2. More in general, this large dependence of the derived ages on the assumed efficiency of mass loss, warns against trusting on the ages of RC stars.

3.3.2 NGC 6819

The previous section demonstrates that it is possible to recover, generally within the expected 68 per cent (1σ) credible interval expected from observational errors,

Table 3.3: Average relative uncertainties for each combination of input parameters for PARAM code as described in Section 3.3.1.

	Case	$< \sigma M/M >$		$< \sigma \mathrm{Age}/\mathrm{Age} >$	
		RGB	RC	RGB	RC
i	$\Delta\nu$	0.173	0.077	0.734	0.217
ii	$\Delta\nu$, $\nu_{\max}$	0.078	0.045	0.284	0.144
iii	$\Delta\nu(\mathrm{SR})$, $\nu_{\max}$	0.061	0.047	0.220	0.146
iv	$\Delta\nu$, ΔP	0.109	0.052	0.336	0.181
v	$\Delta\nu$, $\nu_{\max}$, ΔP	0.054	0.030	0.192	0.109
vi	$\Delta\nu$, ΔP, L	0.043	0.035	0.122	0.101
vii	$\Delta\nu$, $\nu_{\max}$, ΔP, L	0.034	0.025	0.097	0.075
viii	$\nu_{\max}$, L	0.039	0.033	0.107	0.102
ix	$\log g$, L	0.124	0.108	0.427	0.310
x	$\Delta\nu$ $\log g$	0.173	0.077	0.727	0.215
xi	$\Delta\nu$ L	0.052	0.046	0.143	0.146

the masses and ages of artificial stars. It is not granted that a similar level of accuracy will be obtained in the analysis of real data. Star clusters, whose members are all expected to be at the same distance and share a common initial chemical composition and age, offer one of the few possible ways to actually verify this. Only four clusters have been observed in the *Kepler* field (Gilliland et al., 2010), and among these NGC 6819 represents the best case study, owing to its brightness, its near-solar metallicity (for which stellar models are expected to be better calibrated) and the large numbers of stars in *Kepler* database. NGC 6791 has even more giants observed by *Kepler*; however its super-solar metallicity, the uncertainty about its initial helium content, and larger age – causing a non-negligible mass loss before the RC stage – makes any comparison with evolutionary models more complicated.

Handberg et al. (submitted) reanalysed the raw *Kepler* data of the stars in the open cluster NGC 6819 and extracted individual frequencies, heights, and linewidths for several oscillation modes. They also derived the average seismic parameters and stellar properties for $\sim$50 red giant stars based on targets of Stello et al. (2011). Effective temperatures were computed based on $V - K_s$ colours with bolometric correction and intrinsic colour tables from Casagrande & VandenBerg (2014), and adopting a reddening of $E(B - V) = 0.15$ mag. They derived masses and radii using scaling relations, and computed apparent distance moduli using bolometric corrections from Casagrande & VandenBerg (2014). The authors also applied an empirical correction of 2.54 per cent to the $\Delta\nu$ of RGB stars, thus making the mean distance of RGB and RC stars to become identical. As we based the definition of the average $\Delta\nu$ for MESA models similar to the one used in Handberg et al.

(submitted)'s work, we adopted their values for the global seismic ($\Delta\nu$ and $\nu_{\max}$) and spectroscopic (T_{eff}) parameters. We verified that their T_{eff} scale is just ~ 57 K cooler than the spectroscopic measurements from the APOGEE Data Release 12 (Alam et al., 2015). The metallicity adopted was [Fe/H] $= 0.02 \pm 0.10$ dex for all stars. We also adopted period spacing values from Vrard, Mosser & Samadi (2016), who automatically measured ΔP for more than 6000 stars observed by *Kepler*. In order to derive distances and extinctions in the V-band (A_V), we also used the following apparent magnitudes: SDSS $griz$ measured by the KIC team (Brown et al., 2011) and corrected by Pinsonneault et al. (2012); JHK_s from 2MASS (Cutri et al., 2003; Skrutskie et al., 2006); and $W1$ and $W2$ from WISE (Wright et al., 2010).

We computed stellar properties for 52 stars that have T_{eff}, [Fe/H], $\Delta\nu$, and $\nu_{\max}$ available using case ii and iii; and for 20 stars that have also ΔP measurements using case v. Table 3.4 presents the average relative uncertainties on masses and ages for these stars. These average uncertainties are slightly smaller than the ones from our test with artificial stars in the previous section.

Table 3.4: Average relative uncertainties on masses and ages for stars in NGC 6819 using the combination of input parameters ii, iii, and v for PARAM code.

Case		$< \sigma M/M >$		$< \sigma \text{Age}/\text{Age} >$	
		RGB	RC	RGB	RC
ii	$\Delta\nu$, $\nu_{\max}$	0.057	0.026	0.210	0.100
iii	$\Delta\nu(\text{SR})$, $\nu_{\max}$	0.044	0.026	0.161	0.102
v	$\Delta\nu$, $\nu_{\max}$, ΔP	0.013	0.021	0.050	0.077

Figure 3.5 shows the masses and ages derived using PARAM with case ii and iii as observational input. The blue and red colors represent RC and RGB stars, respectively. The median and mean relative differences between stellar properties are presented in Table 3.5. The RGB stars have masses ~ 8 per cent greater when using $\Delta\nu$ scaling relation, while many RC stars present no difference and only few of them have smaller masses (≈ 2 per cent). The mass differences reflects RGB stars being on average ~ 18 per cent younger and no significant differences on RC stars. The ~ 5 per cent difference on RGB radii reflects on the same difference on distances.

Figure 3.6 shows the masses and ages derived using case ii and v as observational input. The average relative uncertainties are much smaller for RGB stars when adding ΔP as an observational constraint (see Table 3.4). The agreement on masses is very good, except for massive stars, when masses are around the upper mass limit of our grid ($2.50\ M_\odot$). Two over-massive stars result ~ 10 per cent less massive when adding ΔP (KIC 5024476 and 5112361). The ages also present a good agreement inside the error bars, although with a dispersion of ~ 5 per cent.

Table 3.5: Median and mean relative (and absolute) differences between properties estimated using case ii and iii for RGB and RC stars from NGC 6819.

properties	RGB		RC	
	median	mean	median	mean
masses	0.088	0.079	0.000	-0.012
ages	-0.195	-0.180	-0.002	-0.004
radii	0.048	0.043	0.000	-0.007
A_V	0.005	0.031	0.001	0.001
distances	0.047	0.045	-0.001	-0.006

The top panel of figure 3.7 shows the comparison between masses estimated with case ii versus masses from Handberg et al. (submitted). The masses have a good agreement with a dispersion of ~ 7 per cent, showing that the proposed correction of 2.54 per cent on $\Delta\nu$ for RGB stars in Handberg et al. (submitted) compensates the deviations when using $\Delta\nu$ scaling. The authors also discussed in details some stars that seem to experience *non-standard* evolution based on their masses and distances estimations and on membership classification based on radial velocity and proper motion study by Milliman et al. (2014). These stars are represented with different symbols in all figures of this section: asterisks – non-member stars (KIC 4937257, 5024043, 5023889); diamonds – stars classified as overmassive (KIC 5024272, 5023953, 5024476, 5024414, 5112880, 5112361); squares – uncertain cases (KIC 5112974, 5113061, 5112786, 4937770, 4937775); triangle – Li–rich low mass RC (KIC 4937011). A similar detailed description star by star is not the scope of the present paper, however the peculiarities of these stars should be kept on mind when deriving their stellar and the cluster properties. Some of the over-massive stars do not have a good agreement, because of the upper mass limit of our grid of models ($2.5 M_\odot$).Taking into account only single member stars, the mean masses of RGB and RC stars using case ii are 1.61 ± 0.04 $M_\odot$ and 1.62 ± 0.03 $M_\odot$, which also agree with the ones found in Handberg et al. (submitted) and Miglio et al. (2012)..

The bottom panel of figure 3.7 shows the comparison between distance moduli estimated with case ii versus distance moduli in the V-band estimated in Handberg et al. (submitted). The solid line represents the linear regression $\mu_0 = \mu_V(\text{Handberg}) - A_V$, which results $A_V = 0.475 \pm 0.003$ mag that is in a good agreement with the average extinction for the cluster (see Fig. 3.8). Our method estimates the extinction star-to-star and it varies significantly in the range $A_V = [0.3, 0.7]$ for the stars in the cluster. This seems to be in agreement with Platais et al. (2013) that shown a substantial differential reddening in this cluster with the maximum being $\Delta E(B-V) = 0.06$ mag, what implies extinctions in the V-band in the same range
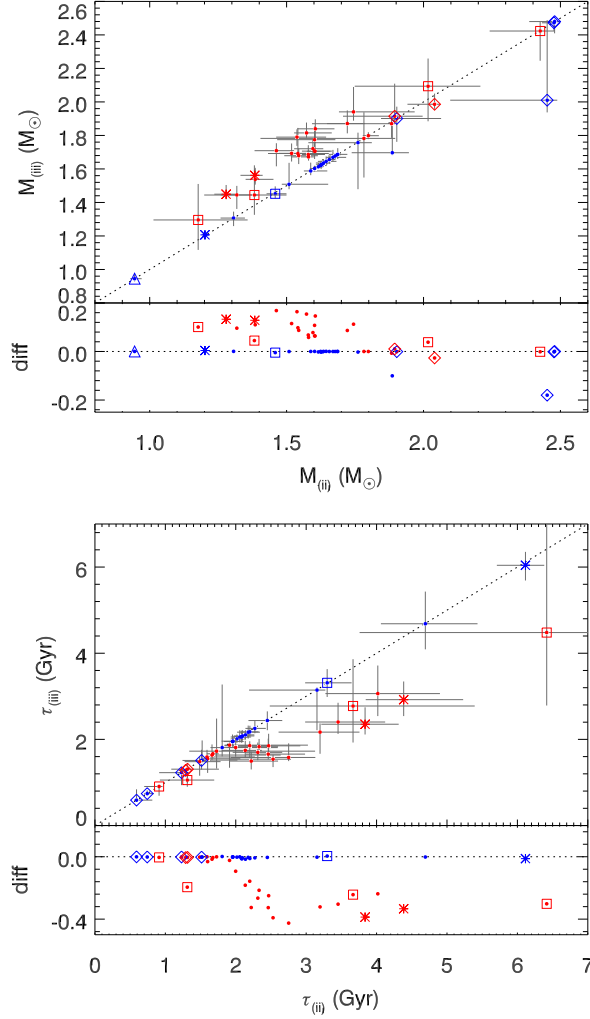
Figure 3.5: Comparison between masses (top panel) and ages (bottom) estimated with case ii versus case iii. The bottom panel excludes KIC 4937011 (Li-rich low mass RC) that has an estimated age in both cases of ∼ 13.8 Gyr. Sub-panels show relative differences. Dotted black lines are the identity line. The blue and red colors represent RC and RGB stars, respectively. Different symbols are peculiar stars that were discussed in details in Handberg et al. (submitted) – asterisks are stars classified as non-member; diamonds: stars classified as over-massive; squares: uncertain cases; triangle: Li-rich low mass RC (KIC 4937011).

that we found. Extinctions and distance moduli estimated using case ii are presented in Figure 3.8. The average uncertainties on extinctions and distance moduli
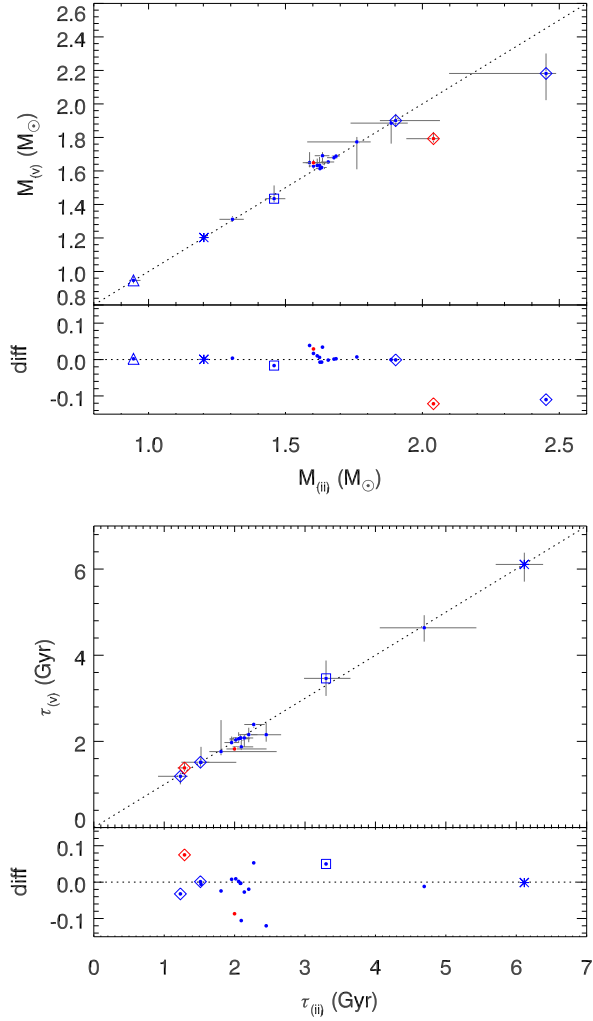
Figure 3.6: Same as Fig. 3.5, but with case ii versus case v.

are 0.1 mag and 0.03 mag (< 2 per cent on distances), respectively. We derived the distance for the cluster by computing the mean distances, $\mu_0 = 11.90 \pm 0.04$ mag with a dispersion of 0.23 mag (solid and dashed black lines in Figure 3.8), excluding stars classified as non-member (asterisks) by Handberg et al. (submitted). This value compares well with distance moduli measured for eclipsing binaries, $\mu_0 = 12.07 \pm 0.07$ mag (Jeffries et al., 2013).

Figure 3.9 shows the histogram of the age estimated using case ii. The gray line represents the histogram of all stars, except the 3 stars classified as non-member and the star KIC 4937011 that has estimated age of ~ 13.8 Gyr. Red and blue
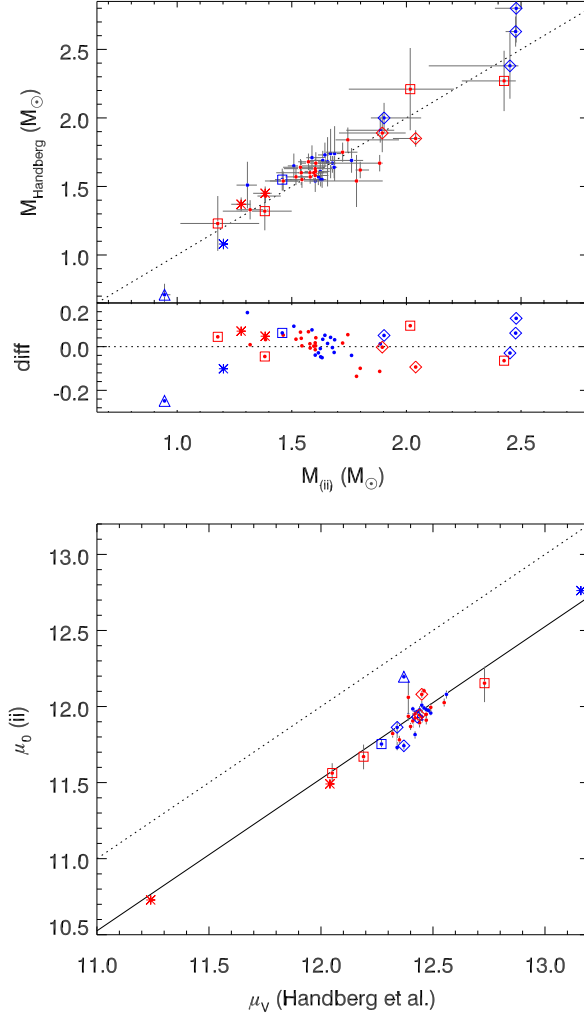
Figure 3.7: Comparison between masses (top panel) and distance moduli (bottom) estimated with case ii and from Handberg et al. (submitted). Dotted black lines are the identity line. The blue and red colors represent RC and RGB stars, respectively. Different symbols are the same as Fig. 3.5. The solid black line in the bottom panel shows the agreement between our distance with the distance in the V-band, representing a measurement of the extinction.

lines represent the ages of RGB and RC stars. The mean age by the gray histogram is 2.22 ± 0.15 Gyr with a dispersion of 1.01 Gyr, that agrees with the age estimated by fitting isochrones to the cluster CMDs by Brewer et al. (2016) ($2.21 \pm 0.10 \pm 0.20$

Gyr). Taking into account only stars classified as single members (31 stars), i.e. excluding stars that are binary members, single members flagged as over-under massive and with uncertain parameters classified according to Handberg et al. (submitted), the mean age results 2.25 ± 0.12 Gyr with a dispersion of 0.64 Gyr. Importantly, RGB and RC apparently share the same age distribution, i.e. there is no evidence of systematic differences in the ages of the two groups of stars. This result reflects taking into consideration the deviations from scaling relations, which are quite relevant for RGB stars but smaller for the RC. Adding ΔP (case v), the mean age is 2.12 ± 0.19 Gyr with a dispersion of 0.79 Gyr, excluding the star KIC 4937011 and also the one classified as non-member KIC 4937257 (triangle and asterisk symbols in Figure 3.6). For this case, there are 13 stars classified as single member according to Handberg et al. (submitted), whose mean age is 2.18 ± 0.20 Gyr with a dispersion of 0.73 Gyr. In the case with $\Delta\nu$ scaling (case iii) the mean age is 1.95 ± 0.11 Gyr (dispersion of 0.78 Gyr, computed also excluding the 3 stars classified as non-member and the star KIC 4937011), 12 per cent younger than using $\Delta\nu$ from models.
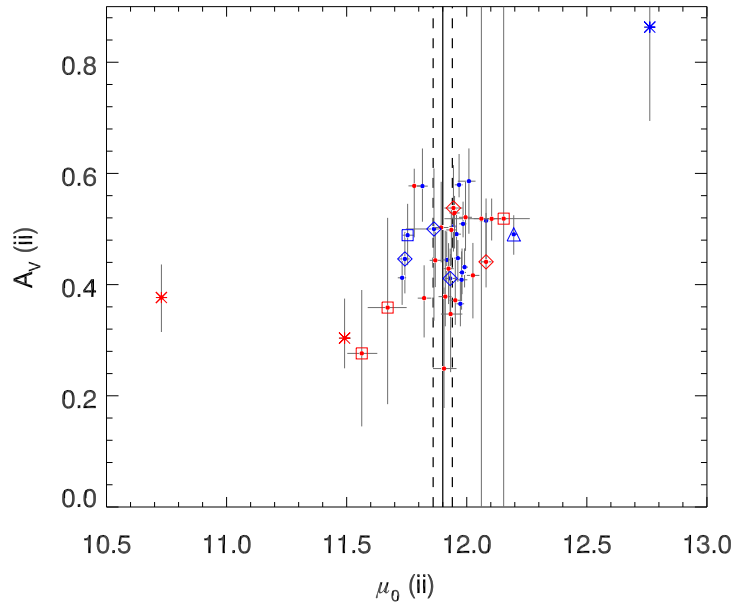
Figure 3.8: Extinction versus distance moduli estimated with case ii. The blue and red colors represent RC and RGB stars, respectively. Solid and dashed black lines are the mean and its uncertainty of distance moduli computed taking into account all stars, except for the ones classified as non-member (asterisks) by Handberg et al. (submitted). Different symbols are the same as Fig. 3.5.

Figure 3.10 shows the color-magnitude diagram (CMD) for the cluster stars with
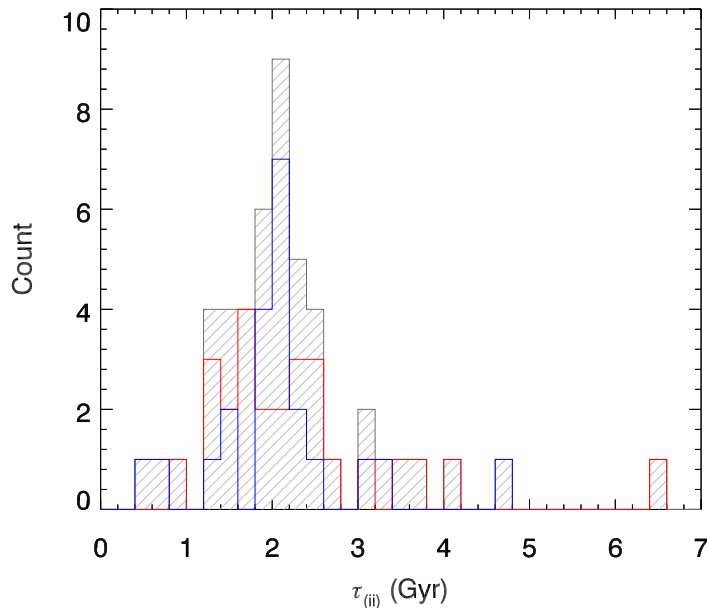
Figure 3.9: Histogram of ages estimated using case ii. The gray line represents all stars, except the ones classified as non-members stars and KIC 4937011 that has ~ 13.8 Gyr. Red and blue lines represent the ages of RGB and RC stars.

membership probability ≥ 90 per cent according to radial velocity by Hole et al. (2009) (gray dots). The red and blue symbols are the stars analysed in the present work. There is a significant dispersion on the RGB and RC, but still our isochrones match well the photometry. This points to a significant consistency between the ages of evolved stars derived from asteroseismology, and the CMD-fitting age which would be derived from the photometry. This particular result, however, should not be generalised, since it applies only to the specific set of stellar models and cluster data that has been used here.

Another important aspect, however, is that the ages derived for cluster stars turn out to present a larger scatter than expected. If we assume that all cluster stars really have the same age, their mean standard deviation implies that the final errors in the ages are of roughly 46 per cent, which is a factor of 2 larger than the individual age uncertainties for the case ii (see Table 3.4).

The scatter is reduced when excluding from the sample stars that are binary members, single members flagged as over-under massive and with uncertain parameters classified according to Handberg et al. (submitted). In this case the scatter (28 per cent) is higher, but comparable with, the expected uncertainty (21 per cent).

84
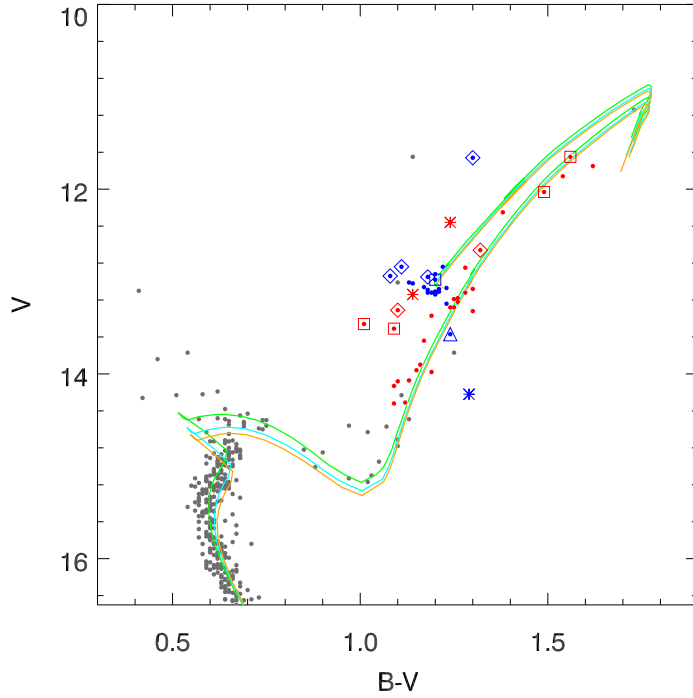
Figure 3.10: CMD for the cluster stars with membership probability ≥ 90 per cent according to radial velocity by Hole et al. (2009) (gray dots). The blue and red colors represent RC and RGB stars, respectively. Different symbols are the same as Fig. 3.5. The green, cyan, and orange lines are MESA isochrones with ages 2.0, 2.2, and 2.3 Gyr, using $\mu_0 = 11.90$ mag and $E(B - V) = 0.14$ mag.

At present, the origin of this increased age dispersion is not clear. We note however that the NGC 6819 giants are also dispersed around the best-age isochrones in the CMD. The magnitude of this dispersion is not simply attributable to differential reddening or photometric errors (Hole et al., 2009; Milliman et al., 2014; Brewer et al., 2016). Therefore, it is possible that it reflects some physical process acting in the individual cluster stars, rather than a failure in the method.

We also notice that in the cluster CMD (Fig. 3.10) the main sequence turn-off is well-defined and the comparison with isochrones appear to rule out internal age spreads larger than ~ 0.2 Gyr. Even larger age spreads have been suggested to explain the very extended (and sometimes bimodal) main sequence turn-offs observed in some very massive star clusters in the Magellanic Clouds (Goudfrooij et al., 2015, and references therein). However, there is no evidence of a similar feature occurring in the photometry of NGC 6819.

Chapter 4

Conclusions

In the first part of our project, we have employed a Bayesian method to determine basic stellar parameters (mass, surface gravity, radius), distances, and extinctions for 1989 giants present in the first version of the APOKASC catalogue (Pinsonneault et al., 2014). The results are very encouraging: distances and extinctions are derived with very small formal uncertainties, for stars located as far away as 5 kpc. The vast majority of the stars produced results that are internally consistent, well-behaved, and considered reliable. The final diagnostics of the correctness of our distances and extinctions come essentially from three sources: (1) for regions of the *Kepler* field for which very small extinction is expected from the SFD dust maps, our own extinction maps do not show evidence of systematic offsets. (2) Stars in the NGC 6791 and NGC 6819 star clusters present essentially the same distances, with small variations in their extinctions. (3) Stars in the APOGEE-RC catalogue (Bovy et al., 2014) – which are very likely RC stars and hence can be assigned precise *Hipparcos*-calibrated spectrophotometric distances – correlate well with our independent distances.

In the second part of our project, we have implemented our code PARAM with the spectroscopic $\log g$ in order to estimate distances and extinctions to RGB stars in the DR12 from APOGEE survey. However the uncertainties on spectroscopic $\log g$ are one order of magnitude greater than the asteroseismic ones, the APOGEE distances and extinctions are in good agreement with the APOKASC ones. Using only spectroscopic parameters, the average uncertainties increased from 2 to 7 per cent for distances, and from 0.08 to 0.21 mag for extinctions. The extinctions are also in a good agreement with reddening maps in the literature. Finally we computed distances and extinctions for the entire APOKASC survey using spectroscopic data from APOGEE DR13 and seismic data using the pipeline of (Mosser & Appourchaux, 2009).

The present results are also very encouraging for the application of these distances and extinctions in studies of Galactic structure and evolution. The distance and extinction values of the first data release of APOKASC were made available

for download with the paper on the journal website (Rodrigues et al., 2014). A sample table is reported in Table 4.1. Interestingly, our distance determinations are becoming widely used by other groups (Santiago et al., 2016; Rezaei Kh. et al., 2016), even for testing the first parallaxes releases by the Gaia astrometric mission (De Ridder et al., 2016). Our results for the second data release of APOKASC will be published together with the catalogue paper (Pinsonneault et al., in preparation) and the grid-based analysis (Elsworth et al., in preparation).

In the third part of our project already published in Rodrigues et al. (2017), we implemented the asteroseismic properties $\Delta\nu$ and ΔP, computed along detailed grids of stellar evolutionary tracks in our code PARAM. It will be soon become available for public use through the web interface http://stev.oapd.inaf.it/param. Our main conclusions are:

- Tests with synthetic data reveal that masses and ages can be determined with typical precision of 5 and 19 per cent, if precise global seismic parameters ($\Delta\nu$, ν_{max}, ΔP) are available. Adding luminosity these values can decrease to 3 and 10 per cent, respectively.

- Combining the luminosity expected from the end-of-mission Gaia parallaxes with $\Delta\nu$, enables us to infer masses (ages) to ~ 5 per cent (~ 15 per cent) independently from the ν_{max} scaling relation, which is still lacking a detailed theoretical understanding (but see Belkacem et al. 2011). A similar precision on mass and age is also expected when combining luminosity and ν_{max}: this will be particularly relevant for stars where data are not of sufficient quality/duration to enable a robust measurement of $\Delta\nu$. Stringent tests of the accuracy of the ν_{max} scaling relation (as in Coelho et al., 2015) are therefore of great relevance in this context.

- Any estimate based on asteroseismic parameters is at least a factor 4 more precise than those based on spectroscopic parameters alone.

- The application of these methods to NGC 6819 giants produces mean age of 2.22 ± 0.15 Gyr, distance $\mu_0 = 11.90 \pm 0.04$ mag, and extinctions $A_V \approx 0.475 \pm 0.003$ mag. All these values are in agreement with estimates derived from photometry alone, via isochrone fitting.

- Despite these encouraging results, the application of the method to NGC 6819 stars also reveals a few caveats and far-from-negligible complications. Even after removing some evident outliers (likely non members) from the analyses, the age dispersion of NGC 6819 stars turns out to be appreciable, with the $\tau = 2.22 \pm 0.15$ Gyr with a dispersion of 1.01 Gyr, implying a ~ 46 per cent error on individual ages (or ~ 28 per cent taking into account only single members

and removing over-massive stars indentified in Handberg et al. submitted). The mean age value is compatible with those determined with independent methods (e.g. the $\tau = 2.21 \pm 0.10 \pm 0.20$ Gyr from isochrone fitting).

The result of a large age dispersion for NGC 6819 stars is no doubt surprising, given the smaller typical errors found during our tests with artificial data. Since asteroseismology is now widely regarded as the key to derive precise ages for large samples of field giants distributed widely across the Galaxy, this is surely a point that has to be understood: it is obvious that any uncertainty or systematics affecting the NGC 6819 stars will also affect the analyses of the field giants observed by asteroseismic missions.

We could point out that, on the one hand, a clear source of bias in age is the presence of over/under-massive stars which are likely to be the product of binary evolution. Additionally, even restricting ourselves to RGB stars and weeding out clear over/under massive stars we are left with an age/mass spread which is larger than expected. Grid-based modelling increases the significance of this spread, compared to the results presented in Handberg et al. (submitted).

Whether this spread is an effect specific to the age-metallicity of NGC 6819, is yet to be determined. Previous works on NGC 6791 and M 67, for instance, have not reported on a significant spread in mass/age of their asteroseismic targets (Basu et al., 2011; Miglio et al., 2012; Corsaro et al., 2012; Stello et al., 2016). These three clusters are different in many aspects, with NGC 6791 being the most atypical one given its very high metallicity. Apart form this obvious difference, in both NGC 6791 and M 67 the evolved stars have masses smaller than 1.4 $M_\odot$, and were of spectral type mid/late-F or G – hence slow rotators – while in their main sequence. In NGC 6819 the evolved stars have masses high enough to be "retired A-stars", which includes the possibility of having been fast rotators before becoming giants. This is a difference that could, at least partially, be influencing our results. Indeed, rotation during the main sequence is able to change the stellar core masses, chemical profile, and main sequence lifetimes (Eggenberger et al., 2010; Lagarde et al., 2016). A spread in rotational velocities among coeval stars might then cause the spread in the properties of the red giants, which might not be captured in our grids of non-rotating stellar models. The possible impact of rotation in the grid-based and Bayesian methods, has still to be investigated.

On the other hand, this ~ 46 per cent uncertainty is comparable to the 0.2 dex uncertainties that are obtained for the ages of giants with precise spectroscopic data and *Hipparcos* parallax uncertainties smaller than 10 per cent (Feuillet et al., 2016), which refer to stars within 100 pc of the Sun. In this sense, our results confirm that asteroseismic data offers the best prospects to derive astrophysically-useful ages for individual, distant stars.

4.1   Perspectives

The Bayesian method we have implemented in the PARAM code is quite versatile. Other sets of evolutionary tracks, stellar poperties, Bayesian priors, and survey data can be easily considered in alternative to those used in this work. Therefore, it is obvious that we plan to extend the range of applications of this code in the near future. Our immediate priorities in this sense regard the APOKASC sample, which is still being analysed by different groups. In particular, the spectroscopic analysis is still being improved by the ASPCAP team, with small systematic errors being removed and with the abundances of many elements becoming more reliable. In addition, other and more accurate seismic parameters are being provided by the KASC team. On the other hand, also our theoretical tools are being revised. We can foresee the following novelties being explored in the next months:

- New PARSEC stellar evolutionary tracks computed by Fu et al. (in preparation), considering the enhancement of α elements, are now being implemented in the PARSEC isochrones. As soon as they are ready, we will be able to reprocess the APOKASC and APOGEE catalog properly taking into account the $[\alpha/M]$ measured for each star.

- Many stars in the APOKASC sample have new asteroseismic parameters already measured, in particular the small frequency separation. This quantity will be computed along our MESA tracks and isochrones, to allow us to use it in PARAM along the other parameters. The primary goal of this addition is to improve the age determinations (Montalbán et al., 2012; Davies & Miglio, 2016).

- Gaia parallaxes are becoming available. The Gaia DR1 catalog includes the astrometric solution obtained from the combination of Tycho plus 1-year of Gaia measurements (Tycho-Gaia astrometric solution, TGAS; Lindegren et al., 2016). We will soon recompute the parameters for the few hundreds of stars in the matched APOKASC+TGAS and APOGEE+TGAS catalogs, including the new parallaxes as a constraint. This work is preparatory for the Gaia DR2, which will release accurate parallaxes for a huge sample of stars.

4.2   Other ongoing projects

We also worked in other projects as a result of collaborations with researchers inside the APOGEE, APOKASC, and APOKASC-2 teams.

- We computed stellar properties, distances, and extinctions for red giant stars in the CoRoT survey:

- with spectroscopic data from APOGEE survey (CoRoGEE) in collaboration with Cristina Chiappini[1] and Friedrich Anders[1] – Chiappini et al. (2015); Anders et al. (2016b,a,c);

- with spectroscopic data from Gaia-ESO survey (CoRoGES) in collaboration with Marica Valentini[1] and Cristina Chiappini[1] – Valentini et al. (2016b)

- We computed stellar properties, distances, and extinctions for red giant stars with spectroscopic data from RAVE survey and seismic data from *Kepler* K2 mission in collaboration with Marica Valentini[1] and Cristina Chiappini[1] – Valentini et al. (2016a).

- We computed masses and radii for red giant stars with Hipparcos parallaxes, seismic data from CoRoT, and spectroscopic data from Morel et al. (2014) in collaboration with Nadege Lagarde[2] and Andrea Miglio[2] – Lagarde et al. (2015) .

- We computed stellar properties for a bright stars in order to study corrections on the classic $\nu_{\max}$ scaling relation in collaboration with the Hugo Coelho[2], Andrea Miglio[2], and Bill Chaplin[2] – Coelho et al. (2015).

- We are also part of the Asteroseismology of STEllar Populations group (asteroSTEP), which aims to foster, and coordinate, collaborations between researchers interested in stellar population studies using CoRoT and Kepler data. We are participating in a project which the goal is to assess under which conditions and with which accuracy the properties of a stellar population can be recovered within the uncertainties of classical and seismic data (including target selection biases). We are using the code PARAM to retrieve the stellar parameters of artificial datasets.

- We also worked in our interpolation code in order to deal with the new tracks from PARSEC (Bressan et al., 2012) and COLIBRI (Marigo et al., 2013). This work, together with many other improvements, has been implemented in the new PARSEC-COLIBRI isochrones, to be soon released (Marigo et al. 2017, submitted).

---

[1]Leibniz-Institut für Astrophysik Potsdam (AIP), Potsdam, Germany

[2]School of Physics and Astronomy, University of Birmingham, Edgbaston, Birmingham, UK

Table 4.1: Derived distances and extinctions with the Bayesian and direct methods for APOKASC stars. LCI and UCI are the lower and upper limits of the 68 per cent CI, respectively. The last column lists the filters for which the photometry is available. A full table is provided in electronic format on the journal website.

KIC ID	2MASS ID	Bayesian method						Direct method						Photometry
		d (pc)			A_V (mag)			d (pc)			A_V (mag)			
		mode	LCI	UCI	mode	LCI	UCI	mode	LCI	UCI	mode	LCI	UCI	
1162746	J19252639+3649116	1420	1397	1435	0.11	0.04	0.14	1318	1262	1368	0.10	-0.08	0.23	griz JHK_s W_1W_2
1432587	J19254985+3701028	2514	2452	2554	0.16	0.04	0.24	2418	2292	2512	0.21	-0.01	0.35	griz JHK_s W_1W_2
1433593	J19264298+3704199	1135	1105	1162	0.16	0.01	0.25	1177	1128	1208	0.21	0.06	0.32	griz JHK_s W_1W_2
1433730	J19265020+3703054	1077	1043	1135	0.45	0.20	0.54	1138	1087	1170	0.38	0.20	0.48	griz JHK_s W_1W_2
1435573	J19282646+3705369	1330	1308	1340	0.13	0.07	0.17	1216	1159	1283	0.16	-0.07	0.32	griz JHK_s W_1W_2

Bibliography

Ahn C. P. et al., 2014, ApJS, 211, 17

—, 2012, ApJS, 203, 21

Alam S. et al., 2015, ApJS, 219, 12

Allende Prieto C., Beers T. C., Wilhelm R., Newberg H. J., Rockosi C. M., Yanny B., Lee Y. S., 2006, ApJ, 636, 804

Anders F. et al., 2016a, ArXiv e-prints

—, 2016b, ArXiv e-prints

—, 2016c, Astronomische Nachrichten, 337, 926

Angulo C. et al., 1999, Nuclear Physics A, 656, 3

Arce H. G., Goodman A. A., 1999, ApJ, 512, L135

Baglin A., Fridlund M., 2006, in ESA Special Publication, Vol. 1306, ESA Special Publication, Fridlund M., Baglin A., Lochard J., Conroy L., eds., p. 11

Bahcall J. N., Basu S., Pinsonneault M., Serenelli A. M., 2005, ApJ, 618, 1049

Bahcall J. N., Soneira R. M., 1984, ApJS, 55, 67

Ball W. H., Beeck B., Cameron R. H., Gizon L., 2016, ArXiv e-prints

Basu S., Chaplin W. J., Elsworth Y., 2010, ApJ, 710, 1596

Basu S. et al., 2011, ApJ, 729, L10

Beck P. G. et al., 2011, Science, 332, 205

Bedding T. R. et al., 2011, Nature, 471, 608

Belkacem K., Goupil M. J., Dupret M. A., Samadi R., Baudin F., Noels A., Mosser B., 2011, A&A, 530, A142

Belkacem K., Samadi R., Mosser B., Goupil M.-J., Ludwig H.-G., 2013, in Astronomical Society of the Pacific Conference Series, Vol. 479, Progress in Physics of the Sun and Stars: A New Era in Helio- and Asteroseismology, Shibahashi H., Lynas-Gray A. E., eds., p. 61

Binney J. et al., 2014, MNRAS, 437, 351

Binney J., Merrifield M., 1998, Galactic Astronomy

Bland-Hawthorn J., Gerhard O., 2016, ARA&A, 54, 529

Blitz L., Spergel D. N., 1991, ApJ, 379, 631

Bonatto C., Bica E., Girardi L., 2004, A&A, 415, 571

Borucki W. J. et al., 2010, Science, 327, 977

Bossini D. et al., 2015, MNRAS, 453, 2290

Bovy J. et al., 2014, ArXiv e-prints

Box G. E. P., Tiao G. C., 1973, Bayesian Inference in Statistical Analysis. Addison Wesley, Reading, Mass.

Bressan A., Marigo P., Girardi L., Salasnich B., Dal Cero C., Rubele S., Nanni A., 2012, MNRAS, 427, 127

Brewer L. N. et al., 2016, AJ, 151, 66

Brogaard K., Bruntt H., Grundahl F., Clausen J. V., Frandsen S., Vandenberg D. A., Bedin L. R., 2011, A&A, 525, A2

Brogaard K. et al., 2016, ArXiv e-prints

—, 2012, A&A, 543, A106

Brown T. M., Gilliland R. L., Noyes R. W., Ramsey L. W., 1991, ApJ, 368, 599

Brown T. M., Latham D. W., Everett M. E., Esquerdo G. A., 2011, AJ, 142, 112

Burnett B., Binney J., 2010, MNRAS, 407, 339

Cardelli J. A., Clayton G. C., Mathis J. S., 1989, ApJ, 345, 245

Casagrande L. et al., 2014, ApJ, 787, 110

Casagrande L., VandenBerg D. A., 2014, MNRAS, 444, 392

Castelli F., Kurucz R. L., 2003, in IAU Symposium, Vol. 210, Modelling of Stellar Atmospheres, N. Piskunov, W. W. Weiss, & D. F. Gray, ed., p. 20P

Chabrier G., 2001, ApJ, 554, 1274

Chaplin W. J. et al., 2011, Science, 332, 213

Chaplin W. J., Miglio A., 2013, ARA&A, 51, 353

Chiappini C. et al., 2015, A&A, 576, L12

Christensen-Dalsgaard J., Silva Aguirre V., Elsworth Y., Hekker S., 2014, MNRAS, 445, 3685

Coelho H. R., Chaplin W. J., Basu S., Serenelli A., Miglio A., Reese D. R., 2015, MNRAS, 451, 3011

Corsaro E. et al., 2012, ApJ, 757, 190

Cutri R. M. et al., 2003, 2MASS All Sky Catalog of point sources.

da Silva L. et al., 2006, A&A, 458, 609

Davenport J. R. A. et al., 2014, MNRAS, 440, 3430

Davies G. R., Miglio A., 2016, Astronomische Nachrichten, 337, 774

De Ridder J., Molenberghs G., Eyer L., Aerts C., 2016, ArXiv e-prints

Eddington A. S., 1918, MNRAS, 79, 2

—, 1926, The Internal Constitution of the Stars

Eggenberger P. et al., 2010, A&A, 519, A116

Eisenstein D. J. et al., 2011, AJ, 142, 72

Epstein C. R. et al., 2014, ApJ, 785, L28

Ferguson J. W., Alexander D. R., Allard F., Barman T., Bodnarik J. G., Hauschildt P. H., Heffner-Wong A., Tamanai A., 2005, ApJ, 623, 585

Feuillet D. K., Bovy J., Holtzman J., Girardi L., MacDonald N., Majewski S. R., Nidever D. L., 2016, ApJ, 817, 40

Frandsen S. et al., 2002, A&A, 394, L5

Freeman K. et al., 2013, MNRAS, 428, 3660

Freeman K. C., 2012, in Astronomical Society of the Pacific Conference Series, Vol. 458, Galactic Archaeology: Near-Field Cosmology and the Formation of the Milky Way, Aoki W., Ishigaki M., Suda T., Tsujimoto T., Arimoto N., eds., p. 393

Gai N., Basu S., Chaplin W. J., Elsworth Y., 2011, ApJ, 730, 63

García Pérez A. E. et al., 2016, AJ, 151, 144

Gilliland R. L. et al., 2010, PASP, 122, 131

Gilmore G. et al., 2012, The Messenger, 147, 25

Gilmore G., Reid N., 1983, MNRAS, 202, 1025

Girardi L., Barbieri M., Miglio A., Bossini D., Bressan A., Marigo P., Rodrigues T. S., 2015, in Astrophysics and Space Science Proceedings, Vol. 39, Asteroseismology of Stellar Populations in the Milky Way, Miglio A., Eggenberger P., Girardi L., Montalbán J., eds., p. 125

Girardi L., Bertelli G., Bressan A., Chiosi C., Groenewegen M. A. T., Marigo P., Salasnich B., Weiss A., 2002, A&A, 391, 195

Girardi L. et al., 2008, PASP, 120, 583

Girardi L., Grebel E. K., Odenkirchen M., Chiosi C., 2004, A&A, 422, 205

Girardi L., Groenewegen M. A. T., Hatziminaoglou E., da Costa L., 2005, A&A, 436, 895

González Hernández J. I., Bonifacio P., 2009a, A&A, 497, 497

—, 2009b, A&A, 497, 497

Goudfrooij P., Girardi L., Rosenfield P., Bressan A., Marigo P., Correnti M., Puzia T. H., 2015, MNRAS, 450, 1693

Gough D., 2003, Ap&SS, 284, 165

Gough D. O., 1986, in Hydrodynamic and Magnetodynamic Problems in the Sun and Stars, Osaki Y., ed., p. 117

Grebel E. K., Roberts W. J., 1995, A&AS, 109, 293

Green G. M. et al., 2014, ApJ, 783, 114

—, 2015, ApJ, 810, 25

Grevesse N., Noels A., 1993, Physica Scripta Volume T, 47, 133

Guggenberger E., Hekker S., Basu S., Bellinger E., 2016, MNRAS, 460, 4277

Gunn J. E. et al., 2006, AJ, 131, 2332

Handberg R. et al., submitted, , submitted

Harris W. E., 1996, AJ, 112, 1487

Hayden M. R. et al., 2014, AJ, 147, 116

Hekker S. et al., 2010, ApJ, 713, L187

Hekker S., Elsworth Y., Mosser B., Kallinger T., Basu S., Chaplin W. J., Stello D., 2013, A&A, 556, A59

Henden A. A., Levine S., Terrell D., Welch D. L., 2015, in American Astronomical Society Meeting Abstracts, Vol. 225, American Astronomical Society Meeting Abstracts, p. 336.16

Hernandez X., Valls-Gabaud D., Gilmore G., 1999, MNRAS, 304, 705

Hole K. T., Geller A. M., Mathieu R. D., Platais I., Meibom S., Latham D. W., 2009, AJ, 138, 159

Holtzman J. A. et al., 2015, AJ, 150, 148

Huber D. et al., 2011, ApJ, 743, 143

—, 2010, ApJ, 723, 1607

—, 2013, Science, 342, 331

—, 2012, ApJ, 760, 32

—, 2014, ApJS, 211, 2

Iglesias C. A., Rogers F. J., 1996, ApJ, 464, 943

Ivezić Ž. et al., 2008, ApJ, 684, 287

Jeffries, Jr. M. W. et al., 2013, AJ, 146, 58

Jørgensen B. R., Lindegren L., 2005, A&A, 436, 127

Jurić M. et al., 2008, ApJ, 673, 864

Kaiser N. et al., 2010, in Society of Photo-Optical Instrumentation Engineers (SPIE) Conference Series, Vol. 7733, Society of Photo-Optical Instrumentation Engineers (SPIE) Conference Series, p. 0

Kapteyn J. C., 1922, ApJ, 55, 302

Kjeldsen H., Christensen-Dalsgaard J., Handberg R., Brown T. M., Gilliland R. L., Borucki W. J., Koch D., 2010, Astronomische Nachrichten, 331, 966

Krishna Swamy K. S., 1966, ApJ, 145, 174

Kurtz D., 2005, in Distant Worlds, Joint European and National Astronomy Meeting, p. 26

Lagarde N., Bossini D., Miglio A., Vrard M., Mosser B., 2016, MNRAS, 457, L59

Lagarde N. et al., 2015, A&A, 580, A141

Laney C. D., Joner M. D., Pietrzyński G., 2012, MNRAS, 419, 1637

Ledoux P., 1945, ApJ, 102, 143

Lillo-Box J. et al., 2014, A&A, 562, A109

Lindegren L. et al., 2016, ArXiv e-prints

Maeder A., 1975, A&A, 40, 303

Maíz-Apellániz J., 2001, AJ, 121, 2737

Majewski S. et al., 2014, APOGEE main paper, in prep.

Majewski S. R., Zasowski G., Nidever D. L., 2011, ApJ, 739, 25

Marigo P., Bressan A., Nanni A., Girardi L., Pumo M. L., 2013, MNRAS, 434, 488

Marigo P., Girardi L., Bressan A., Groenewegen M. A. T., Silva L., Granato G. L., 2008, A&A, 482, 883

Marigo P. et al., 2017, ApJ, 835, 77

Mészáros S. et al., 2013, AJ, 146, 133

Miglio A., 2012, in Red Giants as Probes of the Structure and Evolution of the Milky Way, Miglio A., Montalbán J., Noels A., eds., p. 11

Miglio A., Brogaard K., Stello D., Chaplin W. J., et al., 2012, MNRAS, 419, 2077

Miglio A. et al., 2016, MNRAS, 461, 760

—, 2013, MNRAS, 429, 423

Mihalas D., Binney J., 1981, Galactic astronomy: Structure and kinematics /2nd edition/

Milliman K. E., Mathieu R. D., Geller A. M., Gosnell N. M., Meibom S., Platais I., 2014, AJ, 148, 38

Montalbán J., Miglio A., Noels A., Dupret M.-A., Scuflaire R., Ventura P., 2013, ApJ, 766, 118

Montalbán J., Miglio A., Noels A., Scuflaire R., Ventura P., D'Antona F., 2012, Astrophysics and Space Science Proceedings, 26, 23

Morel T. et al., 2014, A&A, 564, A119

Mosser B., Appourchaux T., 2009, A&A, 508, 877

Mosser B. et al., 2011, A&A, 532, A86

—, 2014, A&A, 572, L5

—, 2012, A&A, 540, A143

O'Donnell J. E., 1994, ApJ, 422, 158

Oort J. H., Kerr F. J., Westerhout G., 1958, MNRAS, 118, 379

Paxton B., Bildsten L., Dotter A., Herwig F., Lesaffre P., Timmes F., 2011, ApJS, 192, 3

Paxton B. et al., 2013, ApJS, 208, 4

Pietrinferni A., Cassisi S., Salaris M., Castelli F., 2004, ApJ, 612, 168

Pinsonneault M. et al., 2014, APOKASC catalog paper, submitted to ApJS

Pinsonneault M. H., An D., Molenda-Żakowicz J., Chaplin W. J., Metcalfe T. S., Bruntt H., 2012, ApJS, 199, 30

Platais I., Gosnell N. M., Meibom S., Kozhurina-Platais V., Bellini A., Veillet C., Burkhead M. S., 2013, AJ, 146, 43

Reese D. R. et al., 2016, A&A, 592, A14

Reimers D., 1975, Memoires of the Societe Royale des Sciences de Liege, 8, 369

Rezaei Kh. S., Bailer-Jones C. A. L., Hanson R. J., Fouesneau M., 2016, ArXiv e-prints

Robin A. C., Reylé C., Derrière S., Picaud S., 2003, A&A, 409, 523

Rodrigues T. S. et al., 2017, MNRAS

—, 2014, MNRAS, 445, 2758

Rogers F. J., Nayfonov A., 2002, ApJ, 576, 1064

Santiago B. X. et al., 2016, A&A, 585, A42

Schlafly E. F. et al., 2014, ApJ, 789, 15

Schlegel D. J., Finkbeiner D. P., Davis M., 1998, ApJ, 500, 525

Schultheis M. et al., 2014, ArXiv e-prints

SDSS Collaboration et al., 2016, ArXiv e-prints

Serenelli A. M., Bergemann M., Ruchti G., Casagrande L., 2013, MNRAS, 429, 3645

Sharma S., Stello D., Bland-Hawthorn J., Huber D., Bedding T. R., 2016, ApJ, 822, 15

Silva Aguirre V. et al., 2012, ApJ, 757, 99

Skrutskie M. F. et al., 2006, AJ, 131, 1163

Sonoi T., Samadi R., Belkacem K., Ludwig H.-G., Caffau E., Mosser B., 2015, A&A, 583, A112

Steinmetz M. et al., 2006, AJ, 132, 1645

Stello D. et al., 2009, ApJ, 700, 1589

—, 2013, ApJ, 765, L41

—, 2011, ApJ, 739, 13

—, 2016, ArXiv e-prints

Stetson P. B., Bruntt H., Grundahl F., 2003, PASP, 115, 413

Strauss M. A. et al., 1999, in Astronomical Society of the Pacific Conference Series, Vol. 177, Astrophysics with Infrared Surveys: A Prelude to SIRTF, Bicay M. D., Cutri R. M., Madore B. F., eds., p. 390

Tassoul M., 1980, ApJS, 43, 469

Tonry J. L. et al., 2012, ApJ, 750, 99

Townsend R. H. D., Teitler S. A., 2013, MNRAS, 435, 3406

Valentini M. et al., 2016a, ArXiv e-prints

—, 2016b, Astronomische Nachrichten, 337, 970

Vandakurov Y. V., 1968, Soviet Ast., 11, 630

Vrard M., Mosser B., Samadi R., 2016, A&A, 588, A87

White T. R., Bedding T. R., Stello D., Christensen-Dalsgaard J., Huber D., Kjeldsen H., 2011, ApJ, 743, 161

Wilson J. C. et al., 2012, in Society of Photo-Optical Instrumentation Engineers (SPIE) Conference Series, Vol. 8446, Society of Photo-Optical Instrumentation Engineers (SPIE) Conference Series

Wright E. L. et al., 2010, AJ, 140, 1868

Wu T., Li Y., Hekker S., 2014, ApJ, 786, 10

Zahn J.-P., 1991, A&A, 252, 179

Zasowski G., 2014, in Asteroseismology of Stellar Populations in the Milky Way, Center for Astrophysics, Sexten, Italy, July 22-26, 2013, in press

Zasowski G. et al., 2013, AJ, 146, 81

—, 2009, ApJ, 707, 510

Eu já me perguntei
Se o tempo poderá
Realizar meus sonhos e desejos
Será que eu já não sei
Por onde procurar
Ou todos os caminhos dão no mesmo
E o certo é que eu não sei o que virá
Só posso te pedir que nunca
Se leve tão a sério, nunca
Se deixe levar, que a vida
É parte do mistério
É tanta coisa pra se desvendar
Por tudo que eu andei
E o tanto que faltar
Não dá pra se prever nem o futuro
O escuro que se vê
Quem sabe pode iluminar
Os corações perdidos sobre o muro
E o certo que eu não sei o que virá
Só posso te pedir que nunca
Se leve tão a sério, nunca
Se deixe levar que a vida
A nossa vida passa
E não há tempo pra desperdiçar.

[TODOS OS CAMINHOS – LENINE]

I am F* crazy
but I am **FREE**!

[RIDE – LANA DEL REY]

Ce l'ho fatta! :)